Dissertation

submitted to the

Combined Faculties for the Natural Sciences and for Mathematics of the
Ruperto-Carola University of Heidelberg, Germany

for the degree of

Doctor of Natural Sciences

Presented by

Dipl.–Phys. M. Saidur Rahaman

from Gangadda, West Bengal

Date of the oral examination: 16.02.2005

First on-line mass measurements at SHIPTRAP and mass determinations of neutron-rich Fr and Ra isotopes at ISOLTRAP

Supervisors: Prof. Dr. H.-Jürgen Kluge

Prof. Dr. Andreas Wolf

Erste on-line Massenmessungen an SHIPTRAP und Massenbestimmungen neutronenreicher Fr- und Ra-Isotope an ISOLTRAP: SHIPTRAP ist eine Ionenfallenanlage hinter dem SHIP-Geschwindigkeitsfilter der GSI/Darmstadt. Das Ziel sind Präzisionsmessungen an Elementen jenseits von Uran, die in einer Fusionsreaktion erzeugt und im Geschwindigkeitsfilter SHIP getrennt werden. Der aktuelle Aufbau zur hochpräzisen Massenbestimmung besteht aus drei funktionalen Einheiten: (i) einer Gaszelle zum Stoppen der energiereichen Ionen von SHIP, (ii) Radiofrequenzquadrupolstrukturen zum Kühlen und Bündeln der aus der Gaszelle extrahierten Ionen und (iii) einem supraleitenden Magneten mit zwei zylindrischen Penningfallen bei einer Feldstärke von 7 T. Im Rahmen dieser Arbeit wurde das Penningfallensystem in Betrieb genommen und ausführlich charakterisiert. Erste on-line Messungen an kurzlebigen Nukliden wurden durchgeführt, und die Massen von ^{147}Er und ^{148}Er konnten erstmals experimentell bestimmt werden. Hierbei wurde eine relative Massenunsicherheit $\delta m/m$ von etwa 1×10^{-6} erreicht.

Desweiteren wurden mit dem ISOLTRAP-Massenspektrometer an ISOLDE/CERN die Massen von schweren, neutronenreichen $^{229-232}$Ra- und ^{230}Fr-Isotopen mit einer relativen Massenunsicherheit von 1×10^{-7} bestimmt. Das Isotop ^{232}Ra ist das schwerste instabile Nuklid, das jemals mit einer Penningfalle untersucht wurde. Die zugrundeliegenden Kernstruktureffekte dieser Nuklide fernab der β-Stabilität wurden durch den Vergleich der experimentellen Zweineutronenseparationsenergien S_{2n} mit denen, die vom "Infinite Nuclear Mass" Modell vorhergesagt werden, untersucht.

First on-line mass measurements at SHIPTRAP and mass determination of neutron-rich Fr an Ra isotopes at ISOLTRAP: SHIPTRAP is an ion trap facility behind the velocity filter SHIP at GSI/Darmstadt. Its aim are precision studies of transuranium nuclides produced in a fusion reaction and separated by SHIP. The current set-up for high-precision mass measurements consists of three main functional parts: (i) a gas cell for stopping the energetic ions from SHIP, (ii) radiofrequency quadrupole structures to cool and to bunch the ions extracted from the gas cell, and (iii) a superconducting magnet with two cylindrical Penning traps at a field strength of 7 T. In this work the Penning trap system has been installed and extensively characterized. The first on-line mass measurements of short-lived nuclides were carried out and the masses of ^{147}Er and ^{148}Er could be experimentally determined for the first time. Here a relative mass uncertainty of $\delta m/m$ of about 1×10^{-6} was achieved.

Furthermore the masses of heavy neutron-rich $^{229-232}$Ra and ^{230}Fr isotopes have been determined with a relative mass uncertainty of about 1×10^{-7} with the ISOLTRAP mass spectrometer at ISOLDE/CERN. The isotope ^{232}Ra is the heaviest unstable nuclide ever investigated with a Penning trap. Underlying nuclear structure effects of these nuclides far from β-stability were studied by a comparison of the resulting two-neutron separation energies S_{2n} with those given by the theoretical Infinite Nuclear Mass model.

Contents

List of Tables

List of Figures

Chapter 1

Introduction

An atom is made of protons, neutrons and electrons. The mass of an atom is not simply the sum the masses of its constituents, the difference is known as the binding energy. Protons and neutrons are held together in the nucleus by the strong force counteracting the Coulomb repulsion of the protons (nuclear binding energy) while the electrons are bound to the nucleus by the electromagnetic force (electron binding energy). The nuclear binding energies are on the order of a million times greater than the electron binding energies of atoms. The nuclear binding energy B is given as

$$B = (Z \cdot M_P + N \cdot M_N - [M_A + B_{el} - Z \cdot M_e])c^2. \qquad (1.1)$$

Here M_P is the mass of the proton, M_N the mass of the neutron, M_A is the mass of the nucleus, B_{el} is the binding energy of the electron and M_e is the mass of the electron. The binding energy can be calculated from Eq. (1.1) measuring the mass M_A since the other masses M_i are known very precisely.

Since the early days of nuclear physics theorists have been trying to formulate mass models predicting masses of a large variety of isotopes. One of the first models is Weizsäcker's mass formula [Weizsäcker35, Bohr98]. Weizsäcker's mass formula is an empirically refined form of the liquid drop model for the binding energy per nucleon given by

$$B = a_{vol}A - a_{sur}A^{2/3} - a_{coul}Z(Z-1)A^{-1/3} - a_{sym}\frac{(A-2Z)^2}{A} + \delta(A), \qquad (1.2)$$

where a_{vol}, a_{sur}, a_{coul} and a_{sym} are constants that have to be adjusted experimentally and $\delta(A)$ is the so called pairing energy. If N and Z are even $\delta(A) = +a_p A^{-3/4}$, if N and Z are odd $\delta(A) = -a_p A^{-3/4}$ otherwise $\delta(A) = 0$. The binding energy according to this formula as a function of A is shown in Fig. 1.1.

From Eq. (1.2) one can conclude that the mass is an important factor which affects many other parameters in the nucleus. Hence precise mass measurements of nuclides are important to unfold many questions in several disciplines in physics. Particularly in nuclear physics systematic mass measurements of nuclides, all over the nuclear chart,
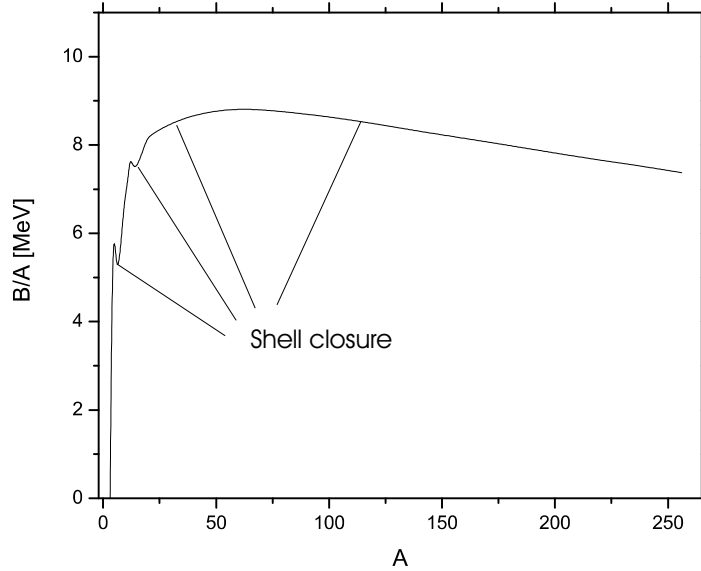
Figure 1.1: Plot of Weizsäcker's formula for binding energy per A as a function of A for some stable nuclides. The position of Shell closures are indicated. The parameters are used $a_{vol} = 15.5$, $a_{sur} = 16.8$, $a_{coul} = 0.72$, $a_{sym} = 23$, $a_p = 34$ in units of MeV/c^2.

are the basic ground for testing various nuclear models and their further improvements. They also provide a better knowledge of the interaction between the nuclear constituents. Accurate mass data allows for a systematic investigation of the binding energy as a function of proton and neutron number, to investigate nuclear structure effects as, for instance, pairing, shell and sub-shell closures as well as deformation effects. In astrophysics, masses and half-lives of exotic nuclei are important parameters for understanding the synthesis of the elements beyond iron (Z$\geq$26). Mass measurements near the proton or neutron drip-line with a precision of $\delta m/m = 10^{-6}$ help to understand the rapid-neutron capture process (r-process) or the rapid-proton capture process (rp-process). Halo nuclides, having very small separation energies that are themselves input parameters for microscopic models, require a precision of the order on 10^{-7}. Weak-interaction studies require a precision on the order of 10^{-8}. Precise mass measurements on the order of one times 10^{-8} or better are important for the tests of fundamental relations like the Conserved Vector Current (CVC) hypothesis and the Isobaric-Multiplet Mass Equation (IMME) [Herfurth01a].

Therefore large efforts are presently devoted to improve mass spectrometric techniques for the accurate mass determination of short-lived nuclides far from the valley of stability, such as time-of-flight, Fourier transform ion cyclotron resonance and Schottky mass spectrometry as applied in the storage ring. Penning traps have proven to be the most precise mass spectrometers. For example, ISOLTRAP [Bollen92a, Blaum03] at CERN/Geneva is a Penning trap mass spectrometer for the investigation of short-lived radioactive nuclides with half-lives larger than 50 ms as produced at ISOLDE (Isotope

Separator On-Line DEvice) [Kugler00].
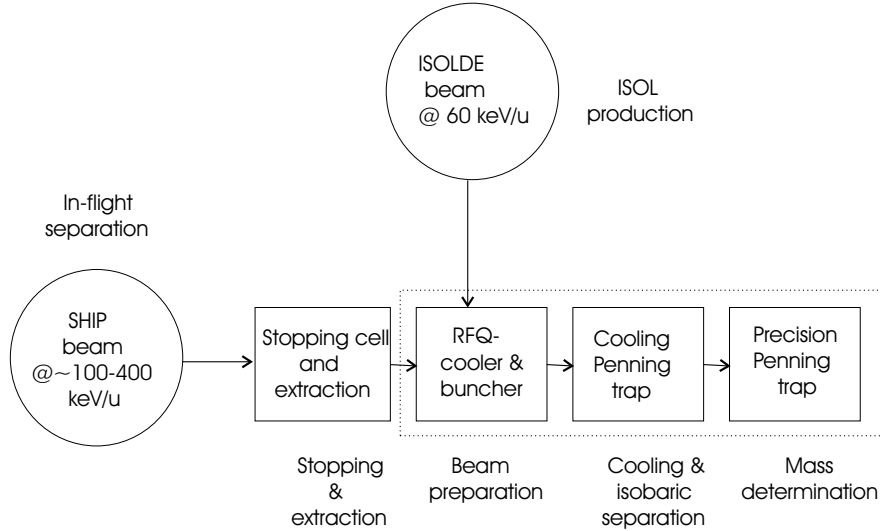
Figure 1.2: Schematic sketch of ISOLTRAP and SHIPTRAP. The common components of both facilities are a RFQ-cooler and buncher, a cooling Penning trap and a precision Penning trap, shown in the dashed box. SHIPTRAP uses a stopping cell to decelerate the energetic ion beam whereas ISOLTRAP uses electric retardation.

The ion trap facility SHIPTRAP [Dilling00, Sikler03b] is installed behind SHIP (Separator for Heavy Ion reaction Products) [Hofmann00] at GSI/Darmstadt for precision mass measurements of transuranium elements. SHIPTRAP and ISOLTRAP are conceptually similar facilities. Both facilities consist of a RFQ buncher and two Penning traps. The basic difference is that a helium filled stopping cell [Neumayr04] is at SHIPTRAP utilized to decelerate the radioactive ion beam whereas ISOLTRAP uses electric retardation [Herfurth01a] to decelerate the ion beam. A schematic drawing of both facilities is shown in Fig. 1.2. The dashed box indicates the components for common both facilities.

In the present work, mass measurements of heavy neutron-rich francium and radium nuclides were performed using the ISOLTRAP mass spectrometer. This work extends the previous investigations by ISOLTRAP [Bollen92b, Weber04] in this region towards the neutron-rich side of the valley of beta-stability. The masses of the short-lived nuclides ^{230}Fr and $^{229-232}$Ra were measured with a relative precision of $1 \cdot 10^{-7}$. The mass values of ^{230}Fr and ^{231,232}Ra were determined experimentally for the first time. Furthermore ^{232}Ra is the heaviest nucleus which has ever been investigated in a Penning trap.

Another goal of this thesis was to commission the double Penning trap mass spectrometer at the SHIPTRAP facility. It consists of two cylindrical Penning traps in one superconducting magnet of 7 Tesla field strength. The main function of the device is isobaric separation and precision mass measurements of radioactive ions. In the course

of this work the set-up was tested, characterized and optimized for better sensitivity and resolving power of the mass spectrometer. Furthermore for the first time, the Penning trap mass spectrometer was used for on-line mass measurements of holmium and erbium isotopes. The mass values of ^{147}Er and ^{148}Er were determined experimentally for the first time with a precision of 1×10^{-6}. A detailed description of the characterization of the Penning trap mass spectrometer and the mass measurement procedure is described in this thesis.

This thesis consists of nine chapters. In chapter 2 the two radioactive ion beam facilities SHIP at GSI/Darmstadt and ISOLDE at CERN/Geneva are described. In addition different mass measurement techniques are discussed. Only the direct mass measurement techniques are presented and their complementarity is outlined. In chapter 3 the theory of Penning traps and their application as isobaric separator and as mass spectrometer are described. Chapter 4 focuses on the main components that were developed for the SHIPTRAP facility, such as stopping cell, RFQ-buncher and Penning trap system where the latter is described in detail in chapter 5. The following chapter is devoted to the characterization of the Penning trap mass spectrometer and the test measurements performed with stable ^{133}Cs ions. Chapter 7 describes the mass measurement procedure. Chapter 8 focuses on the the first on-line experiment of SHIPTRAP which resulted in new mass excess values of ^{147}Er and ^{148}Er. In chapter 9 the ISOLTRAP mass spectrometer is described and precise mass values of the mass of ^{230}Fr and ^{231,232}Ra are presented which were obtained at ISOLTRAP. The physics relevance of the results is discussed.

Chapter 2

Radioactive ion beam facilities and mass measurement techniques

2.1 Production and separation of radioactive nuclei

Radioactive nuclei are produced in the laboratory by various nuclear reactions with an energetic primary beam impinging on a target. The production mechanisms are classified according to the energy of the primary beam. These are multi-nucleon transfer and charge exchange, deep-inelastic reactions, fusion evaporation reactions, fission induced by light ions, fragmentation and spallation reactions. All these processes are useful to produce radioactive nuclei over a wide range of half-lives. The separation methods used depend on the production mechanism. The most commonly used separation methods are in-flight-separation [Geissel95] and the Isotope Separation On-Line (ISOL) method [Ravn92].

The in-flight-separation method is mainly used with production mechanisms where the secondary particles have a strong forward focusing in transporting the beam to the experimental area. The radioactive nuclei are separated by means of magnetic and electric fields. The preparation time of the secondary nuclei is about 1 μs and their energy vary from about 1 MeV/u to 1 GeV/u. The main advantage of this separation method is that there is no need to post accelerate the secondary nuclei. It is very useful to prepare and separate the short-lived radioactive nuclei. At the Separator for Heavy Ion reaction Products (SHIP) facility at GSI/Darmstadt the in-flight-separation method is used for the secondary beam preparation.

The other complementary method is the Isotope Separation On-Line (ISOL). In this case the production target is thick compared to the in-flight technique in order to stop the primary beam and the radioactive nuclei produced in the reaction. The reaction products diffuse out from the high-temperature (2000°) target, are ionized in an ion source region, subsequently accelerated (10-100 keV) and electromagnetically separated. The preparation time is mainly due to the diffusion process which ranges from ms to seconds or minutes depending on the target materials and on the properties of the element produced. The beam quality in this process is determined by the target

and ion source properties. One can get a very good beam quality (emittance $\leq 10\pi$ mm mrad, energy dispersion less than 5 eV) at a low kinetic energy. At the ISOLDE facility at CERN radioactive nuclides are produced in a thick high-temperature target via spallation, fission or fragmentation reactions. This facility is shortly discussed in this chapter. Other ISOL systems are operated, for example, at Louvain-La Neuve, TRIUMF and Jyväskylä.

2.1.1 SHIP facility

The Separator for Heavy Ion reaction Products (SHIP) facility [Münzenberg79, Hofmann00] is well known world-wide for the discovery of super-heavy elements. A schematic diagram of the SHIP facility is shown in Fig. 2.1. It is a kinematic separator installed behind the UNIversal Linear ACcelerator (UNILAC) at GSI/Darmstadt and can provide nuclei which are not accessible at ISOL facilities [Kugler00]. Especially, elements heavier than uranium can be produced and separated by the in-flight method at SHIP. The elements are synthesized in fusion-evaporation reactions with a primary beam from UNILAC impinging on a thin, heavy-element target (≤ 1 mg/cm^2) such as lead or bismuth. Target foils are mounted on a wheel rotating through the beam in order to distribute the beam power onto a large area as shown in Fig. 2.1. The primary beam has an energy of about 5 MeV/u which is sufficient to overcome the Coulomb barrier and a time-averaged intensity of about 2-5·10^{12} ions per second. Energy is transferred from the primary beam to the secondary products by momentum transfer. The secondary products are then deexcited by emission of neutrons, protons or α-particles.
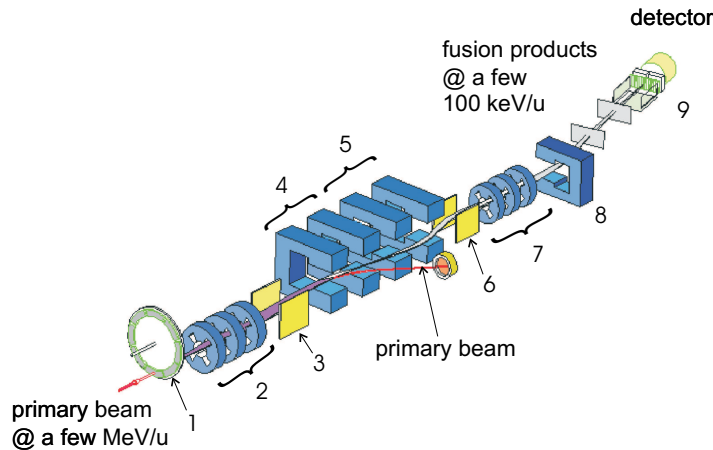
Figure 2.1: Overview of the SHIP velocity filter. 1: rotating target wheel, 2, 7: quadrupole lenses, 3 and 6: electric deflectors, 4, 5 and 8: dipole magnets, 9: Si detectors.

Once a compound nucleus is formed, it is focused using electromagnetic quadrupole triplets at the beginning and towards the end of the ion-optical set-up shown in Fig. 2.1.

The main part of the set-up consists of a two-stage velocity filter. The velocity filter is a combination of electric deflectors and dipole magnets. If q describes the charge state, $\overrightarrow{v}$ the velocity, and $\overrightarrow{B}$ and $\overrightarrow{E}$ the magnetic and electric fields, then the magnetic and electric force experienced by the charged particle is given by

$$\overrightarrow{F}_{mag} = q \cdot (\overrightarrow{v} \times \overrightarrow{B}) \tag{2.1}$$

and

$$\overrightarrow{F}_{elec} = q \times \overrightarrow{E}. \tag{2.2}$$

When $F_{mag} = -F_{elec.}$, the total force on the particle cancels which gives

$$v_i = \frac{E}{B}. \tag{2.3}$$

So a particular choice of the ratio E/B selects a single velocity class which allows particles to pass the filter independent of their charge state. The last magnetic dipole, shown in Fig. 2.1, deflects the beam by 7.5^0 for a reduction of background from scattered primary beam. At the end there are time-of-flight detectors consisting of a pair of thin carbon foils combined with a pair of micro-channel plates. A charged particle creates secondary electrons while passing through the carbon foil which are detected by the micro-channel plate. In addition a position sensitive silicon detector is used to identify the super-heavy elements by their α-decay chains to known daughter nuclei.

For example, the element $^{277}112$ is described below. The element $^{277}112$ was synthesized using the one-neutron evaporation channel in the reaction

$$^{70}\text{Zn} + {}^{208}\text{Pb} = {}^{277}112 + 1n, \tag{2.4}$$
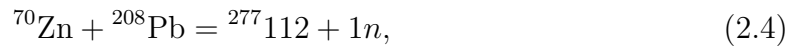
where ^{70}Zn is the primary beam with an energy of 4.5 MeV/A and the excitation energy in the one-neutron evaporation channel is 10.1 MeV [Hofmann00]. ^{208}Pb was used as a target nucleus. A cross section of 1 pb, (two events in 24 days) was deduced from the experiments [Hofmann00].

2.1.2 ISOLDE facility

The ISOLDE facility, the fourth-generation on-line isotope separator, is installed behind the Proton-Synchrotron Booster (PSB) at CERN/Geneva [Kugler00]. Its purpose is the production of pure beams of low-energy radioactive ions for a large number of different physics and chemistry experiments. About 600 isotopes of more than 60 elements can be produced via fission, fragmentation, or spallation reactions. A high-energy proton beam impinges on a target that is thick enough to stop the products. Up to 3.2×10^{13} protons per pulse at time intervals of 1.2 to 2.4 second bombard the target with energies of 1.0 to 1.4 GeV.

The target is made out of different materials depending on the product(s) of interest and has a thickness of 3 g/cm^2 in the case of MgO targets and roughly 350 g/cm^2

in the case of UC_2. The target is usually contained in a tantalum cylinder which is resistivily heated by a current of up to 1000 A resulting in a temperature of up to 2500 ^{0}C. These high target temperatures enhance the diffusion of the reaction products to the ion source. In the ion source region the radioactive atoms are ionized either by surface ionization, in a hot plasma, or by laser ionization before being accelerated to 60 keV and distributed as quasi-DC ion beam to the experiments. The different methods employed for the ionization of the reaction products are chosen depending on the chemical properties of the desired nuclei in order to efficiently ionize them and to suppress all the unwanted contaminants.

Two target stations deliver ion beams to two different sector magnet mass separators. The general purpose separator (GPS) consists of one 90-degree H magnet with a field strength of 0.45 T. It achieves a mass resolving power of about 1000. The more recent high-resolution separator (HRS) is made up of one 60-degree magnet and one 90-degree magnet, both magnets with 0.7 T field strength. It reaches a mass resolving power of 7,000.

After the separators, the radioactive beam is distributed to the different experiments located in the ISOLDE experimental hall. The ion optical elements along the beam lines for focussing and deflection are exclusively electrostatic devices in order to ensure a mass-independent transport of the beam.

2.2   Different mass measurements techniques

Mass measurements of atoms started about 100 years in order to unfold many questions in different disciplines of physics. In the early days of nuclear physics, research was mostly limited to stable or nuclides near the valley of stability but meanwhile the nuclides closer and closer to the driplines are becoming accessible. Radioactive isotopes far from the valley of stability are more and more difficult to produce and it is even more difficult to measure their mass because of their short half-lives. Therefore many different mass measurement techniques have been developed.

2.2.1   Time-of-flight method

One of the most important advances in the last decade in the measurement of masses far from the valley of stability has been the development of time-of-flight techniques. Such spectrometers are SPEG at GANIL [Bianchi89] and TOFI at Los Alamos [Wouters85]. The method is mainly based on a time-of-flight measurement combined with a magnetic rigidity analysis. If $B\rho$ is the magnetic rigidity, v the velocity of an ion, and q the charge state, then the mass m can be deduced from the relation

$$\frac{B\rho}{v} = \gamma \cdot \frac{m}{q},\tag{2.5}$$

where γ is the relativistic factor.
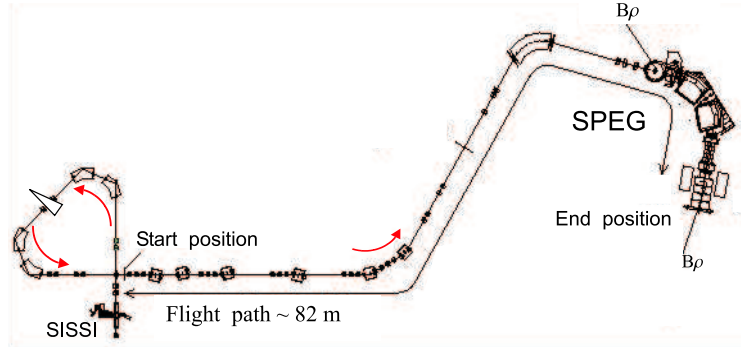
Figure 2.2: Sketch of the high-resolution mass spectrometer SPEG. The nuclides are produced in fragmentation reactions as SISSI (Source d'Ions Secondaire á Supraconducteur Intense).

The high-resolution mass spectrometer SPEG (Spectrométre à Perte d'Energie du Ganil) is shown in Fig. 2.2. A resolving power of about 10^4 is commonly achieved in this experiment. The velocity v is determined from the time of flight of the ions from the start position to the detector which is about 82 m. Secondary particles require about 1 μs to reach the detector in the end position (see Fig. 2.2). The device is well suited to measure the masses of short-lived nuclei ($T_{1/2} \approx 1$ μs). Only this technique allows for mass measurements up to the neutron drip line in the mass range A$\sim$ 10 - 50 [Savajols01] and towards the proton drip line up to A$\sim$ 70.

2.2.2   Mass measurements in Storage Rings

At the Experimental Storage Ring (ESR) at GSI/Darmstadt a cyclic method for mass measurements of nuclei far from the valley of stability is used [Klepper92]. A schematic drawing of the ESR is shown in Fig. 2.3. The secondary ions produced in fragmentation reactions are separated by the fragment separator (FRS) and then injected into the ESR. Relativistic radioactive ions are stored and cooled in the ESR at energies range between 300 MeV/A to 400 MeV/A [Geissel01]. The mass is determined from the revolution frequency of the ion in the ESR. The relative difference in the frequency $\Delta\nu/\nu$ of two species differing in mass by Δm and in velocity by Δv is given by

$$\frac{\Delta\nu}{\nu} = -\frac{1}{\gamma_t^2}\frac{\Delta m/q}{m/q} + \left(\frac{1}{\gamma_t^2} - \frac{1}{\gamma^2}\right)\frac{\Delta v}{v}, \tag{2.6}$$

where $\gamma = \sqrt{1 - (v/c)^2}$ is the relativistic factor and $\gamma_t = \sqrt{1 - (v_t/c)^2}$ is the value of γ at the transition energy. At γ_t, ions with a specific mass-over-charge ratio circulating in the ring need exactly the same time to make one turn independent of their velocity. A mass measurement at ESR can be performed in two different modes: Schottky Mass Spectrometry (SMS) and the Isochronous Mass Spectrometry (IMS). This two modes
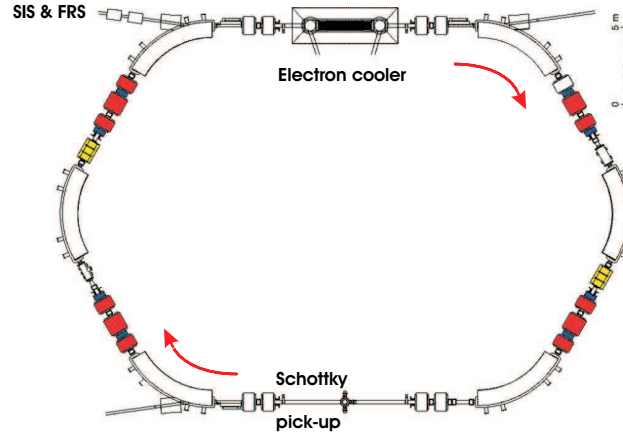
Figure 2.3: Sketch of the Experimental Storage Ring (ESR) at GSI/Darmstadt. The ions are injected from the Fragment Separator (FRS) and transported into the ring guided by electric and magnetic fields. An electron cooler is installed for beam cooling. In addition stochastic cooling can be used. The circumference is ~ 108 m

differ in the way in which the second term in Eq. (2.6) is made negligible.

In Schottky Mass Spectrometry mode, the term $\Delta v/v$ in Eq. (2.6) is made negligible by reducing Δv by means of electron cooling. Electron cooling allows to decrease $\Delta v/v$ down to 10^{-6} in a few seconds [Steck98]. So one can neglect the second term in Eq. (2.6) and the mass is determined from the measured frequency for a known charge state. The ions, circulating in the ring, induce a detectable image charge in a conductor plate (Schottky pick-up). The revolution frequency is obtained from a Fourrier transform of this time-dependent signal and the mass-to-charge ratio can be unfolded by Eq. (2.6). The masses of 104 nuclides with $57 \leq Z \leq 84$ were measured for the first time with an accuracy of $5 \cdot 10^{-7}$ [Radon2000]. In later measurements a relative accuracy of down to $1.5 \cdot 10^{-7}$ was obtained [Lunney03]. However, because of the time required for electron cooling to reduce $\Delta v/v$, the SMS only works for nuclides with half-lives longer than about 10 seconds.

In the case of IMS mode γ equals γ_t and the second term in Eq. (2.6) is zero. The time of flight is recorded for many turns of the ions in the ring by observing the secondary electrons emitted from a foil through which the ion passes. Typically 100-1000 turns can be observed resulting in a time-of-flight path of 10-100 km. Since no electron cooling is required, the masses of very short-lived isotopes can be determined by IMS. For instance the technique was successfully applied to measure the mass of the neutron-deficient nuclides ^{68}As, ^{70,71}Se and ^{73}Br [Hausmann01].
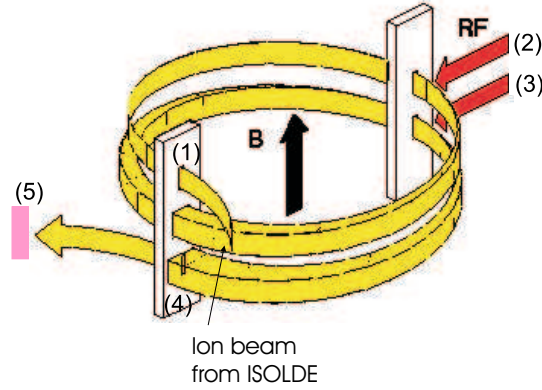
Figure 2.4: Sketch of the transmission radiofrequency spectrometer MISTRAL at CERN/Geneva. 1: entrance slit, 2: first modulator, 3: second modulator, 4: exit slit, 5: electron multiplier.

2.2.3 Cyclotron frequency measurements

Transmission radio frequency spectrometer

A schematic diagram of the transmission radiofrequency spectrometer MISTRAL (Mass Measurements at ISOLDE using a Transmission and RAdiofrequency spectrometer on Line) [Toader99, Lunney01] with its nominal trajectory is shown in Fig. 2.4. The nucleus with the shortest half-life for which the mass was measured is ^{11}Li with a half-life of 8.75 ms [Bachelet04]. The short transit time of $\sim 50 \mu$s makes MISTRAL ideally suited for high-precision mass measurements of short-lived nuclei far from stability. At ISOL facilities the main parts of the radiofrequecy mass spectrometer are a magnet with a highly homogeneous magnetic field, a RF modulator and two symmetrical beam lines for injection and extraction of the beam. The beam with an energy of 60 keV from ISOLDE is injected into the homogeneous area of the magnet, makes two turns in a slightly helicoidal trajectory in a radiofrequency electric field that accelerates or decelerates the beam. Ions only reach the final detector if the radiofrequency ω_{RF} is related to their cyclotron frequency ω_c through $\omega_{RF} = (n+1/2)\omega_c$, which leads to a cancellation of the two modulations. When the modulator frequency is scanned, narrow transmission peaks are observed (with a resolution of R = 10^5) for an integer value of ω_{RF} /ω_c - 1/2, where the transmission is maximum. MISTRAL can reach in the best case a relative mass accuracy of $2 \cdot 10^{-7}$.

Penning trap mass spectrometer

This is described in detail in Section 3.4.
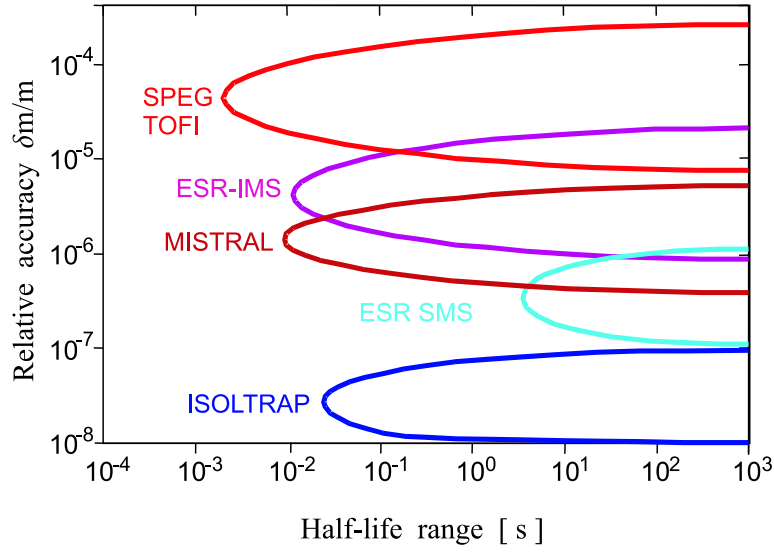
Figure 2.5: The relative mass accuracy plotted as a function of the half-life of the radioactive nuclei reached by different methods.

2.3   Comparison of different techniques

A comparison between different mass measurement techniques is shown in Fig. 2.5. The figure shows the relative mass accuracy which can be achieved in different techniques and the half-life range of the nuclei that can be accessed. The time-of-flight (SPEG, TOFI) technique provides access to very short-lived radioactive nuclides which cannot be accessed in other techniques. At the ESR, IMS is also expected to give access to very short-lived nuclides ($T_{1/2} \ll 1$ ms). ESR-SMS provides a better mass accuracy at longer half-lives ($T_{1/2} \geq 10$ s). MISTRAL has shown to be able to access nuclides with a half-life down to 9 ms. Regarding the relative accuracy, it is obvious that Penning traps are superior to other techniques in mass measurements for radioactive ions with a half-life ≥ 50 ms.

Chapter 3

Penning trap techniques

A Penning trap is a device that uses electric and magnetic fields to trap charged particles, e.g. ions, in a small volume [Bollen90]. It has become one of the most versatile devices in science. It is used in several fields of experimental physics, such as mass measurements, optical spectroscopy, g-factor measurements, and plasma confinement. It allows for the confinement of particles for a long time, of days or even months. For mass measurements it is suitable due to the fact that the ion motion in the trap depends on the charge-to-mass ratio. It is advantageous for hyperfine spectroscopy that a magnetic field is used for the confinement, because it produces a splitting of the Zeeman energy levels. Atomic and nuclear g-factors can be determined from the measurements of the Larmor precession frequency ω_L and of the cyclotron frequency ω_c of the trapped particle. Applications of Penning traps have also included tests of fundamental theories, e.g. of QED, and the determination of fundamental physical constants such as the fine-structure constant [Dehmelt89] and the mass of electron [Beier02]. Recently the Penning trap has been proposed as a quantum computing device by taking advantage of the hysteresis of a parametrically driven electron that serves as a 1-bit memory [Mancini99].

In this chapter the theory and the principle of a Penning trap is described. Important applications of this trap such as the mass selective buffer gas cooling and mass measurement techniques are presented. These two techniques are implemented at the SHIPTRAP double Penning trap system. These techniques were used to measure the mass of holmium (Ho) and erbium (Er) isotopes which is presented in Chapter 8.

3.1   Principle of a Penning trap

In a Penning trap, charged particles are confined by a strong and homogeneous magnetic field $B = B_z$ in the radial direction. The pure cyclotron frequency due to this magnetic field is

$$\omega_c = \frac{q}{m} \cdot B, \tag{3.1}$$

where m is the mass and q is the charge of the particle.
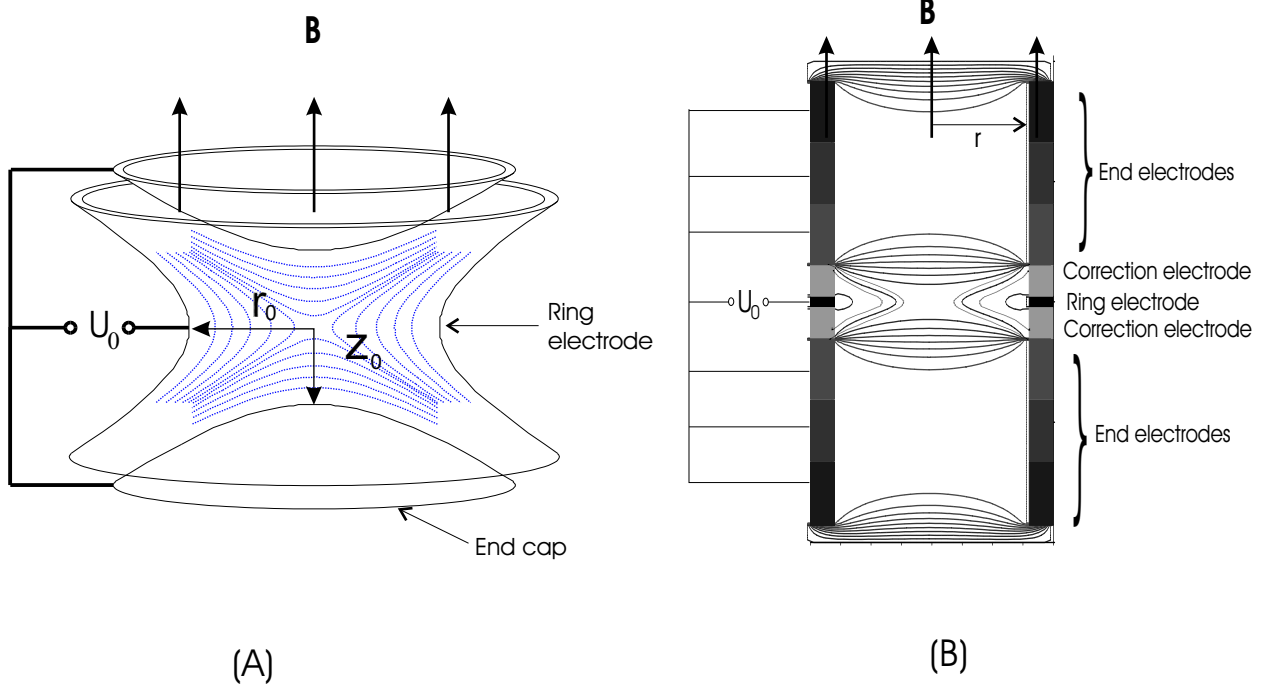
Figure 3.1: A: Hyperbolic Penning trap. An electric DC voltage U_0 is applied between the two endcaps and the ring electrode. The homogeneous magnetic field is oriented along the rotational axis of the electrodes. **B**: Cylindrical Penning trap. It consists of cylindrical electrodes to which appropriate voltages are applied in order to create a quadrupole potential at the center. The correction electrodes are introduced in order to reduce the anharmonicity of the potential. The magnetic field is applied along the symmetry axis of the electrodes. The dotted lines in (**A**) and (**B**) represent the equipotential lines.

The particle is axially bound by superimposing an electrostatic potential. In an ideal Penning trap this potential is harmonic. A quadrupole potential is used to create such a harmonic potential, which is given in radial and axial components by

$$U(r, z) = \frac{U_0}{4d^2}(2z^2 - r^2), \tag{3.2}$$

where U_0 is the trap voltage, r is the radial and z is the longitudinal distance from the trap center. The quadrupole potential has hyperbolic equipotential lines and can be realized by hyperbolically shaped electrodes, as shown in Fig. 3.1(A). The characteristic dimension d of a Penning trap is given by

$$d^2 = \frac{1}{2} \cdot (z_0^2 + \frac{r_0^2}{2}). \tag{3.3}$$

Here r_0 is the inner radius of the trap and z_0 is the minimum longitudinal distance from the trap center to the end cap. The trap voltage U_0 for the axial confinement is applied between the two endcaps and the ring electrode. A positive voltage with respect to the ring electrodes is applied to the end electrodes to confine positive ions. Due to the DC potential the ions experience an electric force in the z-direction towards the center which is proportional to the displacement of the ions from the origin. This force results in a harmonic oscillation of the ions along the axial direction given by

$$\ddot{z} + \omega_z^2 z = 0. \tag{3.4}$$

The axial frequency due to this electrostatic potential is

$$\omega_z = \sqrt{\frac{qU_0}{md^2}}. \tag{3.5}$$
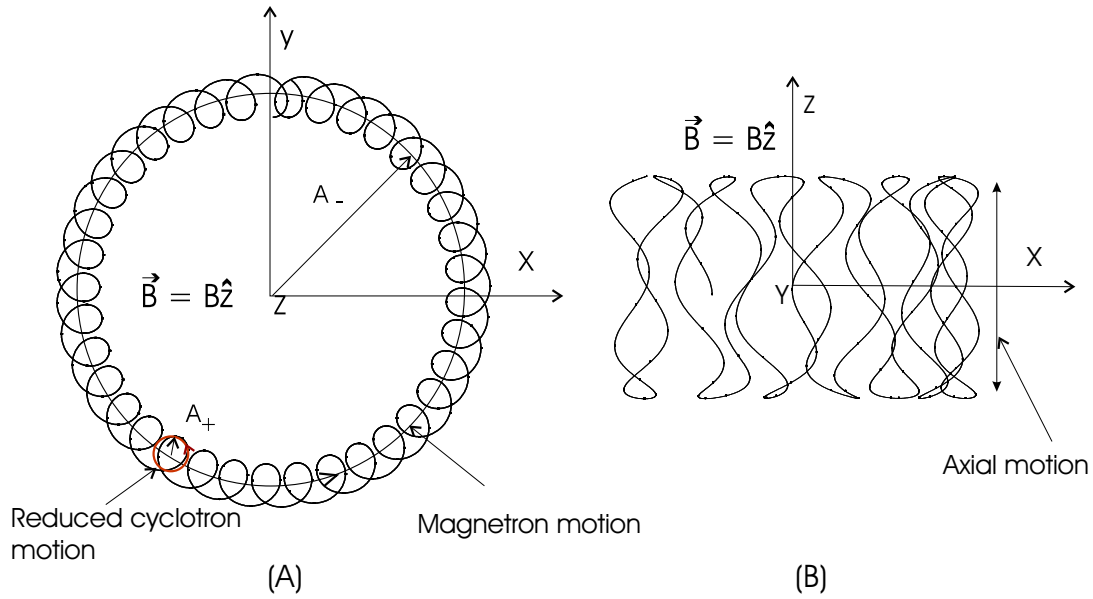
Figure 3.2: **A**: Radial eigenmotions of a stored ion in a Penning trap. The fast reduced cyclotron motion and the slow magnetron motion are shown in the x-y plane. A_+ and A_- are the amplitude of the reduced cyclotron and magnetron motions, respectively. In an ideal case they are decoupled from each other. The magnetic field is along the z-axis. **B**: Axial motion of a stored ion in a Penning trap together with two radial motions. Projection of the eigenmotions on the x-z plane.

The radial motion of the ions due the superposition of electric and magnetic fields is given by the electric force and the Lorentz force

$$\ddot{\vec{r}} = \frac{q}{m}[\vec{E} + (\frac{\dot{\vec{r}}}{c} \times \vec{B})]. \tag{3.6}$$

This equation can be written in terms of pure cyclotron (ω_c) and axial (ω_z) frequencies as

$$\ddot{\vec{r}} - \vec{\omega_c} \times \dot{\vec{r}} - \frac{1}{2}\omega_z^2\vec{r} = 0. \tag{3.7}$$

For vanishing electric field, i.e. for $\omega_z \to 0$, this reduces to the equation for a uniform circular motion at the pure cyclotron frequency ω_c. The additional term $-\frac{1}{2}\omega_z^2\vec{r}$ comes from the repulsive radial term in the electrostatic potential given in Eq. (3.2). This repulsive radial potential leads to two effects, first it reduces the pure cyclotron frequency from ω_c to ω_+. Second, the fast cyclotron orbit is superimposed upon a much slower circular motion, called magnetron motion, with angular frequency ω_-. Hence in the radial plane the ions perform two uncoupled motions, the reduced cyclotron motion with frequency ω_+ and the slow magnetron motion with frequency ω_-.

The solution of the Eq. (3.7) can be found by a proper coordinate transformation, $\vec{u_\pm} = \dot{\vec{r}} - \omega_\pm \hat{z} \times \vec{r}$. With this transformation the solutions are two uncoupled circular motions with frequencies $\omega_\pm$

$$\omega_+ = \frac{\omega_c}{2} + \frac{1}{2}\sqrt{\omega_c^2 - 2\omega_z^2}, \tag{3.8}$$

$$\omega_- = \frac{\omega_c}{2} - \frac{1}{2}\sqrt{\omega_c^2 - 2\omega_z^2}. \tag{3.9}$$

Only the real solutions of the above equations correspond to stable trajectories of the ions inside the Penning trap. Therefore the stability condition $\omega_z < \omega_-/\sqrt{2}$ can be deduced from the Eq. (3.8) or (3.9). The sum of these two frequencies is equal to the pure cyclotron frequency

$$\omega_c = \omega_+ + \omega_-. \tag{3.10}$$

The resulting ion motion in an ideal Penning trap can be described by three uncoupled harmonic oscillations: reduced cyclotron, axial and magnetron oscillation. The motion is a superposition of epicircles with a harmonic axial motion. As an example of ion trajectories in a Penning trap the two radial motions are shown in Fig. 3.2 A in the x-y plane. The axial motion together with the radial motions in the x-z plane are shown in Fig. 3.2 B. It can be shown that the three eigenfrequencies of an ion in a Penning trap are related by the so-called invariance theorem [Brown86]

$$\omega_c^2 = \omega_+^2 + \omega_-^2 + \omega_z^2. \tag{3.11}$$

3.2   Excitation of the ion's motions

To measure the eigenfrequencies of an ion in a Penning trap it is necessary to excite the ion motion by a radiofrequency field. The three motions can be excited by applying a

RF dipole field with proper frequency and orientation. The axial motion is excited by a radiofrequency field which is applied between the two endcap electrodes of the trap. The two radial motions are excited by a RF dipole field perpendicular to the magnetic field. The pure cyclotron motion can also be excited by applying a quadrupole RF field with frequency $\omega_c = \omega_+ + \omega_-$ to a split ring electrode.

3.2.1 Dipole excitation

The required dipole RF field created via a two-fold segmented ring electrode (see Fig. 3.3(A)) to excite the radial motions is given by

$$\overrightarrow{E_x} = E_D \cdot \cos(\omega_{RF}t)\hat{e}_x \tag{3.12}$$

where ω_{RF} is the excitation radiofrequency, $\hat{e}_x$ is the unit vector in the x direction and E_D is given by

$$E_D = C_1 \cdot U_{RF}. \tag{3.13}$$

C_1 is a constant depending on the geometry of the trap, and U_{RF} is the voltage applied to the segmented ring electrode. A transverse cut of the segmented ring electrode in a Penning trap to apply a dipole field is shown in Fig. 3.3(A). If the applied field is in resonance with one of the two eigenfrequencies $\omega_\pm$ (reduced cyclotron or magnetron frequency) the radial energy E_{rad} of the ion will change as a function of the excitation time T according to [Bollen90]
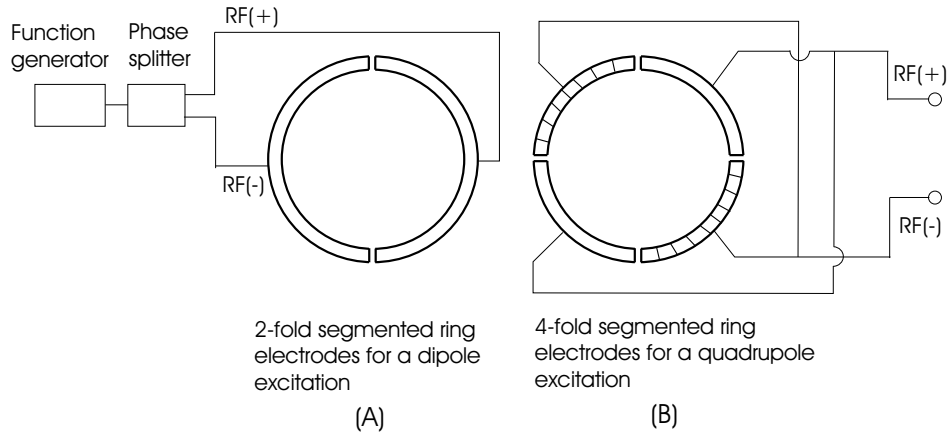
Figure 3.3: Transverse cut of a two-fold (A) and four-fold (B) segmented ring electrode in a Penning trap. **A**: The RF voltage is applied to two opposite segments with a 180 degree phase difference in order to get a dipole field either in the x or y direction. **B**: The RF voltage applied to one pair of opposite segments is phase-shifted by 180 degree with respect to the RF voltage applied to the other pair of opposite segments to create a quadrupole field.

$$E_{rad} \simeq [\frac{\sin((\omega_{RF} - \omega_{\pm}) \cdot T/2)}{(\omega_{RF} - \omega_{\pm})/2}]^2. \tag{3.14}$$

Finally, when the cyclotron or magnetron orbits become larger than the radius of the hole in the end cap or the radius of the cylindrical trap electrodes, the ions cannot be extracted from the Penning trap. A dipole excitation can therefore be used to selectively remove unwanted ions from the trap by increasing the radius of the ion motion. Since the magnetron frequency depends only slightly on the mass, the reduced cyclotron frequency is usually used for this purpose.

3.2.2   Quadrupole excitation with buffer gas

For a precise mass measurement isobarically clean samples are required. These can be obtained using the mass-selective buffer gas cooling technique [Savard91,Herfurth01a]. The ions are loaded into a Penning trap where a buffer gas is present, at a pressure of typically $p \approx 10^{-4} mbar$. To avoid charge exchange processes, noble gases, mainly purified helium, are used. The ion motion is cooled by collisions with buffer gas atoms. For low ion energies of less than a few eV the ion interaction is dominated by a long-range interaction of an ion with buffer gas atoms polarized by this ion. This can be described by a viscous-drag model. The average viscous force is proportional to the velocity of the ion

$$\overrightarrow{F} = -\delta \cdot m \cdot \overrightarrow{v} \tag{3.15}$$

where m is the mass and $\overrightarrow{v}$ is the velocity of the ion. The damping coefficient δ is given by

$$\delta = \frac{e}{m \cdot k_0} \cdot \frac{p/p_N}{T/T_N}. \tag{3.16}$$

The damping coefficient is proportional to the gas pressure p in fractions of the normal pressure $p_N = 1$ bar, and inversely proportional to the temperature T in fractions of the normal temperature $T_N = 273$ K. k_0 is the reduced ion mobility.

Taking into account this damping coefficient in the equations of motion of the ions one can express the amplitudes of the three eigenmotions as a function of time by

$$A_+(t) = A_+(0)e^{-\alpha_+ \cdot t} \tag{3.17}$$

$$A_-(t) = A_-(0)e^{+\alpha_- \cdot t} \tag{3.18}$$

$$A_z(t) = A_z(0)e^{-\alpha_z \cdot t} \tag{3.19}$$

where

$$\alpha_{\pm} = \delta \frac{\omega_{\pm}}{\omega_+ - \omega_-} \qquad and \tag{3.20}$$

$$\alpha_z = \frac{\delta}{2}. \tag{3.21}$$

(A)   (B)
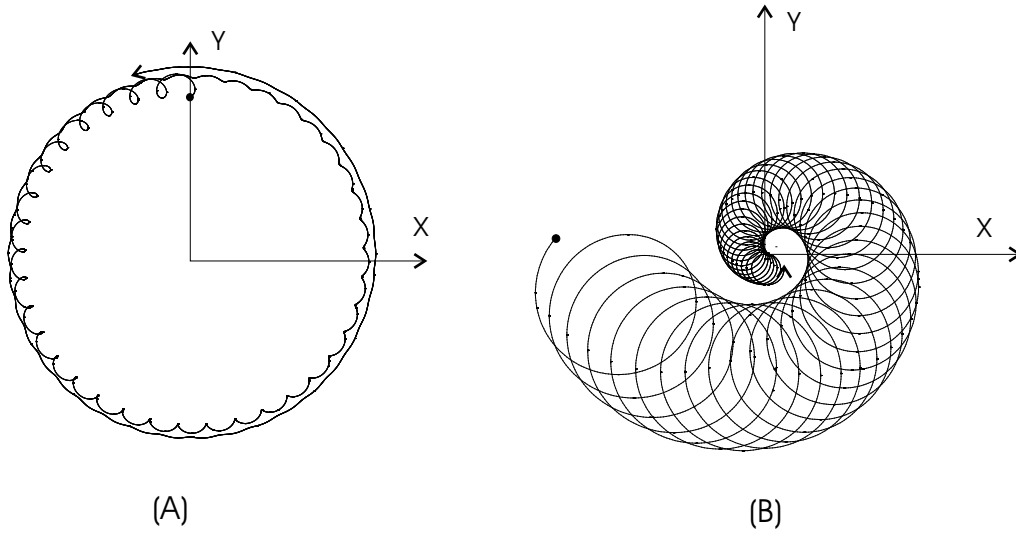
Figure 3.4: Influence of the buffer gas and quadrupolar radiofrequency field on the ion motion in a Penning trap. The ion motion in the plane perpendicular to the magnetic field is shown. The start of the ion motion is indicated by a full dot. **A**: The presence of buffer gas results in fast cooling of the reduced cyclotron motion and a slow increase of the magnetron amplitude. **B**: In addition, an RF quadrupole excitation is applied at the pure cyclotron frequency ω_c. The coupling of the two motions slows down the cooling of the reduced cyclotron motion, but reduces the magnetron orbit. The final result is centering of the ion.

$A_i(0)$ are the initial amplitudes of the different eigenmotions. The amplitudes of the reduced cyclotron motion $A_+(t)$ and of the axial motion $A_z(t)$ decay exponentially. At the same time the amplitude of the magnetron motion $A_-(t)$ grows exponentially with time. This effects is shown in Fig. 3.4(A) for the reduced cyclotron and magnetron motions. The ions are lost, when the magnetron amplitude is larger than the size of the trap electrodes. This can be overcome by coupling the reduced cyclotron and the magnetron motion through a radiofrequency quadrupole field at the pure cyclotron frequency of the ions with frequency

$$\omega_{RF} = \omega_+ + \omega_- = \omega_c = \frac{q}{m} \cdot B. \qquad (3.22)$$

The oscillating azimuthal quadrupole field created via a four-fold segmented ring electrode is given by [Bollen90]

$$\overrightarrow{E_x} = E_q \cdot \cos \omega_{RF} t \cdot y \hat{e}_x \qquad and \qquad \overrightarrow{E_y} = E_q \cdot \cos \omega_{RF} t \cdot x \hat{e}_y. \qquad (3.23)$$

Here ω_{RF} is the excitation radiofrequency, and E_q is given by

$$E_q = C_2 \cdot U_{RF}. \qquad (3.24)$$

C_2 is a constant depending on the geometry of the trap, and U_{RF} is the RF voltage applied to the segmented ring electrode.

A transverse cut of a segmented ring electrode to apply a quadrupole field inside a Penning trap is shown in Fig. 3.3(B). Without quadrupole excitation, the buffer gas leads to fast damping of the reduced cyclotron amplitude, while the magnetron orbit increases slowly, as shown in Fig. 3.4(A). Finally the ions are lost by hitting the trap electrodes. By applying a RF quadrupole field at the pure cyclotron frequency ω_c the two motions are coupled. This leads to conversion from the slow magnetron motion into the fast reduced cyclotron motion. Since the fast reduced cyclotron motion is effectively damped by buffer gas collisions the net effect is a reduction of both amplitudes, i.e. the centering of the ion cloud, as shown in Fig. 3.4(B). Since ω_c depends on the charge-to-mass ratio (q/m-ratio), this centering effect is mass selective and can be used, for example, to get rid of unwanted isobars.

3.2.3   Quadrupole excitation without buffer gas

A mass measurement in a Penning trap is performed by measuring the cyclotron frequency of the stored ions. To measure the cyclotron frequency one of the main steps is to convert the magnetron energy into the reduced cyclotron energy. This can be obtained by applying a quadrupole excitation to the ion motion at their pure cyclotron frequency. In this case a periodic conversion between the two motions (magnetron and reduced cyclotron motions) will take place which is discussed below.

Equation (3.7) can be written for x and y coordinates separately by

$$\ddot{x} - \frac{qU_0}{2 \cdot md^2} \cdot x - \frac{q}{m}B \cdot \dot{y} = 0 \qquad (3.25)$$

and

$$\ddot{y} - \frac{qU_0}{2 \cdot md^2} \cdot y - \frac{q}{m}B \cdot \dot{x} = 0. \qquad (3.26)$$

For the quadrupole excitation shown in Fig. 1.4(B) the potential in the radial plane is given by

$$U = \frac{U_{RF}}{r_0^2} \cos(\omega_{RF}t + \theta_{RF})(x^2 - y^2), \qquad (3.27)$$

where U_{RF}, ω_{RF} and θ_{RF} are the amplitude, the frequency and the phase, respectively. The resulting force is

$$\vec{F} = \frac{U_{RF}}{r_0^2} \cos(\omega_{RF}t + \theta_{RF})(2x\vec{e_x} - 2y\vec{e_y}), \qquad (3.28)$$

which transforms the Eqs. (1.25) and (1.26) in

$$\ddot{x} - \omega_c\dot{x} - (\frac{\omega_z^2}{2} + 2\frac{qU_{RF}}{md^2}\cos(\omega_{RF}t + \theta_{RF}))x = 0 \qquad (3.29)$$

and

$$\ddot{y} - \omega_c \dot{y} - (\frac{\omega_z^2}{2} - 2\frac{qU_{RF}}{md^2}\cos(\omega_{RF}t + \theta_{RF}))y = 0. \tag{3.30}$$

The analytical solutions of Eqs. (3.29) and (3.30) are evaluated in detail in [Bollen90, König95]. Finally the amplitude of the reduced cyclotron motion and the amplitude of the magnetron motion at a time t are given by

$$A_+(t) = [A_+(t=0)\cos(\omega_B t) - \frac{1}{2}\frac{A_+(t=0)[i(\omega_{RF} - \omega_c)] + A_-(t=0)k_0 e^{i\Delta\theta}}{\omega_B}\sin(\omega_B t)]e^{i\frac{1}{2}(\omega_{RF}-\omega_c)} \tag{3.31}$$

and

$$A_-(t) = [A_-(t=0)\cos(\omega_B t) - \frac{1}{2}\frac{A_-(t=0)[i(\omega_{RF} - \omega_c)] + A_+(t=0)k_0 e^{-i\Delta\theta}}{\omega_B}\sin(\omega_B t)]e^{i\frac{1}{2}(\omega_{RF}-\omega_c)} \tag{3.32}$$

with

$$\omega_B = \frac{1}{2}\sqrt{(\omega_{RF} - \omega_c) + k_0^2}, \tag{3.33}$$

$$k_0 = 2\frac{qU_{RF}}{mr_0{}^2}\frac{1}{(\omega_+ - \omega_-)}, \tag{3.34}$$

and

$$\Delta\theta = \theta_{RF} - (\theta_+ + \theta_-). \tag{3.35}$$

If $\omega_{RF} = \omega_c$ Eqs. (1.31) and (1.32) will be

$$A_+(t) = A_+(t=0)\cos\frac{k_0}{2}t - A_-(t=0)e^{i\Delta\theta}\sin\frac{k_0}{2}t. \tag{3.36}$$

and

$$A_-(t) = A_-(t=0)\cos\frac{k_0}{2}t + A_+(t=0)e^{-i\Delta\theta}\sin\frac{k_0}{2}t. \tag{3.37}$$

Equations (3.31) and (3.32) show the general case of the coupling between the magnetron and the reduced cyclotron motion and Eqs. (3.36) and (3.37) that for the particular case when $\omega_{RF} = \omega_c$. Thus in a certain time interval, as the reduced cyclotron amplitude increases, the magnetron amplitude decreases. For example, if at time t = 0 the magnetron amplitude $A_-(t=0)$ = R and the reduced cyclotron amplitude $A_+(t=0) = 0$, the reduced cyclotron amplitude will be maximum after half a period and the magnetron amplitude will be zero. This conversion of the motion is illustrated in Fig. 3.5.

The change in the ion's motion involves a change in the radial kinetic energy of the ion in the trap. The total radial kinetic energy $E_r(t)$ at a time t is given by

(A)   (B)
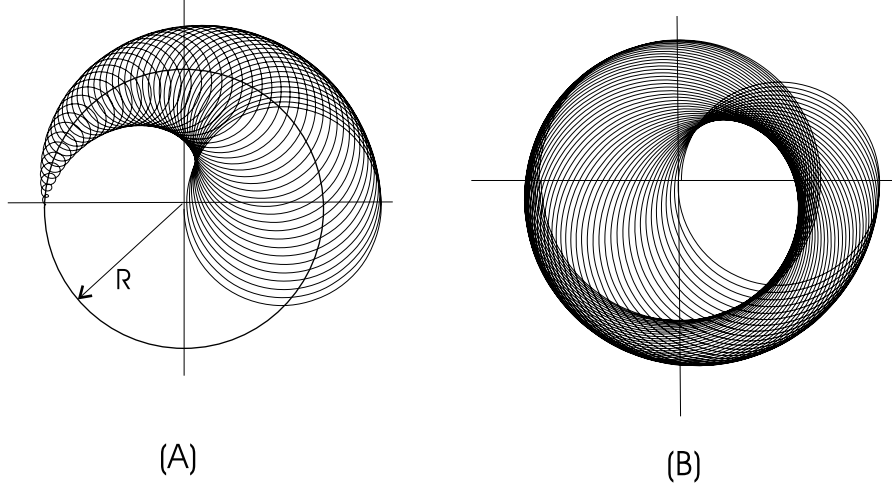
Figure 3.5: Conversion of the radial motions of an ion in a Penning trap due to the application of an external radiofrequency field. **A**: At time t = 0, the magnetron amplitude A_- equals R and the reduced cyclotron amplitude is zero. The magnetron motion is converted to the reduced cyclotron motion with an quadrupole RF field at $\omega_{RF} = \omega_c$. **B**: When a full conversion is obtained, the amplitude of the reduced cyclotron motion equals R whereas the magnetron amplitude is zero. This conversion is periodic.

$$E_r(t) = \frac{1}{2}m[\omega_+^2 A_+(t)^2 + \omega_-^2 A_-(t)^2]. \tag{3.38}$$

It will be maximum when $A_+(t) = $ R and $A_-(t) = 0$, i.e. when the ion's motion is fully converted into a reduced cyclotron motion (see Fig. 3.5). In this condition the radial kinetic energy of the ion is given by

$$E_r(t) = \frac{1}{2}m\omega_+^2 R^2. \tag{3.39}$$

From Eqs. (3.34), (3.36) and (3.37) the required time for a full conversion T_{conv} is given by [König95]

$$T_{conv} = \frac{2n+1}{U_{RF}}(\omega_+ - \omega_-)\frac{mr_0^2}{2q}, (n = 0, 1, 2.....). \tag{3.40}$$

If the excitation time is longer than T_{conv} then the ion's motion will start again to convert to pure magnetron motion. At $T_{RF}=2 \cdot T_{conv}$ the ion is back to a pure magnetron motion. This conversion is periodic.

When $\omega_{RF} \neq \omega_c$, the resulting cyclotron amplitude after applying the quadrupole field for a time T_{conv} is not at a maximum, hence the radial kinetic energy is smaller compared to that given by the Eq. (3.39). In such a condition the difference between

the magnetron radial energy and the reduced cyclotron radial kinetic energy is given by (from Eqs. (3.38)) [König95]

$$\Delta E_r(t) = \frac{1}{2}m[\omega_+^2 A_+(t)^2 - \omega_-^2 A_-(t)^2].$$ (3.41)

This can be written as

$$\Delta E_r(t) = \frac{1}{2}qBR_0[\omega_+ - \omega_-],$$ (3.42)

when $A_-(t) = A_-(t) = R_0$ and $R_0 < R$. The difference of the two radial energies at a ω_{RF} can be expressed as [König95]

$$\Delta E_r(\omega_{RF}) = \frac{q^2 U_{RF}^2}{2mR^4} \frac{\omega_+^2}{(\omega_+ - \omega_-)^2} \frac{\sin^2(\omega_B T_{RF})}{\omega_B^2},$$ (3.43)

where ω_B is given by Eq. (3.33). This results in a resonance curve with side bands. The full width at half maximum of the resonance is given by [König95]

$$\Delta \nu(FWHM) = \frac{0.8}{T_{RF}}.$$ (3.44)

3.3 Real Penning trap

A real Penning trap differs from the ideal one in a number of ways. Some of these imperfections are very important and have to be taken into account to avoid possible systematic errors in the mass measurements. A review of the most important effects is discussed below. A detailed description is given by G. Bollen and R.B. Moore [Bollen90] and by L.S. Brown and G. Gabrielse [Brown86].

3.3.1 Deviation from an ideal quadrupole field

A real Penning trap involves geometrical imperfections like finite size and truncations of the electrodes which result in an electric field slightly different from the ideal quadrupole field as described by equation (3.2). Close to the trap center the electric potential can be expressed as a sum of Legendre polynomials by

$$U(r,\theta) = \frac{U_0}{2} \sum_{0,even}^{\infty} C_k (\frac{r}{d})^k P_k(\cos\theta),$$ (3.45)

with

$$r = \sqrt{z^2 + \rho^2},$$ (3.46)

where C_k are the multipole component coefficients. For an ideal harmonic potential inside the Penning trap only C_2 is non-zero. The deviations from the harmonic potential come from higher-order terms, mainly the octupole and the dodecapole ($k = 4$ and 6) terms. This leads to frequency shifts of the eigenmotions [Bollen90]

$$\Delta(\omega_+ + \omega_-)^{(4)} = \frac{3C_4}{4z_0^2} \frac{\omega_z^2}{(\omega_+ + \omega_-)} (\rho_+^2 - \rho_-^2) \tag{3.47}$$

and

$$\Delta(\omega_+ + \omega_-)^{(6)} = \frac{15C_6}{8z_0^4} \frac{\omega_z^2}{(\omega_+ + \omega_-)} [3z^2(\rho_+^2 - \rho_-^2) + (\rho_+^4 - \rho_-^4)] \tag{3.48}$$

where z is the amplitude of the axial oscillation, and ρ_+ and ρ_- are the radii of the reduced cyclotron and magnetron motions, respectively. From the above equations it is noticed that the frequency shifts $\Delta\omega_c^{(4)}$ and $\Delta\omega_c^{(6)}$ are mass independent. The anharmonicity of the trapping potential can be reduced by introducing correction electrodes between the end and ring electrodes and by applying appropriate potentials to them.

3.3.2   Effect of magnetic field inhomogeneities

There are two sources which cause magnetic field inhomogeneities, first the finite extent of the solenoidal windings creating the magnetic field and, secondly, the distortion of this magnetic field by the magnetic susceptibility of the material forming the trap electrodes as well as the vacuum tube. The magnetic field close to the center of the trap can be expressed approximately by [Bollen90]

$$B_z = B_0[1 + \beta_2(z^2 - \frac{\rho^2}{2})] \tag{3.49}$$

where β_2 is the strength of the quadratic component of the magnetic field. The frequency shift due to this inhomogeneity is

$$\Delta(\omega_+ + \omega_-) = \beta_2 B_0 \frac{q}{m} [z^2 - \frac{\rho_+^2}{2}(1 - \frac{\omega_c}{\omega_+ - \omega_-}) - \frac{\rho_-^2}{2}(1 + \frac{\omega_c}{\omega_+ - \omega_-})], \tag{3.50}$$

which, in the approximation $\omega_c \approx \omega_+ - \omega_-$, gives

$$\Delta(\omega_+ + \omega_-) = \beta_2 B_0 \frac{q}{m} [z^2 - \rho_-^2]. \tag{3.51}$$

In order to minimize this effect it is therefore necessary to reduce the β_2 component and to keep the amplitude of the ion motion small. To reduce the magnetic susceptibility copper metal is chosen to form the trap electrodes. It is also important to construct the trap electrodes in such a way that the material are symmetrically distributed.

3.3.3   Misalignment

Great care has to taken for the alignment of the trap electrodes with respect to the axis of the superconducting coil. Such a misalignment will cause a cyclotron frequency shift, which is given by [Bollen90]

$$\Delta\omega_c \approx \frac{V_0}{d^2 B}[-\frac{1}{4}\epsilon^2 + \frac{9}{8}\theta^2], \tag{3.52}$$

where θ is the angle between the magnetic field and the trap axis at the trap center and ϵ is the electric field ellipticity. If there is no electric field ellipticity then this will reduce to

$$\Delta\omega_c \approx \frac{9}{4}\omega_- \sin\theta^2. \tag{3.53}$$

The deviation $\Delta\omega_c$ due the magnetic field misalignment is described in details in reference [Bollen90].

3.3.4 Space charge effects

Space charge effects are observed in a Penning trap if a large number (of the order 10^6 or more) of ions is present inside the trap [Yu89]. If a large number of ions of the same species is present in the trap then the Coulomb interaction between them can shift the eigenfrequencies. The magnitude of this effect is proportional to the number of trapped ions. A large trap volume is useful in order to reduce space charge effects. When more than one species are present in the trap, the center-of-mass motions of the species interact. As a result the cyclotron frequencies are shifted. Therefore, high-accuracy mass measurements in a Penning trap require that there is no contaminant ion and the number of stored ions is small.

3.3.5 Orthogonalised cylindrical Penning trap

A Penning trap with cylindrical electrodes is a promising alternative to the conventional traps with hyperbolic electrodes even for high precision experiments. The trapping potential of such a Penning trap is created by applying a DC voltage to the cylindrical electrodes (see Fig. 3.1,B). To achieve an almost ideal quadrupole potential in a cylindrical penning trap the voltage applied to the correction electrodes needs to be tuned. This tuning voltage applied to the correction electrodes depends on the trap geometry i.e. on the r_0/z_0 ratio [Gabrielse84, Gabrielse89]. The term "orthogonalised" emphasizes that for such a cylindrical trap, the axial oscillation frequency of the trapped ions is independent of small changes in the voltage applied to the correction electrodes. The advantage of the cylindrical Penning trap is that it can be constructed more easily than a hyperbolic one. Furthermore the cylindrical structure eases injection and extraction of ions.

3.4 Mass measurement techniques

In Penning trap mass spectrometry as described here the mass of a charged particle is determined by a measurement of its cyclotron frequency

$$\omega_c = \frac{q}{m} \cdot B \tag{3.54}$$

in a magnetic field B, where the magnetic field is calibrated by the cyclotron resonance of an ion of well known mass. There are two techniques to determine the cyclotron frequency of charged particles in a Penning trap: The time-of-flight Ion Cyclotron Resonance (TOF-ICR) measurement and the Fourier Transform-Ion Cyclotron Resonance (FT-ICR). In the present set-up at SHIPTRAP/GSI the TOF-ICR technique is used, but in the future it will be complemented by the non-destructive FT-ICR technique to detect even ions with very low production rates.

3.4.1   Time-of-flight Ion Cyclotron Resonance (TOF-ICR)

The cyclotron frequency of charged particles in a Penning trap can be determined by measuring the time of flight (TOF) between the trap and a detector outside the strong magnetic field. A schematic diagram for TOF measurements is shown in Fig. 3.6. When a radiofrequecy quadrupole field at a frequency $\omega_{RF} = \omega_c$ is applied to the segmented ring electrode a coupling between the reduced cyclotron motion and the magnetron motion takes place [Bollen90], resulting in a periodic conversion from one motion to the other, as discussed in the previous section. During this conversion the slow magnetron motion changes to the fast reduced cyclotron motion with higher radial energy and the orbital magnetic moment of the ions increases. The magnetic moment of an ion orbiting in a magnetic field is given by

$$\mid \overrightarrow{\mu} \mid = I \times \pi R^2, \tag{3.55}$$

where $I = q\omega/(2\pi)$ is the current generated by a charged particle moving in a closed orbit with radius R and an area πR^2. In the resonance case ($\omega_{RF} = \omega_c$), after a full conversion of the motions is performed, the magnetic moment of an ion in a Penning trap is given by

$$\overrightarrow{\mu} = \left(\frac{1}{2} q \omega_+ R^2 \right) \overrightarrow{e}_z = \frac{E_r}{\mid \overrightarrow{B} \mid} \overrightarrow{e_z}, \tag{3.56}$$

where E_r is the radial energy of the ion. The magnetic moment is maximum when the ion perform a pure reduced cyclotron motion. So a full conversion of magnetron motion into reduced cyclotron motion is needed. The total energy of the ion in the trap is given by the sum of the radial energy and axial energy

$$E_{total} = E_r + E_z = \mu B + \frac{1}{2} m \omega_z^2 z^2, \tag{3.57}$$

or

$$E_{total} = \frac{1}{2} m \omega_+^2 R^2 + \frac{1}{2} m \omega_z^2 z^2. \tag{3.58}$$
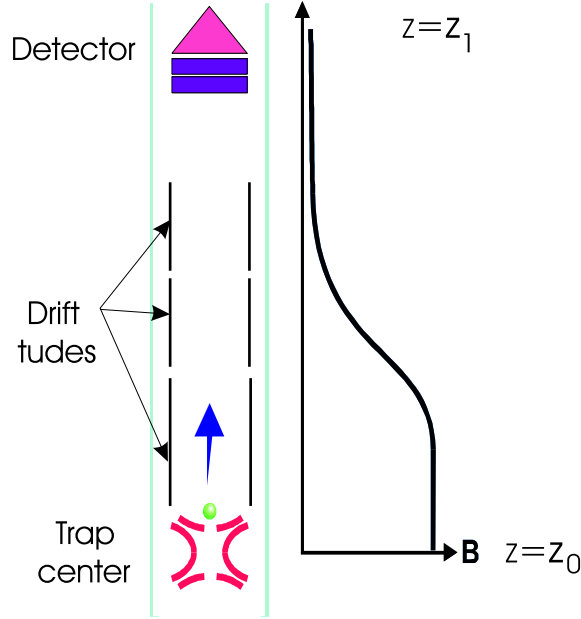
Figure 3.6: Schematic diagram of the time-of-flight method for measuring the cyclotron frequency. The ions are ejected from the trap, drift through the inhomogeneous magnetic field region and are then detected by a micro-channel plate detector. The trap center is at $z = z_0$ where the magnetic field is homogeneous and strong. The detector is at $z = z_1$ where the magnetic field is almost zero.

After the RF excitation the charged particles are ejected from the trap. They drift towards the detector through a drift tube where a strong magnetic field gradient exists. Here the ions experience an axial force given by

$$\overrightarrow{F_z} = -\overrightarrow{\nabla}(\overrightarrow{\mu} \cdot \overrightarrow{B}) = \overrightarrow{\mu}\frac{\delta B}{\delta z}, \tag{3.59}$$

due to the interaction of the magnetic moment of the radial ion motion with the negative gradient of the inhomogeneous magnetic field. Since the total energy of the ion motion is constant, radial energy is converted into axial energy when the ion is ejected out of the trap to a region with vanishing magnetic field. This results in an acceleration in axial direction and a time of flight given by [König95]

$$t(\omega_{RF}) = \int_{z_0}^{z_1} \sqrt{\frac{m}{2[E_{total} - qU(z) - \mu B(z)]}}dz. \tag{3.60}$$

Here z_0 is the coordinate of the trap center and z_1 is the location of the detector. B(z) is the strength of the magnetic field along the axial direction and U(z) represents an eventual electrostatic potential along the flight path. The difference between the time of flight $TOF(\omega_{RF} = \omega_c)$ of an ion in resonance to that of an ion off resonance $TOF(\omega_{RF} \neq \omega_c)$ is defined as TOF-effect, expressed as
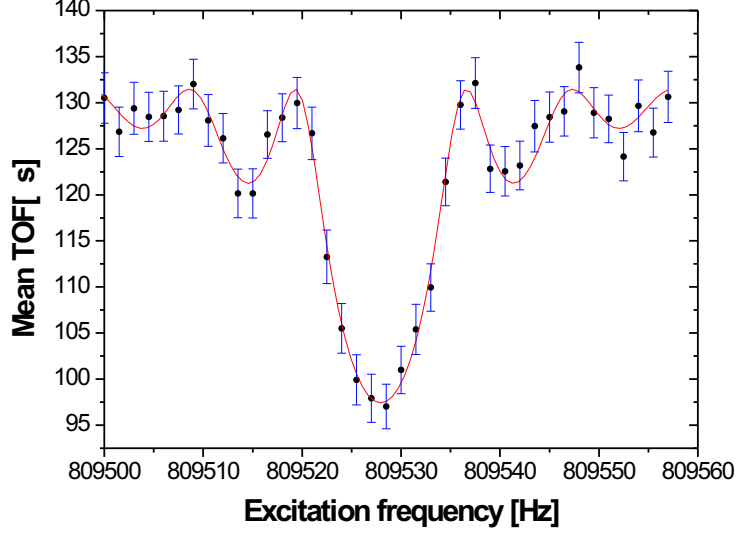
Figure 3.7: Time-of-flight cyclotron resonance for ^{133}Cs measured with the SHIP-TRAP set-up. The time of flight of the ions from the trap to the detector is plotted as a function of the applied excitation frequency. The points are experimental data fitted by the theoretical line shape. For this particular measurement the excitation time was 100 ms. The width of the resonance is about 10 Hz.

$$TOF_{effect} = \frac{TOF(\omega_{RF} \neq \omega_c) - TOF(\omega_{RF} = \omega_c)}{TOF(\omega_{RF} \neq \omega_c)}. \tag{3.61}$$

By measuring the time of flight as a function of the applied excitation frequency, the cyclotron frequency of the ion under investigation and its mass are obtained.

As an example, Fig. 3.7 shows the mean time of flight as a function of the applied excitation frequency for singly-charged ^{133}Cs ions. The experimentally obtained data points match with the theoretically expected line shape given by Ref. [König95].

3.4.2   Fourier Transform Ion Cyclotron Resonance (FT-ICR)

The Fourier Transform Ion Cyclotron Resonance method is a non-destructive technique to identify ions in a Penning trap by observation of their modified cyclotron frequency ω_+ [Brown86,Comisarow86,Stahl98]. This method is mainly used to study chemical reactions or to identify macromolecules by their characteristic mass pattern. Usually, 100 to 1000 ions are required to observe a signal. For FT-ICR detection the ions are excited by an RF dipole field at their reduced cyclotron frequency ω_+. A schematic diagram for the determination of the reduced cyclotron frequency ω_+ is shown in Fig. 3.8.

Two opposite segments of the ring electrode are used to excite the ions, and the other
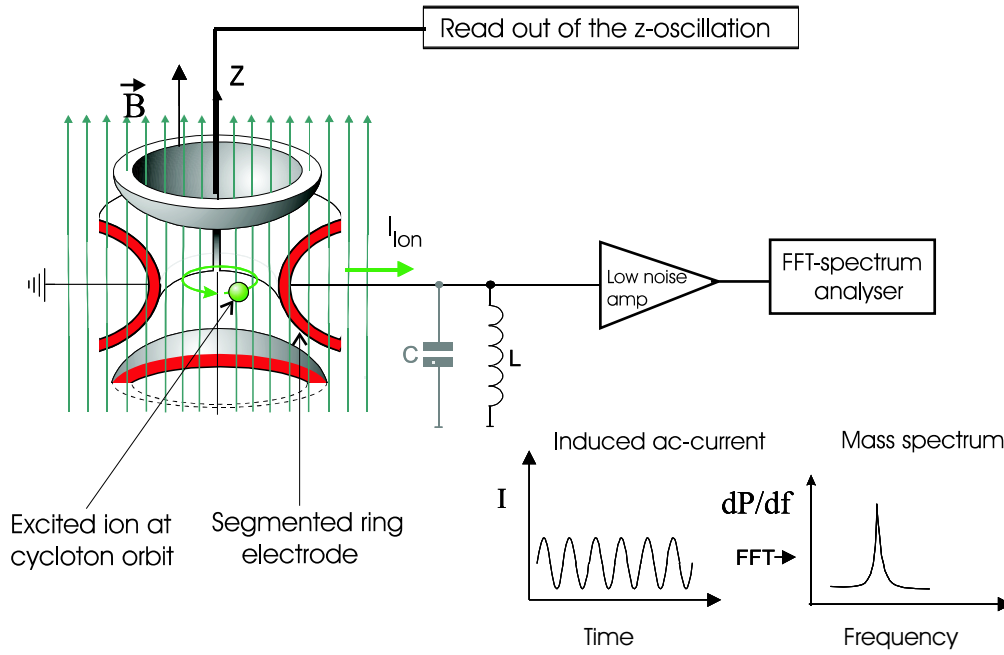
Figure 3.8: Schematic diagram of Fourier Transform-Mass Spectrometry with a tuned circuit for single-ion detection [Stahl98]. The particles excited by RF in the Penning trap induce image currents on the segmented ring electrode and the end caps which are read out, amplified and Fourier transformed.

two segments to detect the image current which is induced by the motion of the trapped charged particles. Also the axial motion ω_z is observed via an image current induced in the endcap electrodes. From the invariance relation (see Eq. 1.9) ω_c can be calculated by the use of

$$\omega_- = \frac{\omega_z^2}{2\omega_+}. \tag{3.62}$$

The small induced currents of a single ion can be detected by using a resonance circuit with high quality factor Q_{LC}. This is done by coupling an inductance L parallel to the trap electrode which is used as a pick-up electrode and the circuit. Choosing the inductance L the circuit can be operated in resonance with the ion oscillation frequencies $\omega_{LC} = 1/\sqrt{LC} = \omega_+$ or ω_z, respectively, where C is the stray capacitance of the pick-up electrode and the circuit. In the resonance case, high amplification can be reached. However, the disadvantage of this scheme is that only one specific frequency or isotope can be measured. This can be overcome by employing a tunable circuit, where the resonance frequency can be shifted by changing the circuit components. Finally, the signal at the resonance circuit is amplified by a low-noise amplifier.

In the following, the expected signal-to-noise ratio of the signal induced by the modified cyclotron motion of a single ion will be calculated. The induced signal S for an ion is given by

$$S = U_{induced} = I_{ion} \cdot R, \tag{3.63}$$

where R is the parallel resistance of the resonance circuit

$$R = \frac{Q_{LC}}{\omega_+ \cdot C}. \tag{3.64}$$

Here Q_{LC} is the quality factor of the LC circuit and ω_+ is the reduced cyclotron frequency. The quality factor Q_{LC} of the resonance circuit is defined by

$$Q_{LC} = \frac{\omega_+}{\Delta\omega_+(FWHM)} \tag{3.65}$$

with $\Delta\omega_+$ the full width at half maximum. The induced current on the trap electrodes is given by

$$I_{ion} = \frac{1}{\sqrt{2}} \cdot \frac{r_{ion}}{D} \cdot q \cdot \omega_+ \tag{3.66}$$

where r_{ion} is the radius of the ion orbit, q is the charge state, and D is the minimum radius of the ring electrode. Then the signal S is

$$S = \frac{1}{\sqrt{2}} \cdot \frac{r_{ion}}{D} \cdot \frac{q}{C} \cdot Q_{LC}. \tag{3.67}$$

The signal increases with the amplitude of the orbit of the ion, with the Q-value of the circuit, but decreases for a larger trap geometry. The thermal (Johnson) noise of the circuit [Hill89] is given by

$$N = \sqrt{4kT \cdot R \cdot \Delta\nu_+}, \tag{3.68}$$

where k is Boltzmann's constant, T the temperature and $\triangle\nu_+$ the bandwidth of the actual signal. The signal-to-noise ratio for a single ion is then given by

$$\frac{S}{N} = \frac{\sqrt{\pi}}{2} \cdot \frac{r_{ion}}{D} \cdot q \cdot \sqrt{\frac{\nu_+}{\Delta\nu_+}} \cdot \sqrt{\frac{Q_{LC}}{kTC}}. \tag{3.69}$$

In order to detect the signal of a single ion, S/N must be larger than one, therefore the quality factor Q_{LC} must be high, the temperature low, and the capacitance C small. For SHIPTRAP a set-up is under construction, with the trap at 77 K and an external superconducting resonance circuit at 4 K [Stahl98]. With this cryogenic set-up it is estimated that the power signal-to-noise ratio will be enough to detect a single trapped heavy ion. For more details about design and construction of the cryogenic set-up see [Weber04].

Chapter 4

The SHIPTRAP facility

The ion trap facility SHIPTRAP [Dilling00, Sikler03a] is coupled to the Separator for Heavy Ion reaction Products (SHIP) at GSI/Darmstadt. The scientific program covered by this facility includes precision mass measurements, nuclear spectroscopy, the study of ion chemical reactions and laser spectroscopy of heavy elements. The advantage of the SHIPTRAP facility is that it offers access to transuranium elements which are not accessible to other trap facilities. A detailed overview of all elements and techniques that have been developed for SHIPTRAP is presented in this chapter.

4.1 SHIPTRAP: experimental set-up

The SHIPTRAP facility is situated behind SHIP, where heavy radionuclides are produced in fusion reactions. The experimental set-up consists of mainly three parts shown in Fig. 4.1. The first one is a gas-filled stopping cell, which is used to stop the reaction products coming from SHIP. It is followed by a radiofrequency quadrupole structure to extract the ions from the stopping cell. The second part, a buffer gas filled RFQ buncher, allows for cooling, accumulating and bunching of ions from the stopping cell. It provides a low emittance bunched ion beam which can be efficiently injected into the Penning trap system. The third part, a Penning trap system, consists of two cylindrical Penning traps. The first one is a purification trap, where mass selective buffer gas cooling is applied for isobaric purification. Finally, the ions are transferred to a second Penning trap, the measurement trap, where precision mass measurements can be performed by the time-of-flight ion cyclotron resonance technique.

Figure 4.1 shows a schematic layout of the SHIPTRAP facility indicating the three main parts and their typical operating pressure. In Fig. 4.2 a technical drawing shows the detailed layout of the vacuum system. The positions of the turbo pumps for each section as well as their pumping speed is indicated. For the Penning trap system the pumps are placed one meter below the beam line since the magnetic field strength close to the superconducting magnet is about 50 Gauss, which can affect the magnetic bearing of the pumps. Micro-channel plate (MCP) and Faraday cup (FC) detectors are placed at different positions in the beam line for diagnosis. MCP1, MCP2, FC1
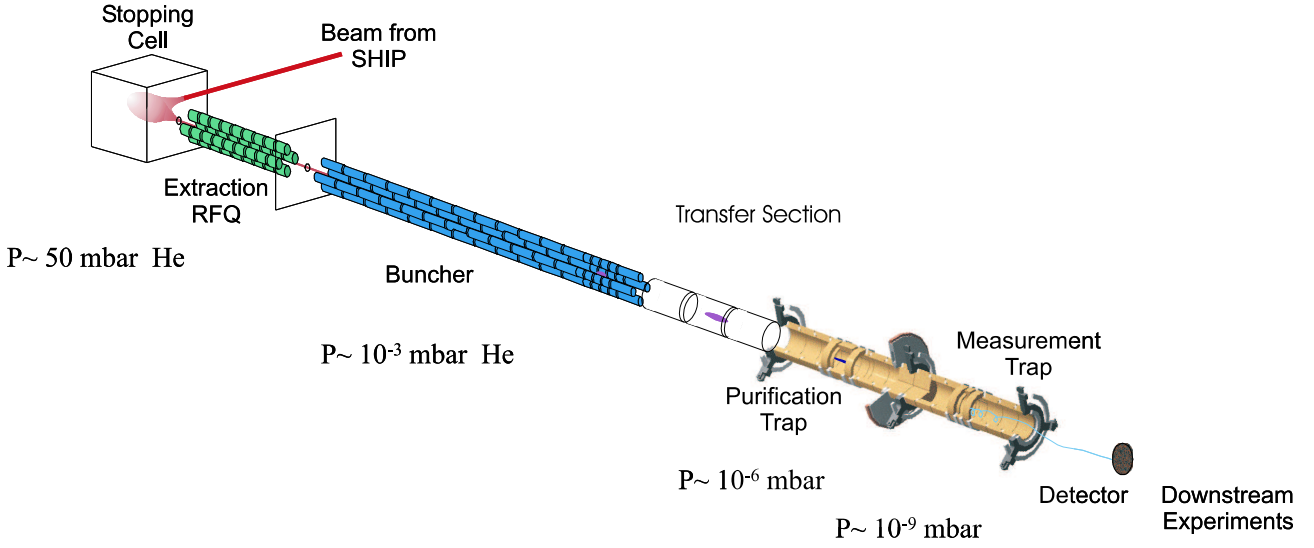
Figure 4.1: Schematic layout of SHIPTRAP. The three main parts are the gas-filled stopping cell for stopping the reaction products coming from SHIP together with the extraction RFQ, the RFQ buncher for cooling and bunching of the ions, and a double Penning trap system for isobaric purification and precision mass measurements. Typical pressures are indicated.

and FC2 detectors are mounted on a movable feedthough which allows to take it in and out from the beam line according to the necessity.
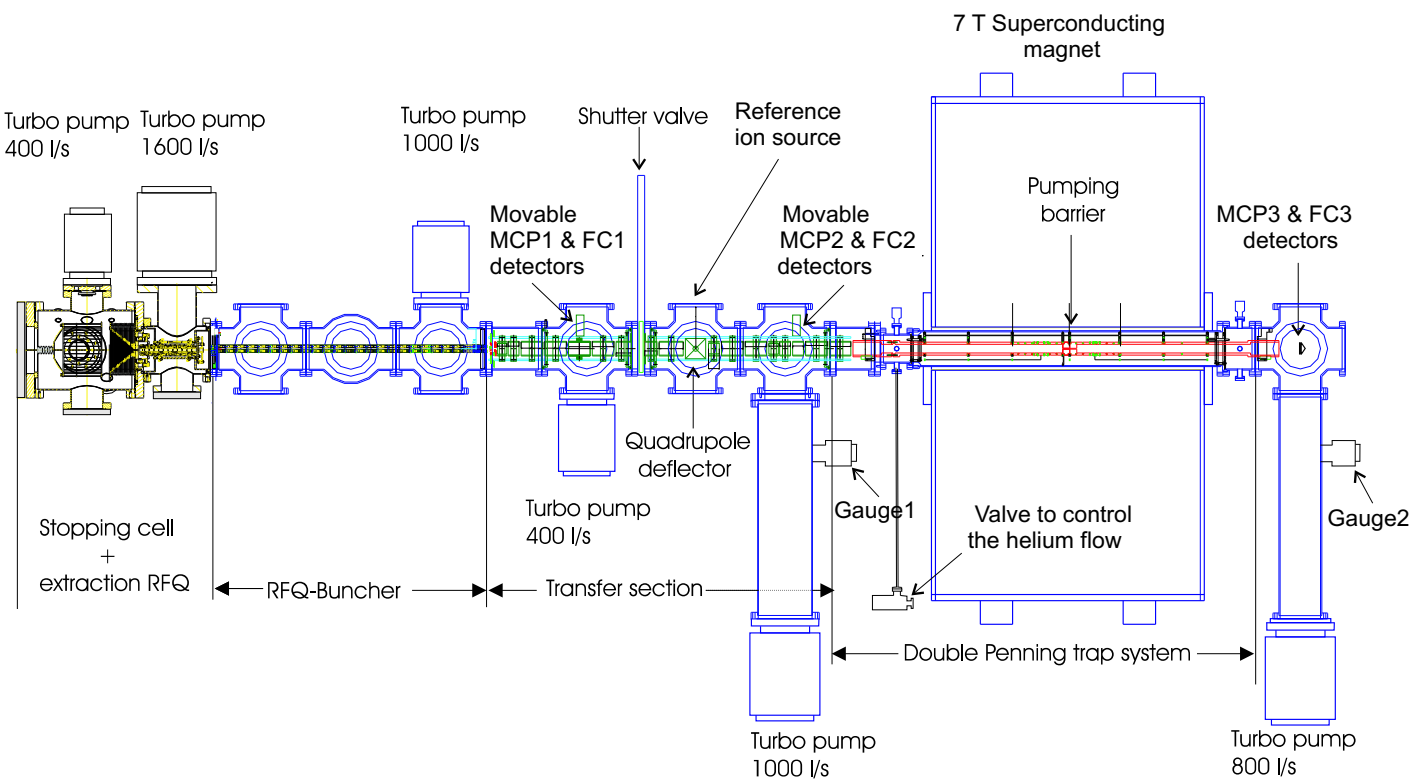
Figure 4.2: Technical drawing of the SHIPTRAP set-up showing a detailed layout of the vacuum system. The position of the turbo-molecular pumps and their pumping speeds are shown. The micro-channel plate (MCP) and Faraday cup (FC) detectors are placed at different positions in the beam line for beam diagnosis.

Turbo pump 400 l/s

Turbo pump 1600 l/s

Turbo pump 1000 l/s

Shutter valve

Reference ion source

7 T Superconducting magnet

Movable MCP1 & FC1 detectors

Movable MCP2 & FC2 detectors

Pumping barrier

MCP3 & FC3 detectors

Quadrupole deflector

Gauge1

Valve to control the helium flow

Gauge2

Stopping cell + extraction RFQ

RFQ-Buncher

Transfer section

Turbo pump 400 l/s

Double Penning trap system

Turbo pump 1000 l/s

Turbo pump 800 l/s

4.1.1 The gas-filled stopping cell

The SHIPTRAP gas-filled stopping cell [Neumayr04] with a length of about 450 mm and diameter of 250 mm is designed to accept the full SHIP beam of dimension 50×30 mm^2. Figure 4.3 shows the stopping cell together with the extraction RFQ. They are connected by a nozzle with an inner diameter of about 0.6 mm. The helium gas in the cell can stop heavy ions with an energy of up to 500 keV/u (in front of the entrance window) at a pressure of about 42 mbar. The window foil is supported by a grid of wires since it maintains the high pressure difference between the stopping cell and the vacuum of the SHIP beam line. It is made of pinhole-free Al, Ti or Ni foils with 60 mm diameter and a thickness of a few μm.
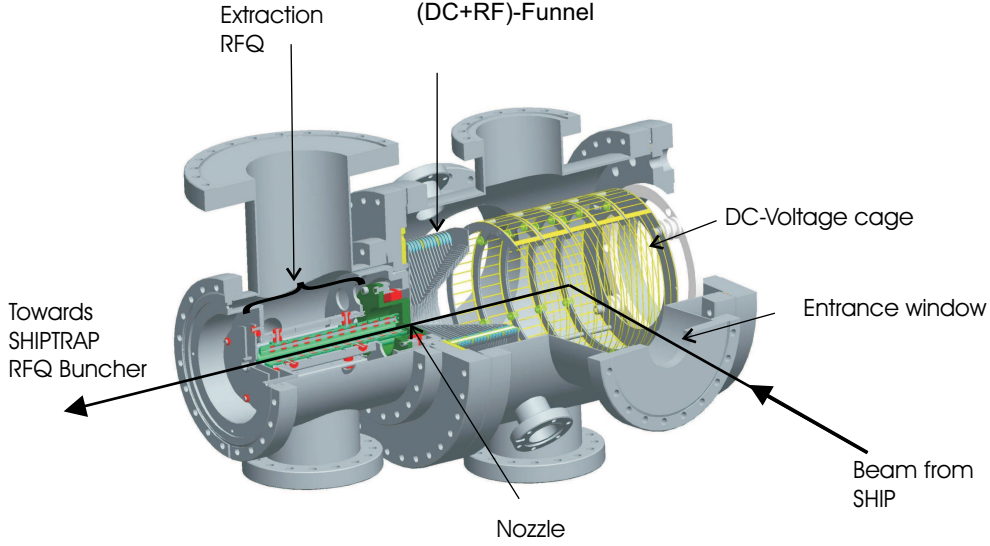
Figure 4.3: Stopping cell and extraction RFQ. For details see text.

Any impurities inside the stopping cell reduce the extraction efficiency of the stopped ions by molecule formation, recombination or charge exchange. Therefore, great care has been taken to increase the extraction efficiency by maintaining UHV conditions before its operation and using very clean helium gas during the operation. To drag the stopped ions out of the stopping cell, DC potentials are applied to a cage electrode system to guide the ions towards a funnel-shaped system of 40 ring electrodes which are installed in front of the nozzle. The voltage applied to the funnel consists of both RF and DC components to achieve better focusing and acceleration of the ions towards the nozzle. The RF potential is applied to the funnel with a phase shift of 180° between two adjacent ring electrodes, to create a RF wall to reduce ion loss by hitting the funnel electrodes. Through the nozzle the ions are extracted via the gas flow. Both sides of the nozzle have a conical shape. It is optimized to achieve a supersonic gas jet for an effective transfer of the ions into the extraction RFQ. The purpose of the extraction RFQ is to guide the ions and to transfer them from the stopping cell into the buncher,

while the helium gas is pumped away. The extraction RFQ consists of four rods with a total length of about 180 mm. Each rod is axially divided into 12 segments to create a longitudinal DC potential.

In order to determine the stopping and extraction efficiency of the stopping cell and extraction RFQ, on-line measurements were performed using stable and radioactive ions at the accelerator facilities of the Maier-Leibnitz Laboratory (MLL) at Garching and at GSI/Darmstadt. The experiment at MLL was performed with a longitudinal extraction of the stopped ions from the stopping cell, while at GSI the extraction of the stopped ions was performed almost at perpendicular direction with respect to the injection [Neumayr04].

The on-line measurements at MLL were performed using radioactive ^{152}Er ions produced in the reaction ^{121}Sb(^{35}Cl,4n). The efficiency of the stopping cell was determined by the ratio between the number of detected α-decays in front of the stopping cell and behind the extraction RFQ. A maximum efficiency (including stopping and extraction) of 8.4% $\pm$ 1.5% was achieved. The on-line measurement at GSI was performed with the same isotope ^{152}Er produced via the reaction ^{116}Sn(^{40}Ar,4n). A maximum efficiency (including stopping and extraction) of 4.8% $\pm$ 0.7% was obtained. An efficiency of 2.7% $\pm$ 0.4% was observed including the RFQ buncher (see Fig. 4.1). The results of the efficiency measurements at MLL and at GSI are summarized in Tab. 4.1. A detailed description and the measurement procedure is presented in reference [Neumayr04].

Table 4.1: Results of the efficiency measurements of the stopping cell performed at Maier-Leibnitz Laboratory (MLL) and GSI. The extraction fields applied to the cage electrode system (DC) and to the RF funnel are indicated. The extraction angle was 0° at MLL and 90° at GSI.

Place	Test ion	Efficiency %	Extraction fields V/cm DC / funnel	Extraction angle
MLL	^{152}Er, α-emitter	8.4±1.5	10 / 10	0°
GSI	^{152}Er, α-emitter	4.8±0.7	10 / 5	90°
MLL	^{107}Ag$^+$, atomic-ions	4.0±1.0	5 / 10	0°

4.1.2   The RFQ buncher

The SHIPTRAP RFQ buncher is an one meter long radiofrequency quadrupole structure consisting of four rods, which is operated at a buffer gas pressure of typically 5×10^{-3} mbar. The rods are divided longitudinally into 29 segments shown in Fig 4.4 (Top). The diameter of each rod is 9 mm and the distance between two opposite rods is 7.86 mm [Rodríguez02]. The ions are radially confined in the pseudo-potential well of the RF quadrupole field while their radial and longitudinal energy is reduced in collisions with the buffer gas atoms. As the kinetic energy of the ions is dissipated, they are dragged along the ion guide by an axial DC field applied to the segmented
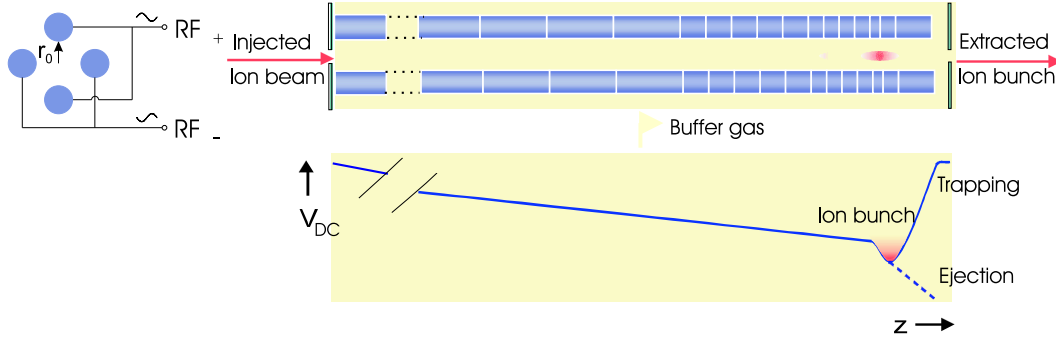
Figure 4.4: Top: Side view of the radiofrequency ion beam cooler and buncher. Bottom: The DC potential slope V_{DC} is shown along the symmetry axis with a harmonic trap at the end.

rods. In the minimum at the end of the RFQ buncher shown in Fig. 4.4 (bottom), a large number (up to about 10^3) of ions can be accumulated. After accumulation and cooling over several milliseconds, the axial potential is lowered to extract a narrow ion bunch.

The SHIPTRAP RFQ buncher system is operated with no radial DC potential, i.e. with the dimensionless parameter $a = 0$. The stability condition depends only on the RF amplitude, i.e. the q value. For Ar^+ the q value is about 0.57 for an RF amplitude of 60 V_{pp} and a radiofrequency of 950 kHz [Rodríguez02]. Typically the width of an ion bunch is about a few μs. The longitudinal emittance was measured to be below 5 eVμs. The transverse emittance, normalized to an energy of 2.5 keV, was determined to be 20 $\cdot \pi mm \cdot mrad$. In measurements done with argon ions an efficiency in bunch mode of about 40 percent was achieved after 50 ms storage time. A dependence of the trapping efficiency on the axial DC potential, on the RF amplitude, and on the ion species was observed. These measurements are described in detail in [Rodríguez02]. The system can also be operated in continuous mode as an ion guide. In this mode the ions are passing through the system continuously and a transmission efficiency of the system of about 95 percent was achieved.

4.1.3   The Penning trap

The third part of the set-up is a double Penning trap system in one superconducting magnet of 7 Tesla field strength. The cooled and low-emittance ion bunch from the buncher is transferred to the purification Penning trap where isobaric separation is performed applying the buffer gas cooling technique. Then the clean ion sample is transported to the measurement Penning trap where a precision mass measurement is performed by the time-of-flight technique. A detailed description of the Penning traps will be presented in the next chapter.

Chapter 5

The SHIPTRAP Penning trap system

The SHIPTRAP facility uses two Penning traps. Both are cylindrical and placed in the same superconducting magnet of 7 Tesla field strength. This chapter describes the layout of the traps and the technical improvements that have been done during the commissioning period for a better efficiency and resolution of the system. A very similar trap system JYFLTRAP was realized in close collaboration with the SHIPTRAP group and is used at Jyväskylä at the IGISOL facility [Kolhinen03].

5.1   The experimental set-up

The Penning trap part of the SHIPTRAP facility together with the reference ion source is shown in Fig. 5.1. It consists of a surface ion source, a quadrupole deflector, two cylindrical traps and two micro-channel plate (MCP) detectors. The surface ion source is placed in the first vacuum cross (see Fig. 5.1) together with a quadrupole deflector. A transfer line consisting of up-down, left-right deflectors and cylindrical electrodes is used to transfer the ions to the trap. In a second vacuum cross (see Fig. 5.1) a movable MCP detector and a Faraday cup detector is placed to measure the ion current before injecting into the Penning trap. A turbo pump (Pfeiffer TMU 1000MC) is connected in order to get the required pressure in the purification trap. An ion gauge (IONIVAC) labelled as Gauge 1 for the pressure measurement is placed below the cross. The second vacuum cross and the superconducting magnet are connected by a small connector cross. The electrical feedthroughs to connect the purification trap electrodes to the power supply are placed here. To inlet buffer gas into the purification trap, a clean helium feeding line is installed. An electronic valve (BALZERS EVR 116) allows for the regulation of the helium pressure inside the purification trap. Two cylindrical Penning traps are placed inside the same superconducting magnet. They are separated by a diffusion barrier to achieve a sufficient pressure difference between the two traps. The superconducting magnet and the detector vacuum cross are connected by the same kind of connector cross where the electrical feedthroughs for the measurement
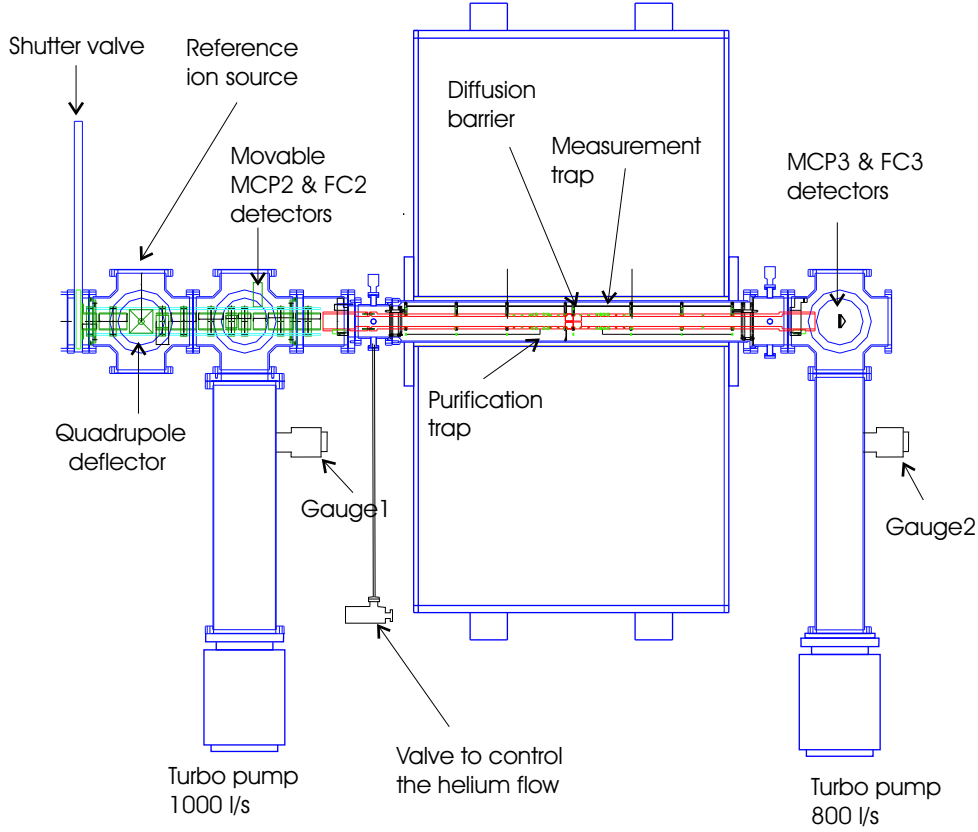
Figure 5.1: Part of the experimental set-up as used for commissioning measurements of the Double Penning trap system at SHIPTRAP. The main components are indicated.

trap electrodes are situated. Inside the detector cross a Faraday cup detector and a MCP detector are placed to detect the ions ejected from the trap. A turbo pump (SEIKOSEIKI 800MC) is connected to get the required pressure in the measurement trap. An ion gauge (IONIVAC) labelled as Gauge 2 is placed below the detector cross to measure the pressure on the measurement trap side.

5.1.1   Description of the Penning traps

Figure 5.2 (top) shows a transverse cut of the SHIPTRAP Penning trap system. The Penning trap system consists of two cylindrical traps in one superconducting magnet (see Fig. 5.1) with a field strength of 7 Tesla. The superconducting magnet has two homogeneous regions at the center, where the traps are placed. The homogeneous magnetic field regions are marked by arrows in Fig. 5.2 (bottom). The distance between the trap centers is 200 mm.

The first trap is used as purification trap. The inner diameter of the trap is 32 mm and the length is about 212 mm. The trap design is based on the ISOLTRAP cooler trap, which is a seven-electrode cylindrical trap [Hartmann97]. It consists of a pair of end
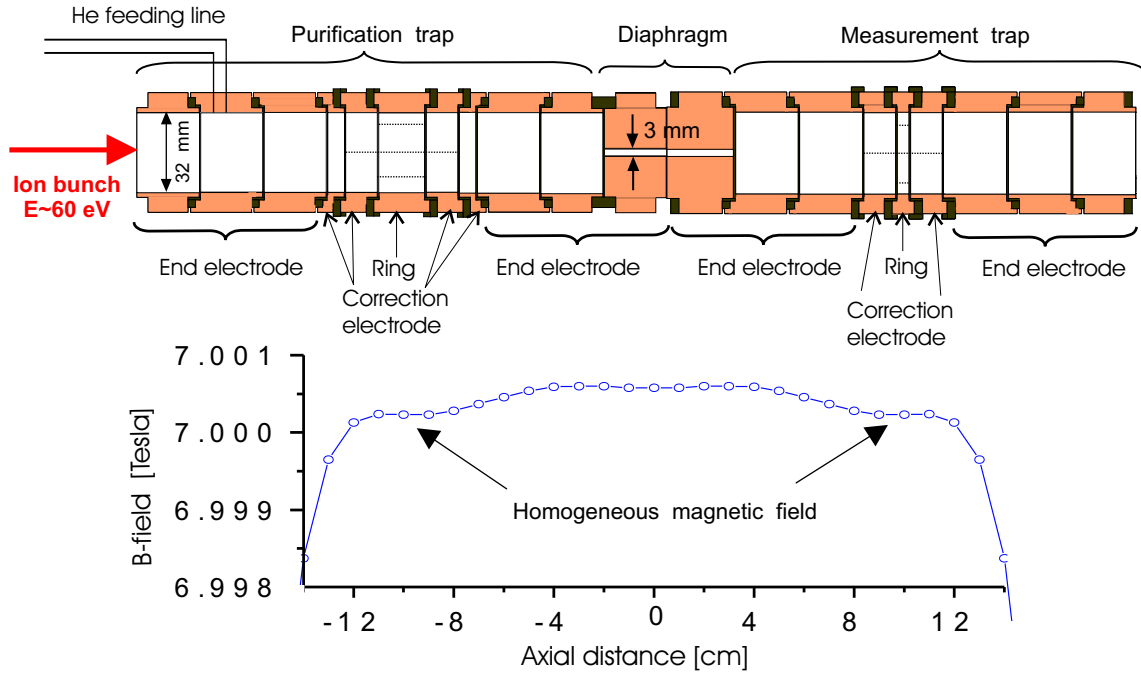
Figure 5.2: Top: Penning trap system. The left one is the purification trap with a ring electrode, a pair of end electrodes and two pairs of correction electrodes. The right one is the measurement trap with a ring electrode, a pair of end electrodes and one pair of correction electrodes. A diffusion barrier (diaphragm) with a length of 50 mm and an inner diameter of 3 mm separates the two traps for differential pumping. The trap electrodes are made of oxygen-free copper indicated in dark gray. The insulator rings are made of aluminium oxide indicated in black. **Bottom**: Magnetic field plot of the superconducting magnet (MAGNEX SCIENTIFIC MRBR 7.0/160/as) along the symmetry axis.

electrodes, two pairs of correction electrodes and a ring electrode. Each end electrode is axially three-fold segmented to apply different DC potentials to create an extended potential well for efficient capture of the ions. The inner correction electrodes are divided into two segments in the azimuthal plane. In this way it is possible to apply a quadrupole field by using all four segments in order to couple the z-oscillation with one of the radial oscillations. The ring electrode is azimuthally divided into eight segments. This allows for the excitation of different motions in various configurations (dipole or quadrupole) for different purposes.

The second Penning trap, the measurement trap, is also cylindrical with the same inner diameter and a length of about 185 mm. It is a five-electrode trap. It consists of a pair of end electrodes, one pair of correction electrodes and a ring electrode. The end electrodes are again divided into three rings to apply different DC potentials. The

correction electrodes are divided into two segments to have a flexibility to apply the quadrupole field by using all four segments in order to couple the z-oscillation with one of the radial oscillations. To apply the RF-fields as required for the excitation of the ion motion, the ring electrode is azimuthally divided into eight segments. The eight-fold segmented ring electrode offers the possibility to excite the trapped ions by an octupole RF field at $2\omega_c$. The second trap is used for high-precision mass measurements. The two traps are separated by an orifice for differential pumping, which is 50 mm long and has a diameter of 3 mm. For more details about design and construction of the trap system see [Sikler03a, Rahaman02].

All the trap electrodes are made of oxygen-free high conductivity (OFHC) copper. The copper electrodes are gold-plated to avoid oxidization which can distort the electric field. Between the copper surface and the gold layer is a silver layer to prevent the diffusion of gold into the copper. The insulators between the electrodes are made of aluminium oxide (Al_2O_3). The thickness of the cylindrical trap electrodes is 8 mm and the distance between two electrodes is 0.5 mm.

To measure the pressure in the both traps two vacuum gauges are placed outside the superconducting magnet as shown in Fig. 4.1. Gauge 1 and Gauge 2 give the pressure of the purification trap and the measurement trap, respectively. From calculations it is known that the pressure in the trap is about 50 times larger than the measured pressure in the gauge. When pressures in the traps are given in the text the pressure indicated on the display of the vacuum gauges is cited.

5.1.2 Helium gas feeding line to the trap
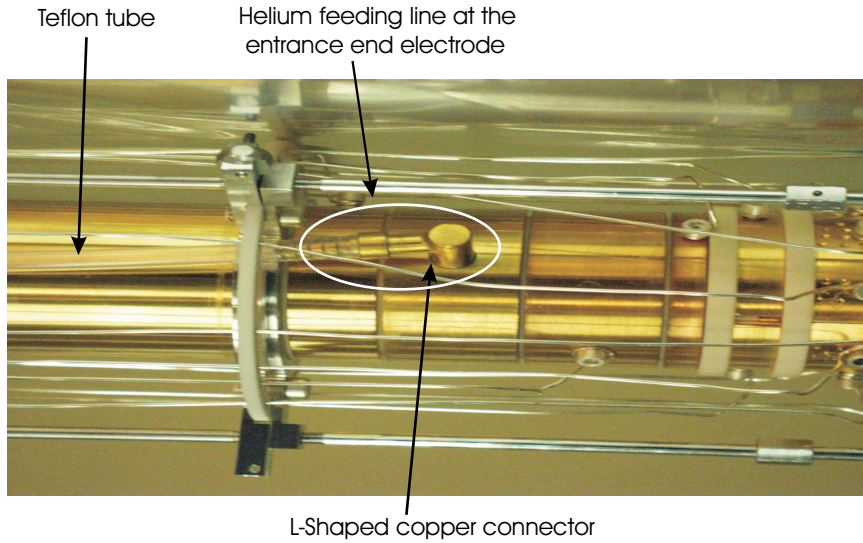
Figure 5.3: Photo of the helium feeding line: A teflon tube is connected to the center of the entrance end electrode of the Purification trap.

A photo of the buffer gas line inside the vacuum is shown in Fig. 5.3. The gas line is connected to the middle part of the entrance end electrode (see Fig. 5.2 top). This helps to get an optimum pressure gradient at the center of the trap, which is needed for mass selective buffer gas cooling. A teflon tube is connected to the trap electrode by a L-shaped copper connector. The inner diameter of the tube is 5.2 mm. A feedthrough on a CF40 flange connects the teflon tube inside the vacuum to a stainless steel tube outside the vacuum. A helium gas bottle with a purity of 99.9998% is connected through a commercial gas purification system (SAES Getters PSGC50R2) via a stainless steel tube to the electronic valve. This electronic valve is used to control the helium flow to the purification trap which is regulated via a controller (BALZERS EVR 300).

5.1.3   The reference ion source

A surface ion source which is typically used for cesium or rubidium together with an extraction system and an electrostatic cylindrical electrode is mounted in the first cross (see Fig. 5.1) on a CF100 flange. The ion source is based on surface ionization. In a surface ion source, the ionization mechanism is the interaction with a hot surface. The ionization potential of the atoms to be ionized (i.e cesium or rubidium) must be lower than the work function of the surface material. Hence it works for elements with low ionization potential (<5-6 eV), i.e., alkalis and alkaline earths. The metal surface is heated indirectly via a current passing through a filament. At temperatures sufficiently high to evaporate the alkali, ions are produced. The number of produced ions (cesium or rubidium) is increases with the surface temperature controlled by the filament current. The ionizer can be floated at any given voltage (typically 90 V or 61 V) to define the energy of the produced ions. For normal operation the required filament current is about 9 Ampere. At this filament current a cesium current about 30 pA is detected on a Faraday cup detector (FC2 see Fig. 5.1) in front of the Penning trap. This ion source was used for the testing of the Penning trap system.

5.1.4   Electronics

A circuit was designed to apply an external radiofrequency quadrupole field to the segmented ring electrode of the Penning trap. Figure 5.4 shows a complete circuit diagram to get two radiofrequency signals at 180 degree phase difference with the same amplitude and frequency at OUT 1 and OUT 2. V2 and V3 are used as power supply for the operational amplifier which require supply voltages of at least ± 4 V up to ± 15 V. The operational amplifier AD811AN was chosen because of its high bandwidth (140 MHz, 3dB at gain = 1) and its very high slew rate (2500 V/μs). Another voltage supply V1 is used to provide the offset voltage (± 2V).

The ring electrode of the Penning trap is at 60 V but for the excitation of the ion motions a radiofrequency has to be applied to the segmented ring electrodes. So it is required to couple the DC voltage to the radiofrequency. For this a coupling circuit is designed shown in Fig. 5.5. The resistance and the capacitor of the circuit are chosen
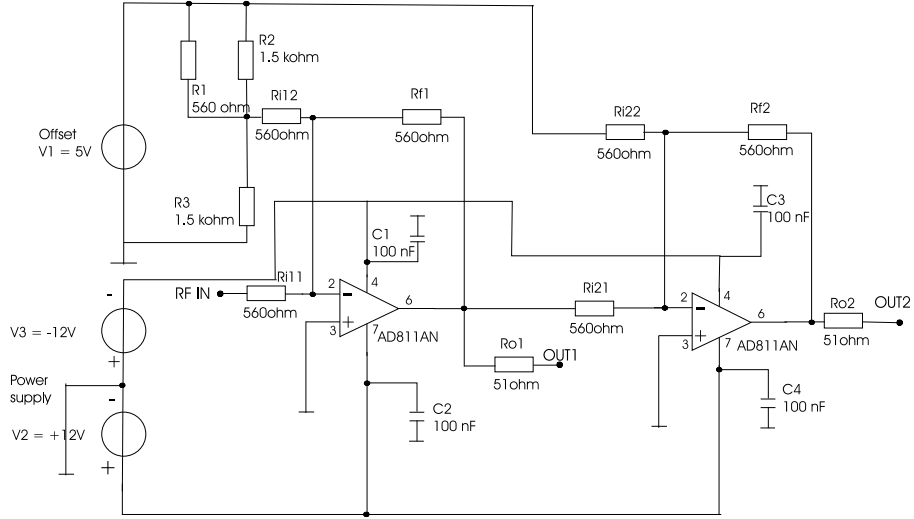
Figure 5.4: Circuit diagram for excitation of the ions in the trap. The input radiofrequency is split in to two parts with same amplitude and frequency but opposite phase at OUT1 and OUT 2.
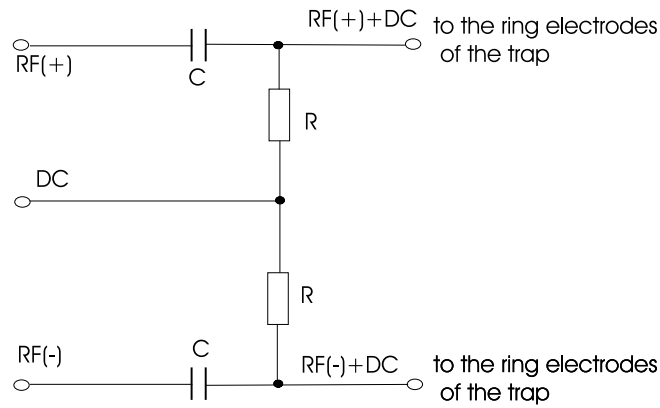
Figure 5.5: The circuit diagram to couple the radiofrequency and the DC voltage. RF(+) and RF(-) indicate the different radiofrequency phases.

such that the time constant is of the order of a microsecond which permits to pass the required frequency. The values of the resistances and the capacitors used to couple the radiofrequency which is of the order of kHz (necessary for magnetron excitation) are 33 kΩ and 10 nF. The values of the resistances and the capacitors used to couple the radiofrequency which is of the order of MHz (necessary for cyclotron excitation) are 20 kΩ and 4.7 nF respectively.

5.2 The detector and control system

5.2.1 Detector

To detect the ions before injection into and after ejection out of Penning trap, micro-channel plate (MCP) detectors are used at different places of the the beam line (see Fig. 5.1). A micro-channel plate consists of an array of glass channels (or capillaries) with 10-12 μm inner diameter, coated on the inside with an electron-emissive material. It is a compact electron multiplier. Incoming ions hit the micro-channel plate and produce secondary electrons.
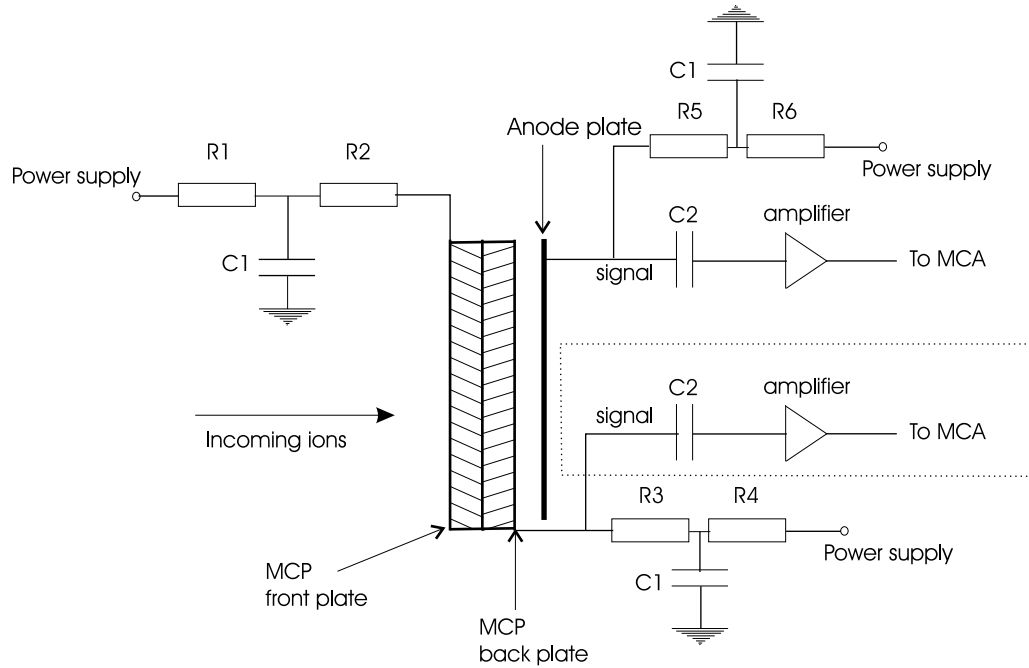
Figure 5.6: Micro-channel plate detector consisting of two micro-channel plates (MSP) and a segmented anode plate. Voltages are applied to the MCPs and to the segmented anode plate via an appropriate low-pass filter. The electronic signal is readout from the anode plate. In the dotted box the optional readout of the signal from the back micro-channel plate is shown.

These electrons are accelerated by the electric field through the channels and in each

collision several secondary electrons are generated. Finally, a large number of electrons emerge from the output side of the micro-channel plate. To collect these electron avalanches an anode plate is used after the micro-channel plates and the electrical signal is readout from this plate (Fig. 5.6). The electronic signal can also be readout from the back plate of the MCP as indicated in Fig. 5.6 by a dotted box.

The complete detector-set at SHIPTRAP (Topag MCP-MA34) consists of two micro-channel plates [Fraser02, Tremsin96] of 34 mm diameter and 460 μm thickness and a segmented anode. Two MCPs and the anode are assembled together in a metal ceramic housing. They are matched in a V-stack assembly and connected to each other via a copper foil ring of 40-50 μm thickness. A gain factor of $10^6 - 10^7$ can be achieved depending on the potential difference between the two micro-channel plates. In normal operation maximum 1 kV per channel is recommended. The voltage applied to the front plate of the MCP is -1850 V and the back plate is kept at ground potential. The voltage applied to the anode plate is about 150 V. These voltages are delivered by a power supply (CAEN N470). The resistances $R_i = 1$ kΩ and the capacitors $C_1 = 10$ nF form a low pass filter to reduce the noise from the high voltage power supply. The capacitor $C_2 = 4.7$ nF is used to decouple the electronic signal and the DC potential applied to the anode.

5.2.2 Control system and measurements cycle

A LabVIEW (presently version 7.1) based control system for the SHIPTRAP facility has been implemented using the Control System (CS) framework [Beck04]. CS is an object-oriented, multi-threaded and event-driven framework with Superiority Control And Data Acquisition (SCADA) functionality. It allows one to control many distributed devices for an experiment and to collect the data at the same time. Presently the SHIPTRAP control system uses about 200 active objects that are distributed over four PCs.

Figure 5.7 shows a simplified design of the SHIPTRAP control system, based on the CS framework. Solid bordered boxes with rectangular corners in Fig. 5.7 represent hardwire like PCs or devices. Solid bordered boxes with round corners denote active objects that are mainly software. Dashed bordered boxes with round corners represent the driver for the different devices. Arrows indicate events or direct method calls. The "Sequencer" and the Graphic User Interfaces (GUI) derived from the "BaseProcess" class are experiment specific add-ons. All other classes are part of the CS framework. The "Control GUI" sends the parameters needed to set the "Sequencer" which creates and parameterizes the objects required. Then it starts the Pulse Pattern Generator ("PPG100_1"), which produces pulses. These pulses are then used to trigger the devices and to synchronize the actions with a resolution of 100 ns. Then the "Sequencer" calls the "Data Collector" which reads the buffer data from the data acquisition devices like "DS430_1". "DS430_1" is connected to the "Data Collector". The "Disc Archiver" is connected to the "Data Collector", which retrieves and writes the data to the disc. The "Online Analysis GUI" is used to analyze and display the data to user. All the
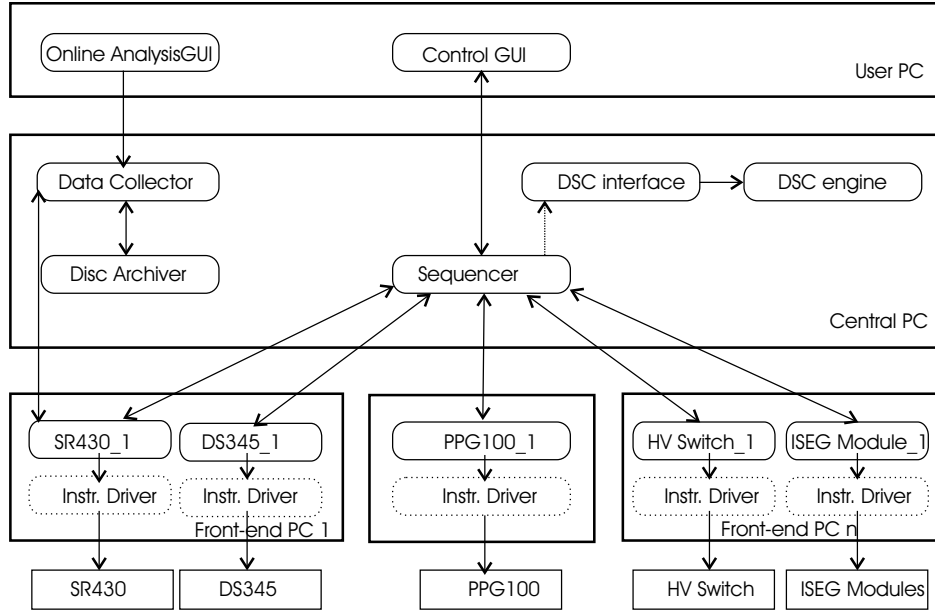
Figure 5.7: Simplified view of the SHIPTRAP control system. Solid bordered boxes with rectangular corners represent hardwire like PCs or devices. Solid bordered boxes with round corners denote active objects that are mainly Software. Dashed bordered boxes with round corners represent the driver for the different devices. The direction of the arrows do not indicate the direction of the data flow but mark between the caller and calli.

objects send their status and error information to the "DSC interface" (Datalogging & Supervisory Control) which is an object for trending and alarming.

Measurement cycle

The experimental measurement procedure consists of cycles and scans. A scan consists of many cycles, and a cycle is one complete measurement sequence for one specific value of frequency, voltage or time. The cycle is repeated from the lower start value to the higher stop value of frequency, voltage or time with a period depending on the half-life of the radioactive elements. For example, one such cycle to excite the ions in the trap at one frequency value is described in the following.

Figure 5.8 shows a schematic layout of the connection from the different devices to the trap electrodes used for the quadrupole excitation of ions in the purification trap. All the devices are connected to the various front-end PCs (see Fig. 5.7). The same schematic is applicable for the measurement trap. First, the time sequence is set by the PPG100 for a measurement cycle. This cycle includes: capturing and exciting the ions in the purification trap, transporting them into the measurement trap, exciting the ions in the measurement trap and then finally ejecting them from the measurement trap to the detector. Then a high voltage switch is triggered by the PPG100 for the
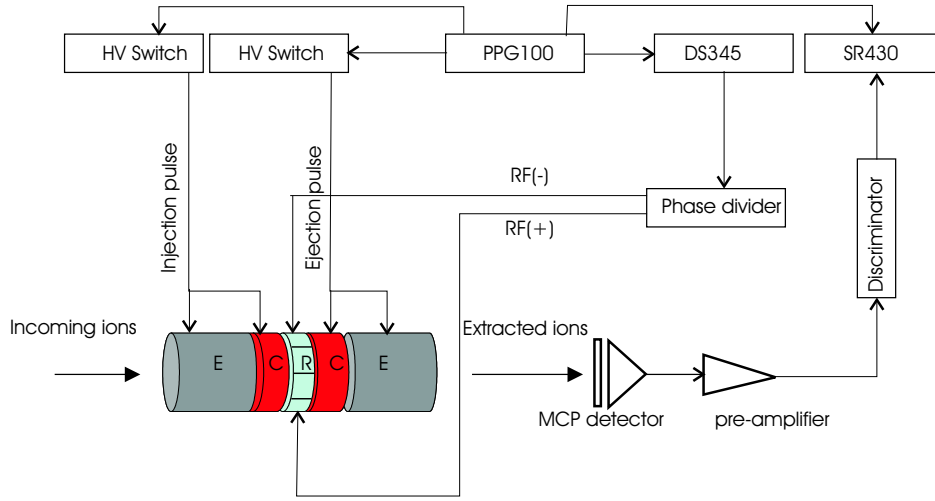
Figure 5.8: Schematic layout of the connection from the devices to the trap electrodes for the example of quadrupole excitation of the ions in the purification and measurement trap. All the devices are connected to the different front-end PCs (see Fig. 5.7). E: end electrode, C: correction electrode, R: ring electrode.

injection pulses. After setting the pulse height for injection, the pulses are applied to the entrance electrode (E) and correction electrode(C) of the trap. Then after 200 ms a function generator (DS345) is triggered to create an excitation radiofrequency which passes through a phase divider from where the excitation radiofrequency is applied with 180^0 phase shift to two opposite segments of the ring electrode for the dipole excitation. From another function generator the excitation radiofrequency is applied with same phase to two opposite segments of the ring electrode and with 180^0 phase to the another opposite segments of the ring electrodes for quadrupole excitation. Afterwards an ejection pulse is applied to the end electrode (E) and correction electrode (C) of the trap to extract the ions from the purification trap. Then in the same way the measurement trap is loaded and excitation is performed. Finally, an ejection pulse is applied to the end electrode (E) and correction electrode (C) of the measurement trap to extract the ions from the measurement trap. The electronic ion signal is readout from the detector, amplified and discriminated for the analysis in the multichannel scaler (SR430). In this way the complete cycle is repeated for different frequency values to complete one scan.

Chapter 6

Characterization and Optimization of the Penning traps

The cylindrical double Penning trap system of SHIPTRAP was extensively tested for a full characterization and to obtain a set of optimum operating parameters. The off-line tests of the Penning trap system were performed using cesium ions from the surface reference ion source located after the buncher in the second vacuum cross of the transfer section (see Fig. 4.2). The working principle of the ion source was described in the previous Chapter in Section 5.1.3.

The vacuum tube was aligned relative to the magnetic field inside the bore of the superconducting magnet. In the first step the injection of ions into the magnetic field and the transmission through both Penning traps, and the extraction out of the magnet were studied. The operation of the purification trap was optimized. In this trap the mass-selective buffer gas cooling technique is used for isobaric separation. The proper harmonic potential shape was chosen for trapping and storing the ions in the trap. The identification of stable cesium ions was demonstrated by measuring their cyclotron frequency. At present a mass resolving power of about $\frac{m}{\Delta m} = 85,000$ was achieved. Afterwards the cooled and centered ions from the purification trap were transferred to the measurement trap. A characterization of the measurement trap has also been performed in the course of this work. This trap is used for precision mass measurements. The identification of the cesium ions was demonstrated by measuring their cyclotron frequency via the time-of-flight technique. A mass resolving power of about $\frac{m}{\Delta m} = 860,000$ was achieved for ^{133}Cs^{+}. In this chapter a set of optimum operating parameters will be presented for both traps.

6.1 Magnetic-field alignment

The alignment of the vacuum tube with respect to the magnetic field was done with the help of an electron gun. The vacuum tube was aligned and hence the set of trap electrodes was aligned with respect to the magnetic field. The electron gun was placed at the center of the superconducting magnet. The two four-fold segmented Faraday
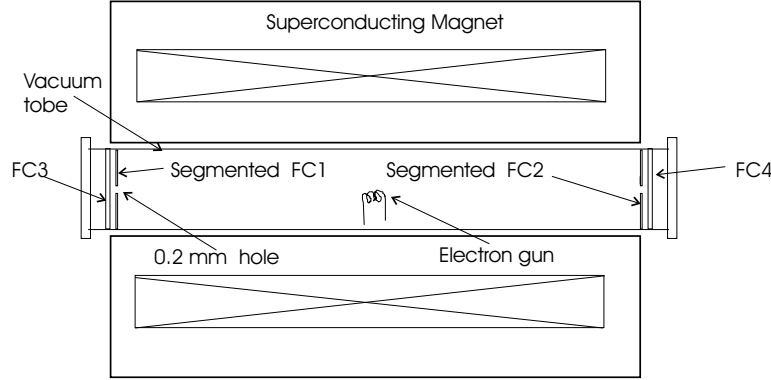
Figure 6.1: A: Schematic layout of the set-up for alignment of the vacuum tube with respect to the magnetic field. FC1 and FC2 are four-fold segmented Faraday cup detectors with a 0.2 mm hole at the center. FC3 and FC4 is Faraday cup detectors, to detect the current passing through 0.2 mm hole of FC1 and FC2. At the center of the vacuum tube an electron gun is placed.

cup FC1 and FC2 detectors (with a 0.2 mm hole at the center) were placed at the end positions of the superconducting magnet. Behind each of the segmented Faraday cup detectors another two Faraday cup FC3 and FC4 detectors were placed to detect the electron passing through the 0.2 mm hole of FC1 and FC2. A schematic drawing of the set-up is shown in Fig. 6.1.

The electron current distribution on the FC is made as much as possible uniform on all FC segments and at the same time the electron current passing through the 0.2 mm hole is maximized. This was done by moving the superconducting magnet relative to the vacuum bore in "up-down" and "left-right" direction in small steps of about 0.01 mm. The electron current at FC3 and FC4 was maximized and the vacuum tube was fixed to the bore of the superconducting magnet. After the vacuum tube alignment with respect to the magnetic field, both purification and measurement traps were placed inside the superconducting magnet.

Afterwards cesium ions were created at 90 eV energy from a surface ion source placed about 800 cm away from the magnet. The continuous ion beam was transmitted through the transfer line and the Penning trap system and detected outside the super-conducting magnet on a micro-channel plate detector (MCP3 in Fig. 5.1). The ions passing through the purification Penning trap can hit the diaphragm (see Fig. 5.2) if the ion beam is not aligned with the magnetic lines or has a current distribution larger than the diameter of the diaphragm. In that case it is possible to measure the ion current on the diaphragm by a picoameter. In Figure 6.2 (A) the ion current detected by the micro-chennel plate (MCP3) (open squares) and the current on the diaphragm (filled circles) are plotted as a function of the voltage difference applied to the "left-right" deflector. At zero voltage difference between "left-right" deflector the detected ion current is minimum at the diaphragm and maximum at the MCP3 detector. The

same result is shown in Fig. 6.2 (B) for the "up-down" deflector. At 7 V voltage difference between "up-down" deflector the detected ion current is minimum at the diaphragm and maximum at the MCP3 detector. The second measurement indicates that the magnetic field is still not perfectly aligned in "up-down" direction and a small deflection is needed to pass the ion beam trough the diaphragm.
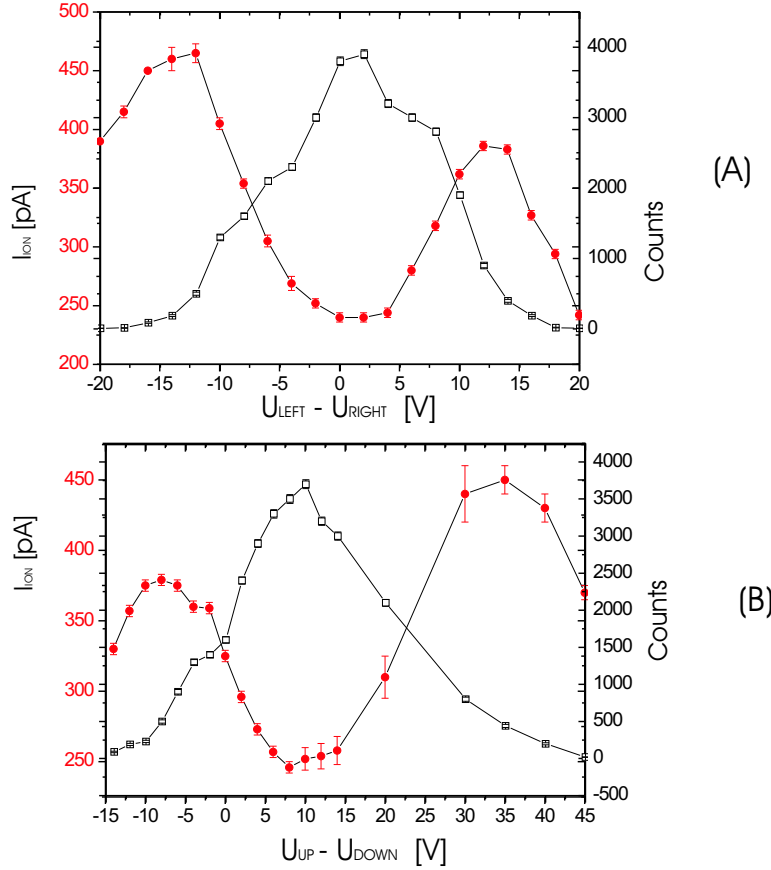
Figure 6.2: A: Ion current detected on the micro-channel plate (MCP3) (open squares) and the current measured on the diaphragm (filled circles) plotted as function of the voltage difference applied to the "left-right" deflector. B: Ion current detected on the MCP3 (open squares) and the current measured on the diaphragm (filled circles) plotted as function of voltage difference applied to the "up-down" deflector.

6.2   Commissioning the purification trap

The purification trap is dedicated for isobaric separation using the mass-selective buffer gas cooling technique. The nuclei of interest can be cooled and centered while the other ions can be removed at the same time. The theoretical background of this technique

was discussed in chapter 3 in Section 3.2.2. Below, some systematic measurements are
presented to implement this technique in the purification trap.

6.2.1   Potential shape along the z-axis
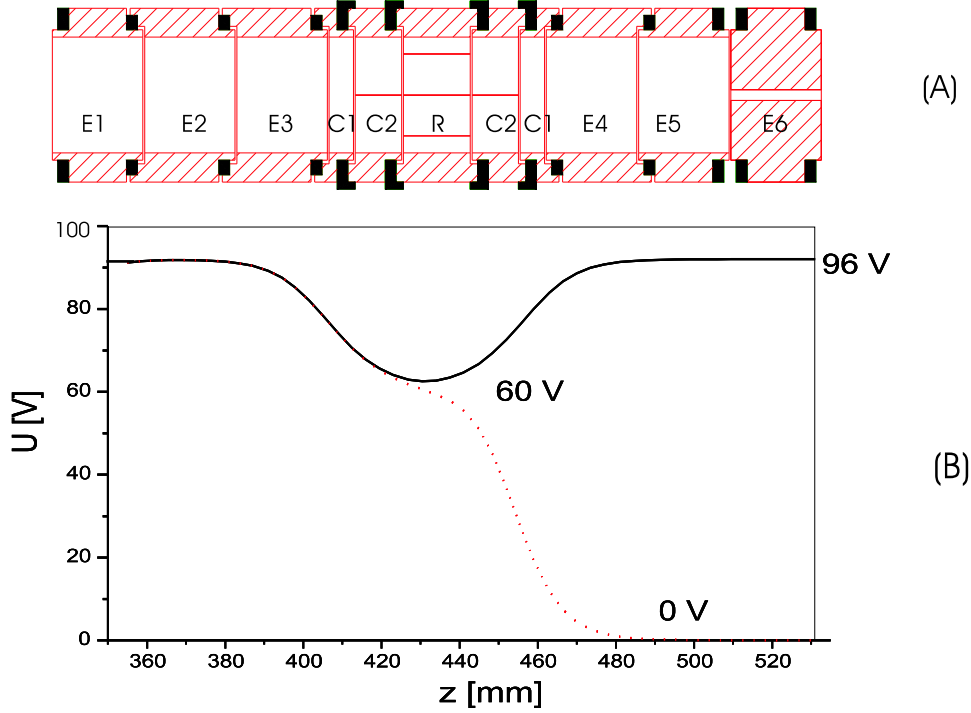
Figure 6.3: A: Cut of the electrode arrangement of the purification trap. See Tab 6.1
for nomenclature of the electrodes and the DC voltage applied to each electrode. B:
The potential shape along the z-axis of the purification trap. A harmonic potential
well is used to accumulate and cool the ions. The cooled ions are released towards
the detector by switching down the voltage at the E4, E5 and E6 end electrodes. The
potential shown was calculated using the RELAX code.

For capturing and storing ions in the purification trap, the potential height is chosen
according to the ion energy. As an example Fig. 6.3 B shows the potential shape used
for the purification trap for an incoming ion energy of 90 eV. The solid line represents
a closed trap, while the dotted line indicates the potentials slope for extracting the
ions from the trap. The trap bottom is kept at 60 V. The full volume of the potential
well (between z = 400 mm and z = 470 mm) allows to accept a large incoming ion
bunch and cool it subsequently. The center part of the trap at z = 435 mm is used
to store the cooled ions. The center region of the trap is made harmonic by applying
appropriate [Gabrielse83, Sikler03a] voltages to the correction electrodes. The voltages
of the purification trap electrodes determined for optimum injection, capturing and
ejection are given in Tab. 6.1.

Table 6.1: Voltages applied to the purification trap electrodes for optimum injection, trapping and ejection of ions. The correction voltages are chosen to minimize anharmonic components of the trapping potential.

Electrodes	Abbreviation	Applied voltage	Condition	Length of the electrode
end electrodes	E1,E2 and E3	96 V	trapping	25 mm
end electrodes	E1, E2 and E3	0 V	injection	25 mm
correction	C1(out)	83.04 V		6.7 mm
correction	C2(in)	64.68 V		12.8 mm
ring	R	60 V		18.5 mm
correction	C(in)	64.68 V		12.8 mm
correction	C(out)	83.04 V		6.7 mm
end electrodes	E4,E5 and E6	96 V	trapping	25 mm
end electrodes	E4,E5 and E6	0V	ejection	25 mm

6.2.2 Determination of the magnetron frequency and optimum excitation amplitude

In order to achieve a high resolving power for the buffer gas cooling the ions have to be prepared having a very small z-oscillation amplitude after capturing in the purification trap. This is done by collisions with helium atoms at an optimum helium pressure in the trap. This also leads to an increase of the magnetron radius which helps to remove the unwanted ions.

The magnetron motion of the trapped ions is a slow motion. The magnetron frequency can be expressed by

$$\omega_- = \frac{\omega_z^2}{2\omega_+} = \frac{qU_0}{md^2} \cdot \frac{1}{2\omega_+} \qquad (6.1)$$

where $\omega_z = \frac{qU_0}{md^2}$ is the axial frequency (see Eq. (3.5)) and ω_+ is the reduced cyclotron frequency (see Eq. (3.8)). Considering the approximation that $\omega_- \ll \omega_z \ll \omega_+$ we can rewrite the magnetron frequency as

$$\omega_- \simeq \frac{qU_0}{md^2} \cdot \frac{1}{2\omega_c} = \frac{1}{2}\frac{U_0}{d^2 \cdot B}. \qquad (6.2)$$

From the expression 6.1 it is seen that the magnetron frequency is directly proportional to the trap potential. Equation (6.2) indicates that the magnetron motion is independent of the ion mass. The calculated magnetron frequency of the trapped cesium ions is about 500 Hz for the purification trap, taking into account that the trap depth (U_0) is 28 V, the magnetic field strength is B = 7 T and the trap dimension is d = 26 mm. The exact magnetron frequency is measured by applying a dipole RF field to the segmented ring electrodes and varying it around the estimated frequency of 500 Hz.
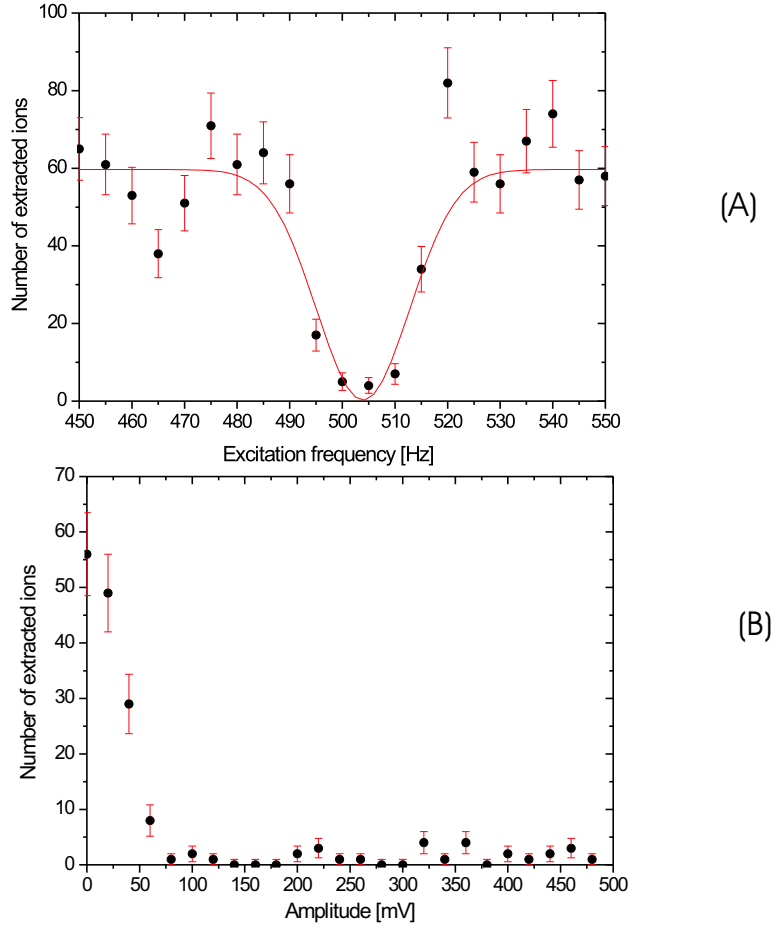
Figure 6.4: Dipole excitation in the purification trap, A: The number of extracted ions is plotted as a function of the excitation frequency. The line is a Gaussian fit to the data points giving a magnetron frequency of $\nu_- = 503(2)$ Hz. B: The number of extracted ions is plotted as a function of the excitation RF amplitude at $\nu_{RF} = \nu_- = 503$ Hz. For a RF amplitude of exceeding $A_- = 80$ mV the extracted ion counts drop almost to zero. For both measurements an excitation time of 50 ms was used and the measured helium pressure was about 4.3×10^{-7} mbar with a total trapping time of 400 ms.

When the driving field frequency is in resonance with the magnetron frequency of the trapped ions, their motional amplitude is increased such that a part of the ions cannot be extracted through the diaphragm (see Fig. 5.2), resulting in a significant reduction of the total number of detected ions. Such a measurement is shown in Fig. 6.4 A. From this measurement and a Gaussian fit to the data points a magnetron frequency of ν_- = 503(2) Hz is determined.

Subsequently the RF excitation amplitude is scanned at ν_{RF} = 503 Hz in order to determine the value which is sufficient to increase the magnetron orbit such that the ions cannot pass the diaphragm (see Fig. 5.2). Such a measurement is shown in Fig. 6.4 B. For an amplitude of 80 mV the number of extracted ions becomes zero.

From this measurement the amplitude of the ν_- excitation is chosen to be 350 mV, which gives sufficient power in order to increase the magnetron radius in such a way that all ions are driven out. A higher magnetron excitation amplitude will increase the linewidth of the cooling resonance. As a result the mass resolving power of the system will be reduced.

6.2.3 Determination of the cyclotron excitation amplitude for centering the ion cloud

Also for the quadrupole excitation of the cyclotron frequency of the trapped ions it is essential to know the proper RF amplitude of the driving field at a given pressure.

In order to determine it the amplitude is scanned and the number of extracted ions is recorded as a function of RF excitation amplitude, as shown in Fig. 6.5. The number of extracted ions is increasing as the amplitude is increasing. After 200 mV all the ions of the desired mass are centered and the extracted number of ion stays almost constant. From this measurement the RF quadrupole excitation amplitude is chosen to be 200 mV. It should be mentioned that, after applying the cyclotron excitation with an amplitude of 200 mV, nearly all the ions of interest can be centered.

6.2.4 Timing sequence of the cooling resonance

The typical cycle time of the Penning trap system for buffer gas cooling of the ions in the purification is about 400 ms. This particular time cycle is used for the excitation of cesium ions in the trap. First the trap is loaded for 100 μs from a pulsed Cs ion beam, then the ions are cooled axially for 150 ms by buffer gas collisions, afterwards magnetron excitation is applied for 50 ms, and, finally, the ions are excited for 200 ms at the true cyclotron resonance at $\omega_{RF} = \omega_c$ for buffer gas cooling. Finally the ions are extracted within a very short time (50 μs) and detected by a micro-channel plate detector. For the investigation of the influence of the buffer gas pressure on the cooling resonance, magnetron, as well as cyclotron excitation parameters and the cooling time are varied in different measurements.

For a higher helium pressure, the total cycle time can be reduced to 150 ms. However this is not the lower limit. One can reduce the total cycle time even further to access
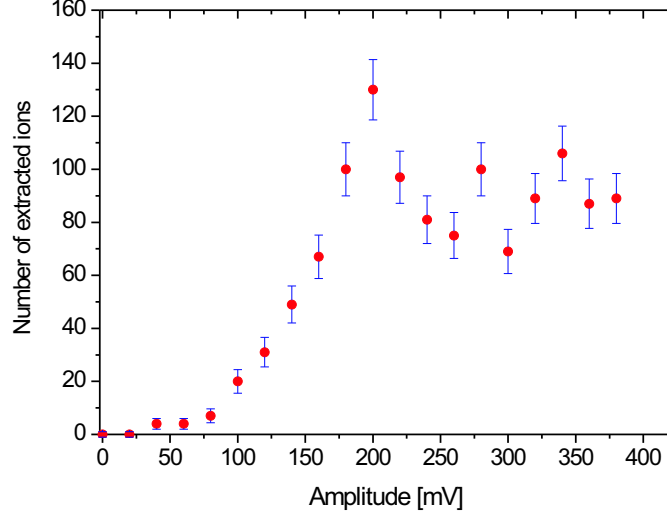
Figure 6.5: Number of extracted ions as a function of the applied RF amplitude for quadrupole excitation at ω_c. About 200 mV is required to center all the ions. The cyclotron frequency was $\nu_c = 809{,}725$ Hz (fixed) with an excitation time of 200 ms. The magnetron frequency and amplitude was $\nu_- = 503$ Hz and $A_- = 350$ mV, respectively, with an excitation time of 50 ms.

shorter-lived radioactive nuclei, but the resolving power will also be reduced. At 150 ms total cycle time, the resolving power was determined to $\frac{m}{\Delta m} = 40{,}500$.

6.2.5   Cooling resonance of stable cesium ions

As an example, Fig. 6.6 shows the number of accumulated ions as a function of the excitation frequency. After loading the trap the ions were axially cooled for 150 ms by collisions with buffer gas atoms. Then the ions were excited by a dipole field at the magnetron frequency of 503 Hz with an amplitude of 350 mV. The magnetron excitation time for this particular measurement was 50 ms. The applied quadrupole RF excitation frequency was scanned from 809,680 Hz to 809,760 Hz in steps of 4 Hz with an amplitude of 200 mV for an excitation time of 200 ms. When the driving RF frequency is in resonance with the cyclotron frequency of the trapped ions, the magnetron radius and the reduced cyclotron radius of the ions will be reduced and the ions will move towards the trap center. As a result the number of extracted ions will be maximum when the excitation frequency matches the cyclotron frequency as shown in Fig. 6.6. From a Gaussian fit to the data points a FWHM of about 10 Hz is obtained. This corresponds to a mass resolving power of about $\frac{m}{\Delta m} = 85{,}000$.
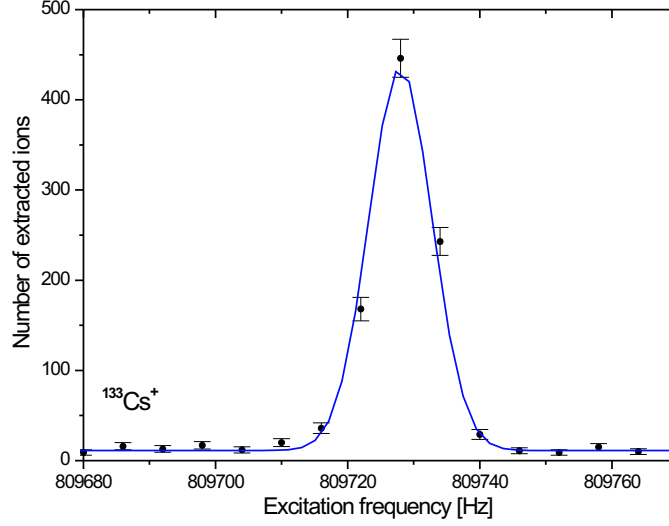
Figure 6.6: Quadrupole excitation of Cs^+ in the purification trap in the presence of helium buffer gas. The number of extracted ions is plotted as a function of the applied radiofrequency. The solid line is a Gaussian fit to the data points. The RF excitation amplitude was 200 mV and the excitation time was 200 ms with a total cycle time of about 400 ms. The width of the resonance curve corresponds to a mass resolving power of $\frac{m}{\Delta m} = 85,000$. The helium pressure was about 4.3×10^{-7} mbar measured with Gauge 1 (see Fig. 5.1).

6.2.6 Dependence of the resolving power on the helium pressure

Systematic measurements were performed to study the effect of the buffer gas pressure on the mass resolving power. The Full Width at Half Maximum (FWHM) of the cooling resonance is plotted as a function of buffer gas pressure in the trap in Fig. 6.7 A. The measurement shows that a higher helium pressure increases the FWHM of the resonance which implies a lower mass resolving power of the trap. At higher helium pressure a higher cyclotron excitation amplitude is required for centering as shown in Fig. 6.7 B. The measurements were performed for three different pressures.

In figure 6.8 the cyclotron frequency obtained from the cooling resonance is plotted as function of the helium pressure in the purification trap. The plot shows a shift of the center frequency towards higher values as the helium pressure increases in the trap. The frequency shift was about 0.8 Hz for a pressure change of about 1.2×10^{-6} mbar. This shifts could be due the higher damping. For each measurement the other conditions such as magnetron and cyclotron excitation amplitude and excitation time were kept constant.

(A)

(B)
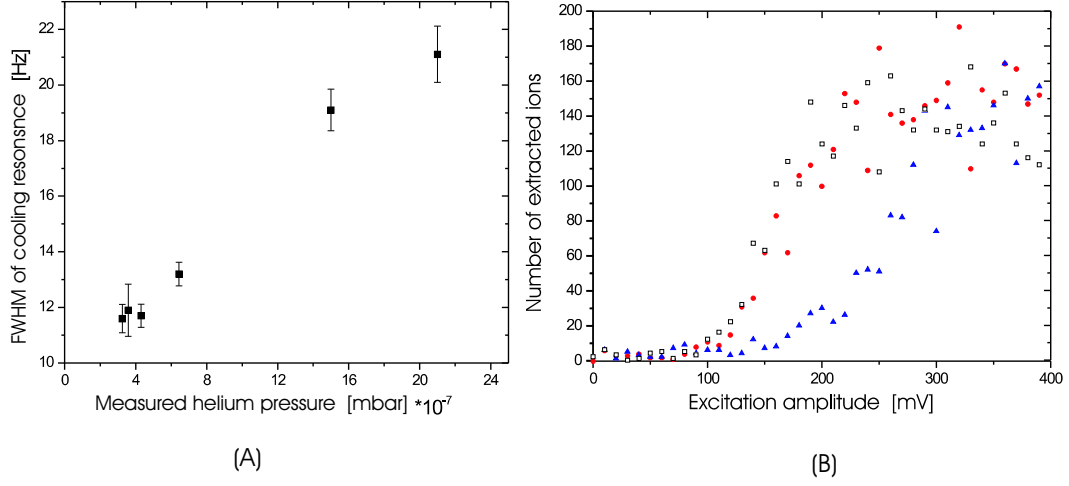
Figure 6.7: A: Full width half maximum (FWHM) linewidth of the cooling resonance as a function of the pressure measured by Gauge 1 (see Fig. 5.2). B: Number of extracted ions as a function of the cyclotron excitation amplitude for three different pressures: Open squares $p_{He} = 3.2 \times 10^{-7}$ mbar, filled circles $p_{He} = 4.3 \times 10^{-7}$ mbar, and filled triangles indicate a pressure of about 1.2×10^{-6} mbar. The excitation time was 200 ms for each case.
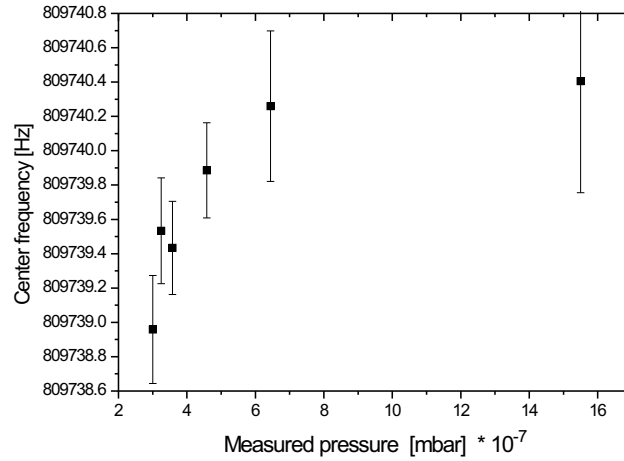
Figure 6.8: Center frequency of the cooling resonance as a function of the helium pressure in the trap. The measurements were performed with cesium ions.

6.3   Commissioning of the measurement trap

The second trap i.e. the measurement trap is dedicated to precision mass measurements via cyclotron frequency measurements. The theory of the technique is described in Chapter 3 in Section 3.2.3. Below some systematic measurements are presented which were obtained in the commissioning of the measurement trap.
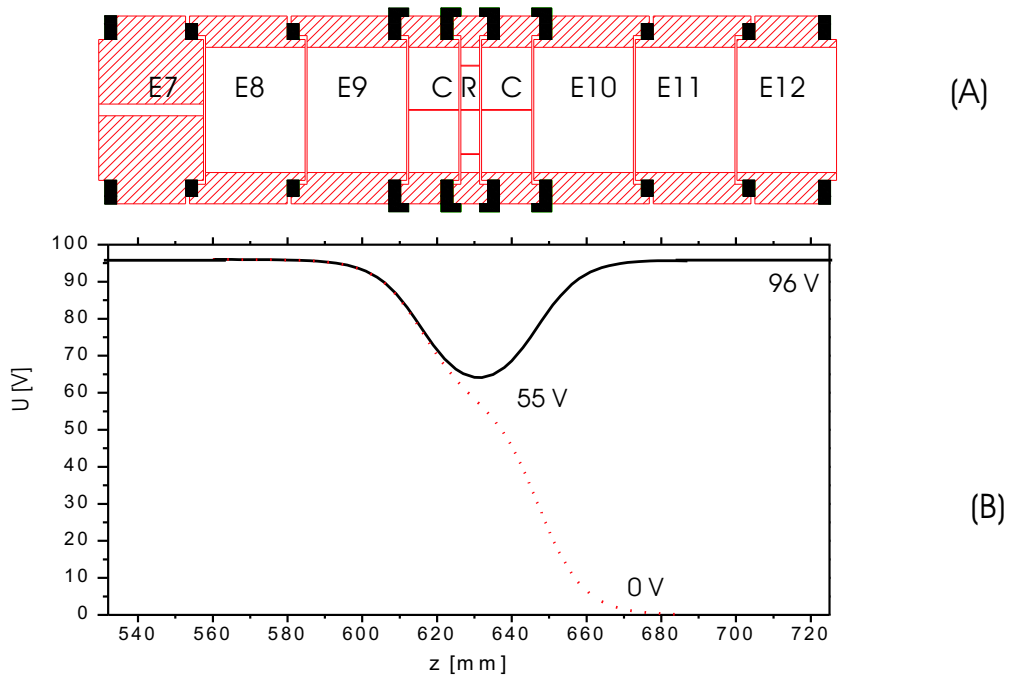
Figure 6.9: Cut of the electrode arrangement of the measurement trap. See Tab. 6.2 for nomenclature of the electrodes and the DC voltage applied to each electrode. B: The potential shape along the z-axis of the measurement trap. The harmonic potential well is used to capture the ions transferred from the purification trap. The ions are released towards the detector by switching down the voltage at the E10, E11 and E12 end electrodes. The potential shown was calculated using the RELAX code.

6.3.1 Potential shape along the z-axis of the measurement trap

The potential shape along the z-axis of the measurement trap is shown in Fig. 6.9 for 90 eV incoming ion energy. The end electrodes are kept at 96 V to close the trap. The ring voltage is kept at 55 V, 5 V lower than the purification trap, which keeps the bottom of the measurement trap at the same potential level as the purification trap (determined by RELAX calculation). An appropriate voltage needs to be applied to the correction electrode to create a harmonic potential at the trap center [Gabrielse83]. A set of voltages applied to the measurement trap electrodes for injection, trapping and ejection of the ions is given in Tab. 6.2.

Table 6.2: Voltages applied to the measurement trap electrodes for injection, trapping and ejection of the ions coming from the purification trap. The correction voltages are chosen to minimize anharmonic components of the trapping potential.

Electrode	Abbreviation	Potential applied	Condition	Length of the electrode
end electrodes	E7,E8 and E9	0 V	injection	25 mm
end electrodes	E7,E8 and E9	96 V	trapping	25 mm
correction	C	59.92 V		12.6 mm
ring	R	55 V		4.7 mm
correction	C	59.92 V		12.6 mm
end electrodes	E10,E11 and E12	96 V	trapping	25 mm
end electrodes	E10,E11 and E12	0V	ejection	25 mm
outer electrode	out1	55.4 V		155 mm
outer electrode	out2	55.4 V		155 mm
outer electrode	out3	0 V		155 mm

6.3.2 Determination of the magnetron frequency

In order to achieve a maximum change in radial energy the ions have to be prepared having a pure magnetron motion after capturing in the measurement trap. This leads to a high contrast between the on resonance and off resonance ions in the time-of-flight resonance. In the same way as described in section 6.2.2, the magnetron frequency and the excitation amplitude of the measurement trap are determined. Figure 6.10 shows a plot of excitation frequency as a function of the extracted number of ions. The solid line is a Gaussian fit to the data giving a magnetron frequency of about 1350(2) Hz, for a particular potential depth of about 40 V. The magnetron excitation amplitude was 300 mV for 20 ms excitation time.
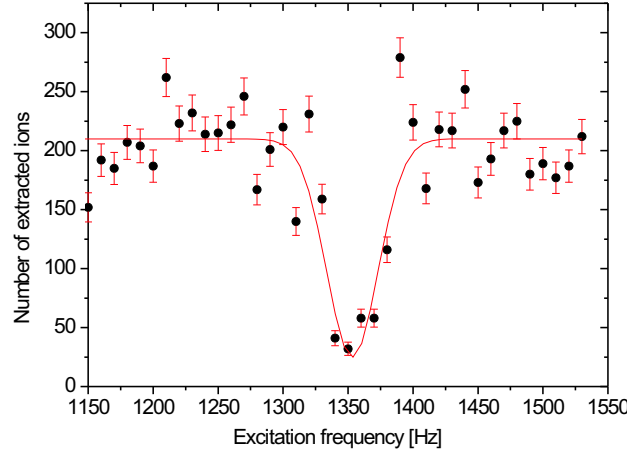
Figure 6.10: Number of extracted ions as a function of the frequency for exciting the magnetron motion. When the applied frequency is in resonance with the magnetron frequency of the trapped ions their motional amplitude is increased such that a major part of the ions cannot be extracted. The solid line represents a Gaussian fit to the data points.

6.3.3 Determination of the cyclotron amplitude

It is essential to determine the RF excitation amplitude of the quadrupolar field of the cyclotron excitation for one full conversion of the magnetron motion into cyclotron motion for a given excitation time. This periodic conversion takes place in the absence of buffer gas in the trap.

It is possible to calculate the required amplitude for one conversion. The conversion time is given by Eq. (3.40). With the values of ω_c = 809,545 Hz, ω_- = 1,350 Hz, T_{conv} = 200 ms, a = trap diameter = 32 mm, the required value of the driving field (V_d) for one conversion is about 55 mV in the case of cesium.

U_{RF} is the amplitude of the driving azimuthal quadrupole field at an ion radius r_0 (see Eq. (3.40)). If an eightfold-segmented ring electrode with an inner radius $\rho_0 = 2r_0$ is used for the creation of the azimuthal quadrupole field, then U_{RF} is to first order equal to the amplitude $2U_{RF}$ of the oscillating voltages applied to the ring segments. This is the value for an ideal quadrupole potential with an infinitely long ring electrode. So considering the correction factor the required azimuthal RF quadrupole excitation amplitude for one full conversion from magneton motion to cyclotron motion is about 110 mV for 200 ms excitation time.

To find this value experimentally the driving RF excitation amplitude was scanned as shown in Fig. 6.11. In the plot one can see periodic minima and maxima of the mean time of flight as a function the excitation amplitude. When the RF excitation amplitude is about 100 mV the mean TOF is minimum. This means the required RF
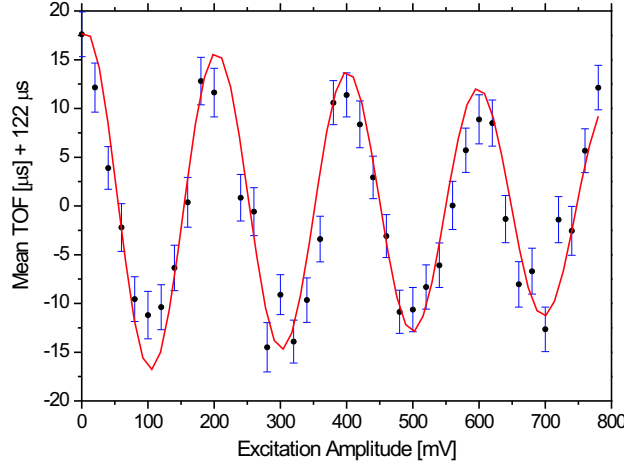
Figure 6.11: Mean time-of-flight as a function of the excitation amplitude of the quadrupole field. The excitation frequency was set to the cyclotron frequency of $\nu_c = 809{,}545$ Hz and the excitation time was 200 ms. The line represents a fit to the data points taking into account a damping over time.

excitation amplitude for one full conversion is about 100 mV for 200 ms excitation time. As the amplitude is increasing the mean TOF is increasing again and maximum at 200 mV. At this point the ions are again performing a pure magnetron motion. In this way the ion motion periodically changes as a function of the RF excitation amplitude as shown in Fig 6.11.

6.3.4   Timing sequence of the measurement

A complete measurement cycle for a cyclotron frequency measurement is shown in Fig. 6.12. It consists of loading the purification trap, buffer gas cooling in this trap, then transfer to the measurement trap, excitation in the measurement trap and finally detection at the MCP detector. The steps for the purification trap are explained in detail in Section 5.2.4. The cooled, purified and centered ions are transferred to the measurement trap. The time for each step is given in Fig. 6.12. The quadurpole excitation time can be varied for different measurements according to the desired mass resolving power.

6.3.5   Potential shape for different switching

Figure 6.13 B shows different potential shapes along the z-axis for different switching modes of the trap electrodes. Figure 6.13 A displays a transverse cut of the purification and measurement trap. In Fig. 6.13 B the solid line indicates the potential shapes along
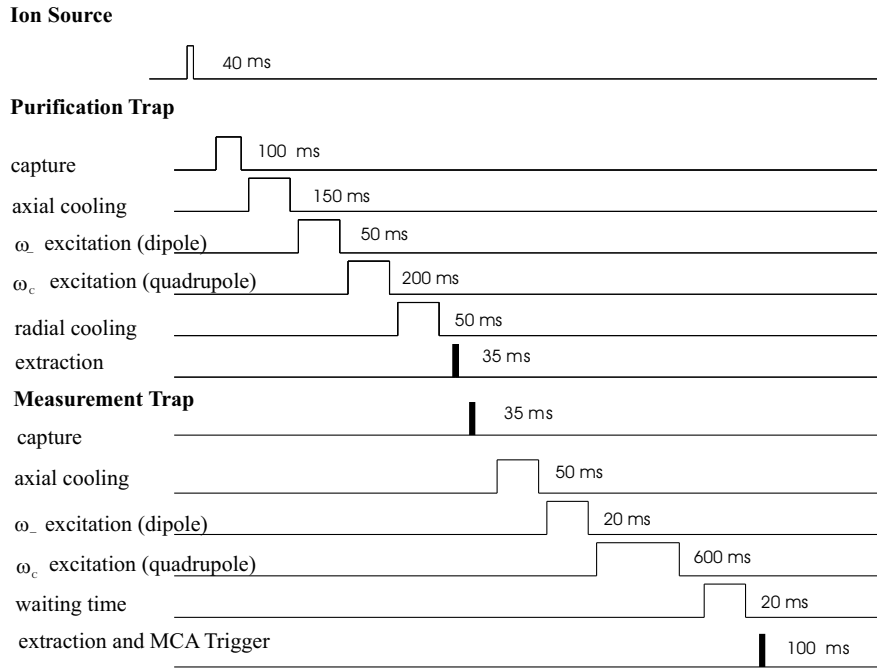
Figure 6.12: The timing sequence used at SHIPTRAP for TOF-ICR measurements. The time indicated for each step corresponds to the time used during the measurements.

the z-axis when both traps are closed. The doted line indicates the voltage applied to E1, E2 and E3 when switched down from 96 V to 50 V for 100 μs to load the purification trap. The doted-dashed line indicates the voltage on E4, E5, E6, E7, E8 and E9 when switched down from 96 V to 0 V for 35 μs (for ^{133}Cs$^+$) to eject the cooled and centered ions from the purification trap and at the same time to load the measurement trap. The dashed line indicates the voltage applied to E10, E11 and E12 when switched down from 96 V to 0 V for 100 μs to eject the ions towards the MCP3 detector.

6.3.6 Time-of-flight resonance

As an example, Fig. 6.14 shows the time of flight of cesium ions as a function of the applied quadrupole excitation frequency for the measurement timing sequence as shown in Fig. 6.12. For this measurement the amplitude of the magnetron driving field was 300 mV, the magnetron frequency was 1,350 Hz and the excitation time was 20 ms. The driving cyclotron RF field was 200 mV and the excitation time was 1.2 seconds. The linewidth of the resonance curve is 0.95 Hz. This corresponds to a mass resolving power of $\frac{m}{\Delta m} = 860,000$ and the TOF-effect was about 20%.
Theoretically the expected full width at half maximum (FWHM) of the resonance is given by Eq. (3.44) and results for $T_{RF} = 1.2$ s to a FWHM of about 1 Hz. The

Figure 6.13: A: Cut of the electrode arrangement of the double Penning trap system. The numbers on top indicate the DC voltage in Volt applied to the electrodes. B: Potential shapes along the z-axis of the trap for the different switching modes as calculated using RELAX code. Solid line indicates the potential shape along the z-axis when both traps are closed. The doted line represents for loading the purification trap. The Doted-dashed line for ejecting the ions from the purification trap and to load the measurement trap. Dashed line represents for ejecting the ions from the measurement trap.

measurement gives a FWHM of about 0.95 Hz in accordance with expectation. So the linewidth is only limited by the excitation time.
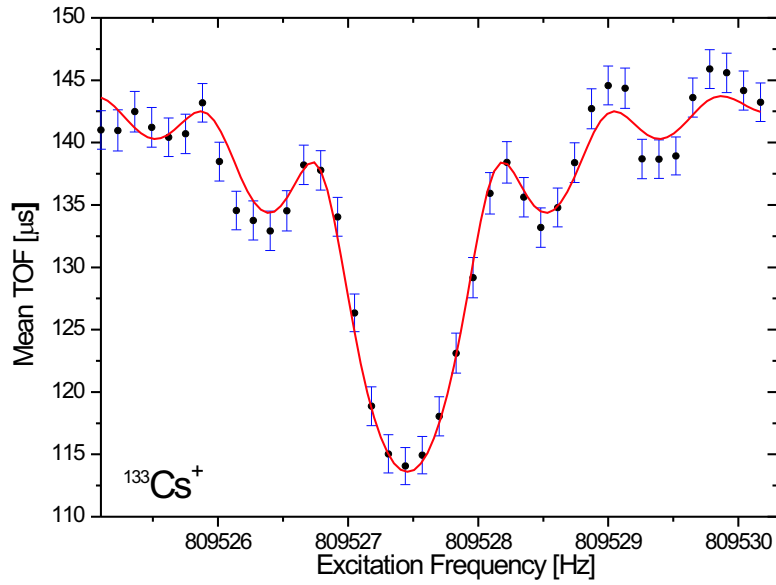
Figure 6.14: Time-of-flight resonance of Cs^+ ions in the measurement trap. The mean time of flight (TOF) is plotted as a function of the applied radiofrequency. The solid line corresponds to a fit using the theoretically expected line shape. The RF excitation amplitude was 200 mV and the excitation time was 1.2 s. The linewidth of the resonance curve $\Delta\nu_{FWHM} = 0.95$ Hz corresponds to a mass resolving power of $\frac{m}{\Delta m} = 8.6 \times 10^5$. The resolving power is only limited by the excitation time.

Chapter 7

The mass measurement procedure

In this chapter the mass measurement procedure and the identified effects are presented that contribute to the uncertainties of the measured quantities in Penning trap mass spectrometry. The ISOLTRAP spectrometer is used as example where the effects are quantified. Systematic uncertainties that come into the cyclotron frequency determination are the uncertainty due to magnetic field fluctuations and due to the mass difference between the reference ion and the ion of interest. The center frequency of the cyclotron resonance of the ion of interest shifts due to contaminating ions. These effects were studies in detail using a carbon cluster ion source [Blaum02] at ISOLTRAP and are reported in [Kellerbauer03].

Similar detailed studies will be performed using a carbon cluster ion source at SHIP-TRAP to quantify these effects. Presently, at SHIPTRAP, the statistical uncertainty dominates the systematic uncertainties discussed here. The analysis of the SHIPTRAP data is performed using the ISOLTRAP procedure and worst case estimates are applied in this case of the first on-line run of a new instruments.

7.1 Cyclotron frequency measurements

The cyclotron frequency of any ion is determined from a time-of-flight resonance as shown in Fig. 6.14. In order to find the cyclotron frequency a least squares fit of the theoretically expected function [König95] is performed.

The experimental standard deviation $\sigma(\nu)$ of the cyclotron frequency ν can be estimated as [Bollen01]

$$\frac{\sigma(\nu)}{\nu} = \frac{1}{\nu} \cdot \frac{K}{\sqrt{N} \cdot T_{RF}}, \tag{7.1}$$

where N = number of detected ions, T_{RF} = excitation time and $K = 0.898$ is an empirical constant independent of the number of ions and the excitation time. From Eq. (7.1) one can see that a longer excitation time and a higher number of ions reduce the experimental standard deviation. The excitation time might be limited by the

half-life and the number of detected ions is depending on the production yield. If the yield is not a limiting factor a measurement period of about 15 minutes is chosen to accumulate about ≤3000 ions. In the case of radioactive ions produced with low yield the measurement period can range from 30 minutes to several hours to accumulate enough statistics.

7.2 Frequency shifts due to contaminating ions

In the case of radioactive nuclei produced at ISOLDE, the presence of contaminants is possible. These can be isobaric (or isomeric) impurities created in the target and ionized in the ion source. Contaminations can also be produced in the ISOLTRAP apparatus through charge exchange reactions with buffer gas or with rest gas atoms, or by the decay of a short-lived radioactive nuclei.

The effect of contaminating ions in the precision Penning trap at ISOLTRAP was studied [König95, Bollen92a]. If all the stored ions in the trap have equal mass, the driving field will act on the center of mass of all ions and there will be no frequency shift. However, if there are other ion species than the isotope under investigation in the trap, the cyclotron frequency is shifted due to the coupling of the eigenmotions forced by the Coulomb interaction between ions with different mass-to-charge ratio [Bollen92a]. In order to correct for this frequency shift the measured time-of-flight data are classified according to the number of detected ions. There classes were defined for the plot shown in Fig. 7.1: 1-2, 3-4 and 4-5. The data of each class was used to determine cyclotron frequency. The result is plotted in Fig. 7.1 for a $^{232}Ra^+$ measurement at ISOLTRAP. The cyclotron frequency is shifted towards higher values as the number of trapped ions in the trap increases. In order to correct this, the data is fitted by a linear function and extrapolated to 0.25 (indicated by the open circle in Fig. 7.1), equivalent to one ion in the trap, for a detector efficiency of 25%. For a particular measurement of $^{232}Ra^+$ shown in Fig. 7.1, the frequency shift was 0.00626 Hz per ion in the trap. The final cyclotron frequency used for the mass measurement is the extrapolated one along with the uncertainty of the extrapolation.

7.3 Cyclotron frequency of the reference ion

The magnitude of the magnetic field in a superconducting magnet fluctuates and decays with time. Temperature, ferromagnetic material near the magnet and the pressure in the helium dewar are mainly responsible for the magnetic field changes. The decrease of the current in the superconducting coil is responsible for the steady decay of the magnetic field. The effects responsible for irregular changes are briefly discussed below.
1: The magnitude of the magnetic field changes with the temperature of the experimental hall. The vacuum tube and the trap electrodes installed in the bore of the supperconducting magnet are made of materials with low magnetic permeability such as stainless-steel and oxygen free high conductivity (OFHC) copper. However, their
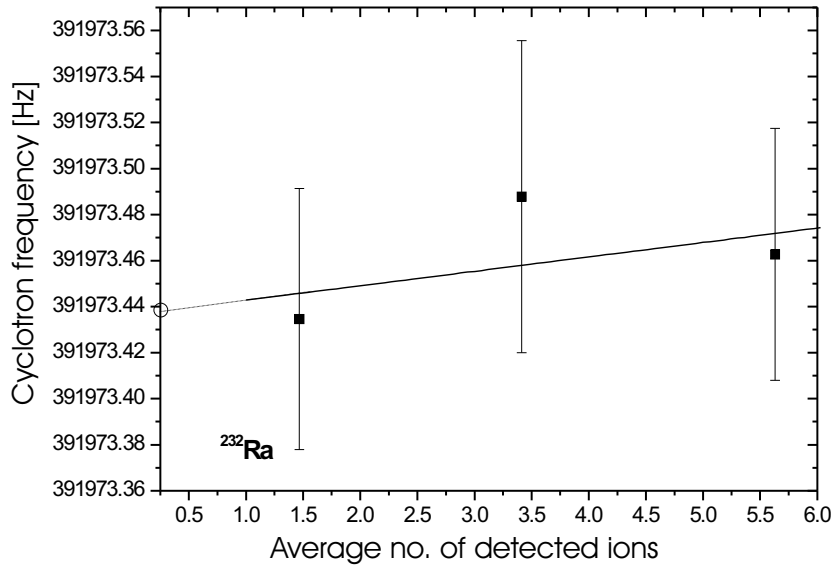
Figure 7.1: Determined cyclotron frequency of ^{232}Ra as a function of the number of detected ions on the micro-channel plate detector MCP5 per pulse. The data are fitted by a straight line the open circle indicates the extrapolation to 0.25 corresponding to one trapped ion at a detector efficiency of 25%.

magnetic permeability changes with temperature so ambient temperature fluctuations lead to magnetic field fluctuations. A temperature stabilization as installed at SMILE-TRAP allows for a reduction of the magnetic field fluctuations [Bergström02].

2: If a ferromagnetic material is brought close to the superconducting magnet it will be magnetized. This magnetization removes energy from the field of the superconducting magnet. For large ferromagnetic metallic objects (as for example a crane in the experimental hall) close to the magnet, significant magnetic field jumps of the order of 10^{-7} are observed. This effect is avoidable by keeping ferromagnetic materials far from the superconducting magnet during the measurements.

3: The boiling point of the liquid helium depends on the pressure in the helium dewar of the magnet. This changes the temperature of the liquid helium and hence the temperature of the materials in direct contact to the liquid helium in the strong magnetic-field region. Hence the magnetic field fluctuates because of the temperature dependence of the magnetic permeability of these materials. Installation of a pressure stabilization can reduce this effect.

4: The steady decay of the magnetic field is mainly due to the decrease of the current flowing in the superconducting coil. This steady decrease of the current is due to a phenomenon called flux creep [Anderson62, Anderson64]. It happens when flux lines jump from one pinning line to another, which are pinned to inhomogeneities of the superconducting materials. This steady decay of the magnetic field due to the viscous drag force follows a logarithmic decay and is of the order of $\frac{\delta B}{\delta t}\frac{1}{B}$ = -2.3×10^{-8}/h. This logarithmic decay can be approximated by a linear decay for a periods of up to one

year.

Since the magnetic field depends on time, the cyclotron frequencies of the two ions should be measured in an interval as short as possible to achieve high precision. Therefore a reference measurement is carried out just before and just after the actual measurement. The cyclotron frequency of the reference ion is then linearly interpolated to the time of the actual measurement. In that way a linear drift of the magnetic field is taken into account. The cyclotron frequency of the reference ion at a time t, the measurement time for the ion of interest, is given by

$$\nu_{ref}(t) = t\frac{\nu_1 - \nu_2}{t_2 - t_1} + \frac{t_2\nu_1 - t_1\nu_2}{t_2 - t_1},\tag{7.2}$$

and the respective uncertainty by

$$\sigma_{int}(\nu_{ref})(t) = \sqrt{\frac{1}{(t_2 - t_1)^2}[t_1^2\sigma_2^2 + t_2^2\sigma_2^2 - 2t(t_1\sigma_2^2 + t_2\sigma_1^2) + t^2(\sigma_1^2 + \sigma_2^2)]}.\tag{7.3}$$

t_1 and t_2, denote the time of the measurement of the reference ion, before and after the measurement of the ion of interest. σ_1 and σ_2 are the standard deviation of these measurements.

An additional uncertainty due to fluctuation of the magnetic field has to be considered. It was measured at ISOLTRAP using $^{85}Rb^+$ over 300 h [Kellerbauer02,Kellerbauer03] to be

$$\frac{\sigma_{mag}(\nu_{ref})}{\nu_{ref}} = 6.35(35) \cdot 10^{-11}/min \cdot \Delta t.\tag{7.4}$$

The combined uncertainty of the reference frequency ν_{ref} is then calculated according to

$$\frac{\sigma(\nu_{ref})}{\nu_{ref}} = \sqrt{\left[\frac{\sigma_{int}(\nu_{ref})}{\nu_{ref}}\right]^2 + \left[\frac{\sigma_{mag}(\nu_{ref})}{\nu_{ref}}\right]^2}.\tag{7.5}$$

7.4 Frequency ratio of the reference ion to the ion of interest

The cyclotron frequency ratio r between the reference ion ν_{ref} to the ion of interest ν_c is then given by

$$r = \frac{\nu_{ref}}{\nu_c},\tag{7.6}$$

and the respective uncertainty is

$$\frac{\sigma(r)}{r} = \sqrt{\left[\frac{\sigma(\nu_c)}{\nu_c}\right]^2 + \left[\frac{\sigma(\nu_{ref})}{\nu_{ref}}\right]^2}.\tag{7.7}$$

Here $\sigma(\nu_i)$ represents the error in the determination of the center frequency. If more than one measurement is performed the weighted mean value of the frequency ratio $(\overline{r})$ is given by

$$\overline{r} = \frac{\sum_i \frac{r_i}{\sigma_i^2(r_i)}}{\sum_i \frac{1}{\sigma_i^2(r_i)}} \qquad (7.8)$$

with a standard uncertainty given by

$$\sigma(\overline{r}) = \frac{1}{\sqrt{\sum_i \frac{1}{\sigma_i^2(r_i)}}}. \qquad (7.9)$$

The frequency ratio between the reference ion to the ion of interest can be converted to the atomic mass m_{atomic} of the ion of interest according to

$$m_{atomic} = \overline{r} \cdot (m_{ref} - m_e) + m_e, \qquad (7.10)$$

where m_{ref} is the mass of reference ion and m_e is the mass of electron. It should be mentioned that the uncertainty of the atomic mass of the reference ion contributes also to the uncertainty of the mass determination of the ion of interest.

7.5 Mass dependent systematic error

A mass dependent frequency ratio shift has been observed at ISOLTRAP due to the mass difference (more than 20 amu) between the reference ion and the ion of interest. A detailed study has been presented in [Kellerbauer03]. The magnitude of the effect was determined to be

$$\frac{\sigma_{mass}(r)}{r} = -1.6(4) \cdot 10^{-10}/u \cdot (m - m_{ref}), \qquad (7.11)$$

by cross-reference measurements using carbon clusters. A mass dependent frequency ratio shift can be due to imperfections of the electric quadrupole field or a misalignment of the precision trap's electrostatic field axis to the magnetic field axis [Brown86, Bollen96].

The last uncertainty to be considered is the residual systematic uncertainty. The cross reference measurements with the carbon cluster ions deviate from the expected values slightly even after including the mass-dependent uncertainty given by Eq. (7.11). The necessary additional uncertainty in order to obtain an agreement is given by [Kellerbauer03]

$$\frac{\sigma_{res}(r)}{r} = 8 \times 10^{-9}. \qquad (7.12)$$

The total uncertainty of the cyclotron frequency ratio is given by

$$\frac{\sigma(\overline{r})_{total}}{\overline{r}} = \sqrt{\left[\frac{\sigma(\overline{r})}{\overline{r}}\right]^2 + \left[\frac{\sigma_{mass}(\overline{r})}{\overline{r}}\right]^2 + \left[\frac{\sigma_{res}(\overline{r})}{\overline{r}}\right]^2}.$$

(7.13)

The first term in the above equation is calculated according to Eq. (7.7). The second and third term are given in Eq. (7.11) and (7.12), respectively.

Chapter 8

The first on-line mass measurements at SHIPTRAP

In this chapter the first on-line mass measurements of radioactive ions at SHIPTRAP are described performed in a beam time in July 2004. It marks an important step in the process of commissioning since for the first time all components of the set-up were used under beam time conditions. Two major problems occurred in this run which almost prevented us from measuring: A surprisingly high background of impurity ions, mainly created in the stopping cell, was observed and later it was found that the micro-channel plate detector was not working properly and had only an efficiency of 2%. Nonetheless, first mass measurements were possible. In addition, the isobaric separation of the radioactive nuclides ^{147}Ho and ^{147}Er using a buffer gas cooling scheme was demonstrated in the purification trap. This run showed that the system is ready for on-line mass measurements, but even more important, key issues were identified to be addressed in order to improve the conditions for a next run.

8.1 Production of the radionuclides at SHIP

The nuclides of interest were produced in the fusion reaction

$$^{58}\text{Ni} + {}^{92}\text{Mo} \longrightarrow {}^{150}\text{Yb}^* + xp + yn, \tag{8.1}$$
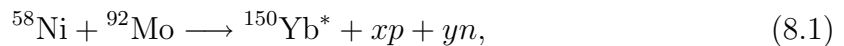
at SHIP. The production cross sections for this reaction as a function of the primary beam energy were calculated using the HIVAP code [Reisdorf81]. This code allows for an estimate of the absolute value of the cross section and a reliable prediction of the energy dependence of the cross section. The results of such a calculation are shown in Fig. 8.1.

The highest cross section of about 100 mbarn is obtained in the 3p evaporation channel for a primary beam energy of 4.36 MeV/u for the production of ^{147}Ho. Four other nuclides are produced in different evaporation channels with peak cross sections of several ten mbarn. The maximum for each channel occurs at a different energy but
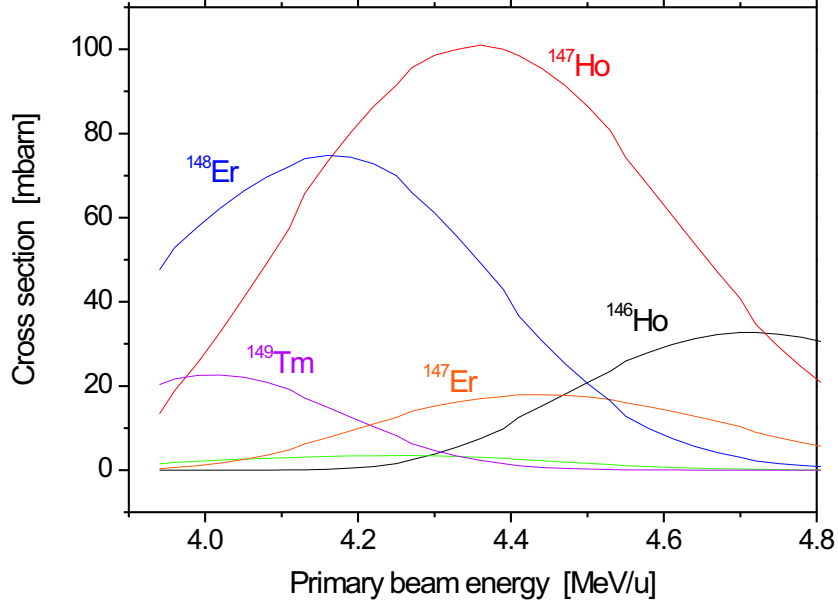
Figure 8.1: Calculated production cross-section of the different products in the re-
action ^{92}Mo(^{58}Ni,xnxp) as a function of the primary beam energy using the HIVAP
code. The highest cross-section is observed for ^{147}Ho.

all excitation functions are several MeV broad. So even if the optimum beam energy
for the 3p channel is selected, other nuclides are produced with about 20 to 50% of
the maximal possible production rate. The three relevant evaporation channels at the
selected primary beam energy of 4.36 MeV/u are

$$^{58}\text{Ni} + {}^{92}\text{Mo} \longrightarrow {}^{147}\text{Ho} + 3p, \tag{8.2}$$

$$^{58}\text{Ni} + {}^{92}\text{Mo} \longrightarrow {}^{147}\text{Er} + 2pn, \tag{8.3}$$

$$^{58}\text{Ni} + {}^{92}\text{Mo} \longrightarrow {}^{148}\text{Er} + pn. \tag{8.4}$$
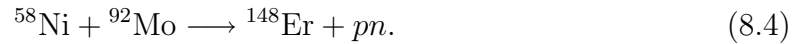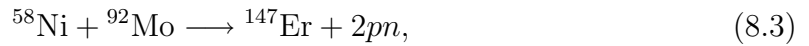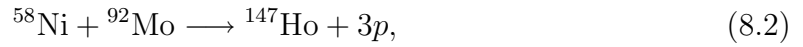
A primary beam intensity for ^{58}Ni^{14+} of up to 500 pnA was delivered by the UNILAC
accelerator. The target was a standard rotating target wheel consisting of eight single
targets. In this case rolled metallic targets made from enriched ^{92}Mo were used. The
average target thickness was 670 μg/cm^2. For an intensity of 8.9×10^{11} particles per
second about 4,000 secondary particles per second were produced. This number is
calculated from the number of detected particles at a silicon detector behind SHIP in
front of the gas cell and includes all evaporation residues produced.

The silicon detector was placed about 17 cm in front of the gas cell window on a movable feed-through and consisted of 16 stripes covering an area of 40 mm x 80 mm. The typical beam spot size was about 30 mm x 50 mm so the full beam was accepted by the detector. Normally all stripes are read out individually for a maximum spatial resolution. In this run two neighboring stripes of the detector were connected and read out together. The detector signals were amplified and digitized via an ADC and recorded on tape using the SHIP data acquisition system. In the beginning of the run the beam was centered and focussed on this detector by adjusting the field strength of the last dipole magnet and of the quadrupole triplets of SHIP.
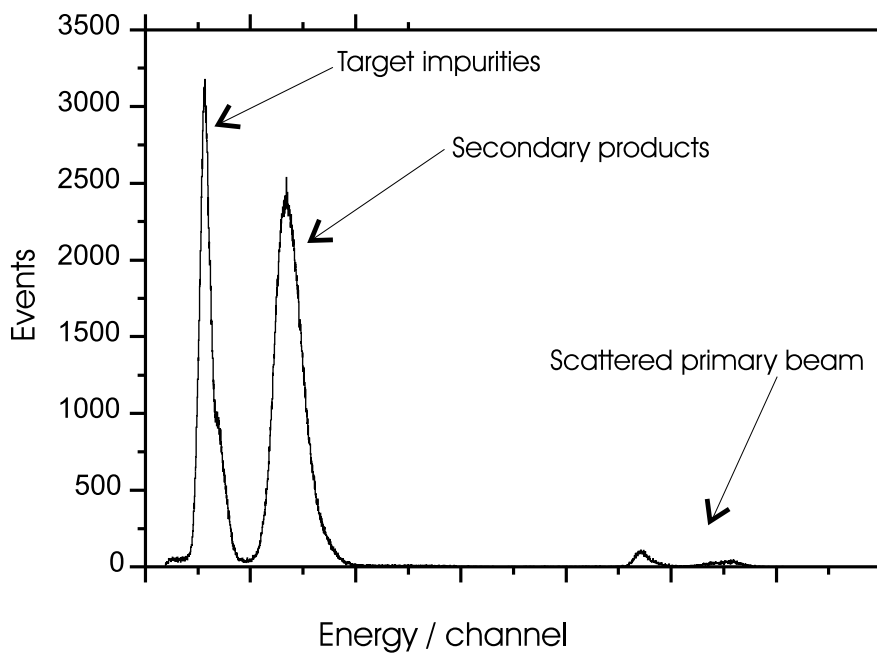
Figure 8.2: Energy spectrum of the ions detected on a silicon strip detector about 17 cm in front of the gas cell. To record the spectrum the primary beam intensity was lowered to about 100 pnA.

A typical energy spectrum obtained from this detector is shown in Fig. 8.2. It should be noted that the beam intensity was reduced to about 100 pnA whenever the silicon detector was used. The primary beam intensity was monitored by the current detected on the beam stop which was initially calibrated by the current measured on a Faraday cup in front of the target wheel. In the spectrum two prominent peaks at low energy and two smaller peaks at high energy were observed. The first peak contains background from target impurities. The second peak at 97 MeV contains the ions of interest. This was confirmed by a spectrum recorded in the beam pause where for instance α lines from the decay of the α emitters ^{151}Ho and ^{152}Er were detected. The small peaks at high energy result from scattered primary beam particles. The energy of those particles is too high compared to the evaporation residues so they were not stopped in the gas

cell but contributed to the ionization of impurities inside the cell.

The number of particles per second detected in the second peak was recorded for a primary beam current of about 100 pnA. The production rate of 4000 ions/s was obtained by linearly scaling the number of particles detected at 100 pnA to the expected number at the actual beam current during a mass measurement.

Since the SHIP separator used as a velocity filter does not provide any mass resolving power, a cocktail beam of different products was delivered. For the selected primary beam energy of 4.36 MeV/u the reaction products have an energy of 95 MeV/u $\pm$ 10% after SHIP taking into account the energy loss in the target and an additional carbon foil used as charge state reset foil. After the SHIP optimization was completed the stopping conditions were optimized.

8.2 Stopping in the gas cell

The stopping conditions in the buffer gas cell depend on the energy spread of the incident ion beam resulting in a range straggling. The typical energy spread of a SHIP beam is about $\pm$10%. Additional contributions to the range straggling are from the energy loss in the cell entrance window and optional degraders that may be used to adapt the energy of the products for optimum stopping. The main issues in choosing an appropriate entrance window for the expected energy of the reaction products are the energy loss in the foil, and the transmission through the foil, its mechanical stability, and the influence on the purity inside the cell. Since the gas purity is crucial UHV compatible and bakeable materials have to be chosen also for the window. For a minimum energy loss and hence a low straggling low-Z materials are preferable. So far only titanium and nickel foils were used. For the large required diameter of 60 mm the thinnest foil available is a 4μm titanium foil. In the holmium run a thicker foil was used to reduce the energy of the products to less than 20 MeV, because for a higher pressure than 50 mbar inside the cell a sufficient amplitude of the funnel radio frequency could not be reached due to technical limitations. So a 7.1 μm titanium foil was used, that according to TRIM calculations reduced the transmission through the window to only 15 %.

Since the injection at SHIPTRAP is almost perpendicular to the extraction direction the stopped distribution needs to be placed on the extraction axis. However, TRIM simulations show that the stopped distribution is broad compared to the size of the extraction volume. Therefore, a small mismatch can be tolerated since it does not result in a reduced number of extracted ions.

At the beginning of the run the stopping conditions in the gas cell were optimized. For that purpose a silicon detector (PIN diode) was installed inside the cell opposite to the entrance window. The energy spectrum of the particles entering the cell is taken for different pressures with this detector. The observed distribution of reaction products shifts towards lower energy for increasing buffer gas pressure. Since typical silicon detectors have a conducting surface layer, particles are only detected if their energy is

sufficient to penetrate this layer. In addition, the energy distribution was measured for different product energies using different mylar degrader foils situated on a ladder in front of the gas cell window. After the energy was close to the minimum energy detectable the stopping conditions were further optimized by maximizing the number of extracted ions detected on a multi-channel plate detector behind the buncher. This is mainly done by varying the pressure and the extraction RF and DC fields.

8.3 Identification of the ions extracted from the stopping cell

The ions extracted from the stopping cell were injected into the buncher where they were cooled and extracted as short bunches. The operating parameters for the buncher were chosen according to optimizations in off-line tests discussed in [Rodríguez02]. Additionally, the intensity of the ejected bunches detected on a micro-channel plate detector (MCP2) was optimized by varying the RF voltage i.e. the q parameter. The MCP2 detector is situated about 110 cm behind the buncher. The distance to this detector is too short to resolve different masses unambiguously from their time of flight. Therefore, the bunches were transferred to the purification trap. To get an overview of the masses extracted from the stopping cell the ions were trapped and axially cooled for about 500 ms and ejected towards the multi-channel plate detector behind the magnet (MCP3) and their time of flight was recorded.

The mass of the ions was determined from their time of flight using the time of flight of ^{133}Cs ions from the reference ion source for calibration via the relation

$$\frac{T_1}{T_2} = \sqrt{\frac{m_1}{m_2}}, \tag{8.5}$$

where T_1 and T_2 denote the time-of-flight of mass m_1 and m_2 respectively. Even though the ions are passing through a strong magnetic field the relation is expected to hold in a first order approximation. This procedure is faster than applying the buffer gas cooling technique and scanning the excitation frequency if a larger mass range has to be covered. A typical mass spectrum is shown in Fig. 8.3. A surprisingly high number of impurity ions over a wide mass range was observed. Since the purity inside the cell is crucial the gas cell was baked at a temperature of about 150 °C for more than 24 hours before the run. The buffer gas was supplied from a He 7.0 bottle and fed into the cell via a commercial gas purifier (SAES getter) which should reduce eventual impurities to the ppm level. The mass range corresponding to each peak and possible species assigned to it are listed in Tab. 8.1.

The most prominent peak (no. 10) corresponds to a mass of $A = 129 \pm 3$. It contains several Xe isotopes which was additionally proved by a cyclotron resonance of the naturally most abundant Xe isotopes in the purification trap. The ions of interest were contained in peak 11 which corresponds to A = 147 with an uncertainty of 2 mass units along with impurities like $(Xe + H_2O)^+$. The other ions present include
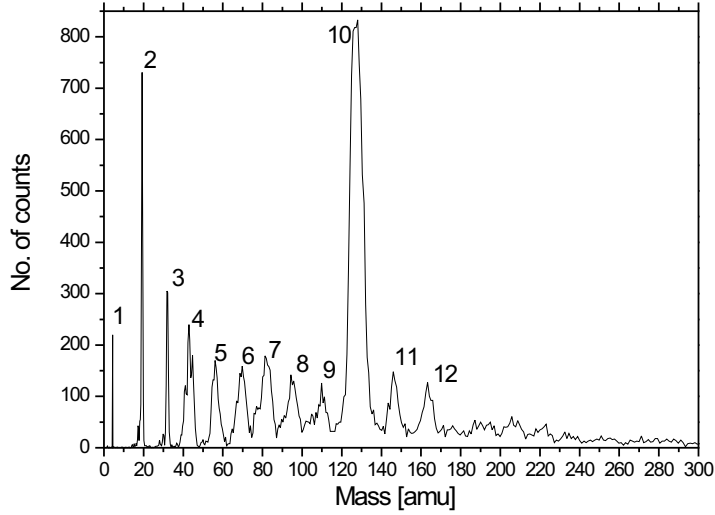
Figure 8.3: Mass spectrum of the ions extracted from the purification trap as determined in the beamtime in July 2004. A large number of impurity ions was observed initially. The peak 11 corresponds to mass A=147 with an uncertainty of two mass numbers. It contains the ions of interest ^{147}Ho, ^{147}Er and ^{148}Er as well as impurity ions like $Xe - H_2O$ clusters. Table 8.1 lists the ion species which were assigned to the other peaks.

helium, water clusters and hydrocarbons. Most of the assigned contaminations listed in the table have already been observed in a previous gas cell test run performed at the Tandem accelerator at Garching [Eliseev04]. The ratio of impurities to the ions of interest was at least 250. Such a high number of impurities is difficult to handle in the purification trap since space charge effects spoil the resolving power. For instance at ISOLTRAP [Blaum04] it was found experimentally that the ratio between impurities and ions of interest must not exceed 200 otherwise the mass resolving power is reduced. In order to allow for a mass measurement in the measurement trap the source of the impurities had to be identified and the amount of impurities had to be reduced substantially.

Comparing the peaks in the mass spectrum (Fig. 8.3) it is striking that the low mass peaks up to A = 30 are much narrower than the other peaks. It should be mentioned that low masses such as He were anyway not expected to be transported by the RF funnel because of its mass selectivity. Hence it was supposed that these ions were created in the purification trap. Even though the buffer gas for the trap is also supplied via a gas purifier, contamination by water vapor was sometimes observed in off-line tests since the system is usually not baked. The ionization can happen via charge exchange or by free electrons trapped in the strong magnetic field (Penning effect). For comparison a mass spectrum was recorded with the incident ion beam blocked. It

Table 8.1: Ion species tentatively assigned to the mass spectrum shown in fig. 8.3. They were identified by measuring their time of flight from the purification trap to the MCP3 detector. The uncertainty of the mass determination was about two mass units. $^{129,132}Xe^+$, $^{147}Er^+$ and $^{147}Ho^+$ were identified by measuring their cyclotron frequencies in the purification trap.

peak	A(δA)	possible species
1	4	He^+
2	19(1)	H_2O^+ or H_3O^+
3	31(2)	O_2^+
4	44(2)	CO_2^+, $C_2H_3O^+$
5	55(2)	$(H_2O)_3^+$
6	68(2)	$(H_2O)_4^+$
7	84(2)	$^{84}Kr^+$
8	95(2)	???
9	110(2)	$(H_2O)_6^+$
10	129(3)	$^{129-132}Xe^+$
11	147(2)	$^{147}Ho^+$, $^{147}Er^+$, $(H_2O)_8^+$
12	164(2)	$^{147}Ho(H_2O)^+$, $^{147}Er(H_2O)^+$

was found that the helium and water ions were indeed created in the purification trap.

The heavier impurity ions were created in the stopping cell by ionization due to the ion beam and by charge exchange processes. Such impurities could originate from materials outgassing or they may be introduced via the gas feeding line. In the latter case the amount of impurities could be reduced by using a liquid nitrogen trap situated in the gas feeding line close to the stopping cell. Therefore, after activating the cold N_2 trap another mass spectrum was recorded shown in Fig. 8.4. The spectrum was accumulated over the same time interval as the one shown in Fig. 8.3 so the peak heights can be directly compared. A significant reduction of most peaks was observed but the helium peak stays constant and the water peak is only slightly reduced supporting that these ions were created in the Penning trap itself. For sure, water and water clusters contribute significantly to the impurities as also indicated by the sharp structure at A = 72 corresponding to $(H_2O)_4^+$. In the mass range A = 70 to A = 100 some impurities increase which may be due to statistical fluctuations or because some of them were extracted as molecules before but appear as singly-charged ions now. The intensity of peak 11 around mass 147 decreased as well with the cold N_2 trap in operation. This indicates that peak 11 also contained contaminations e.g. $(H_2O)_8^+$ since the primary beam intensity and hence the production rate of erbium and holmium was constant during both measurements. The ratio of impurities to the ions of interest dropped to about 100 with the cold N_2 trap in operation.
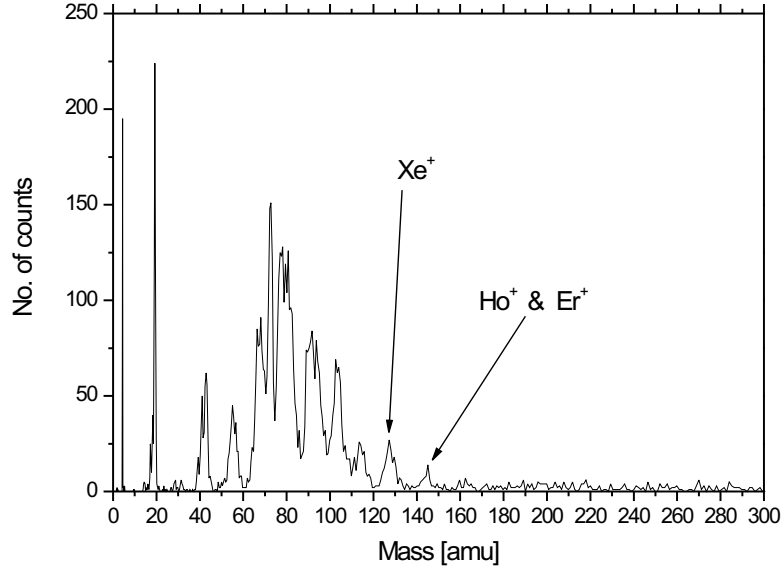
Figure 8.4: Mass spectrum of ions extracted from the purification trap. Compared to Fig. 8.3 a cold N_2 trap was used in the gas feeding line of the gas cell.

8.4   Isobaric separation and mass measurements in the purification trap

Under the improved conditions the buffer gas cooling in the purification trap was applied to center ions with A = 147 even though the number of impurities was still unfavorable. A mass spectrum of ions ejected from the purification trap recorded during a scan of the cyclotron excitation frequency for centering is shown in Fig. 8.5. In this time-of-flight mass spectrum, besides the strong contamination peaks of helium and water, a rather clean spectrum is observed with a peak at mass 147(2). The helium and water ions were created during the complete cycle in the Penning trap i.e. also after the magnetron excitation driving unwanted ions out of the trap center.

The cooling resonance obtained from the scan of the cyclotron excitation frequency is shown in Fig. 8.6 The plot shows the number of ejected ions detected on MCP3 in a TOF time window that contains only ions with A = 147 ± 10 (see mass range indicated in Fig. 8.5) as function of the cyclotron excitation frequency. Two separate peaks for ^{147}Er$^+$ and ^{147}Ho$^+$ at their resonance frequencies 732,351.8 and 732,401.3 Hz were observed. The mass difference between the two isobars ^{147}Er$^+$ and ^{147}Ho$^+$ corresponds to a frequency difference of 49.5 Hz. Taking the halfwidth of an individual peak of $\Delta\nu_{FWHM} = 12.4$ Hz the resolving power was about 60,000. The center frequencies were obtained by fitting two Gaussians to the data points keeping the baseline fixed at zero counts. In the case of the holmium peak two data points in the maximum
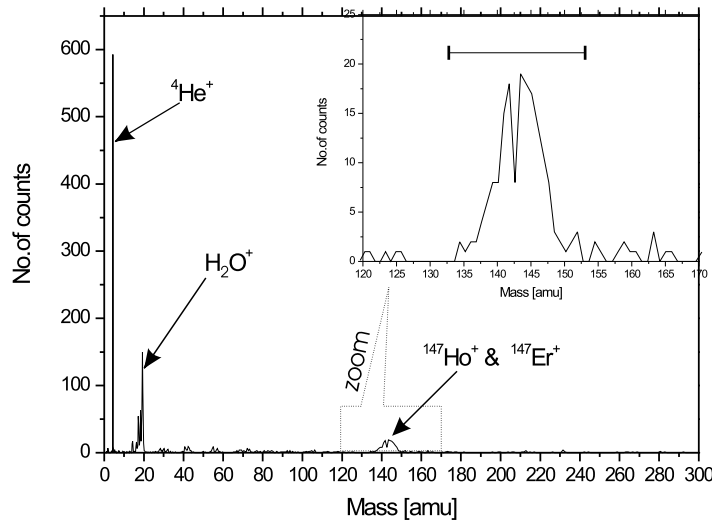
Figure 8.5: Time-of-flight mass spectrum of ions ejected from the purification trap after buffer gas cooling recorded on MCP3. The purification trap was operated to center selectively only ^{147}Er and ^{147}Ho (scan over both resonances). The mass region around 147 is zoomed and shown as insert. Here also mass range is indicated used to obtain the cooling resonance shown in Fig. 8.6.

deviate from the fit curve by about 2 σ. This deviation is still in agreement with statistical fluctuations according to a $\chi^2 = 1.8$ obtained for the displayed fit. The ratio between the number of ^{147}Ho$^+$ ions to the number of ^{147}Er$^+$ ions is about three. From the calculated production cross sections the ratio should be five. The reason for this deviation is not yet understood.

8.5 Mass measurements in the purification trap by use of the cooling resonance

In general the buffer gas cooling technique is used to prepare cooled and isobarically purified ion samples for a precise mass measurement. However, since the cyclotron frequency of the centered ion can be determined from a cooling resonance as shown in Fig. 8.6 as well, it can also be used for a mass measurement. This is rarely done because the conditions are not as clean as in the measurement trap and the resolution is lower. The resolution is generally limited by the damping due to the buffer gas. Further difficulties may arise from the fact that unwanted ions are still present in the trap only at a larger magnetron radius. The Coulomb interaction between the different species may also contribute to frequency shifts.

To perform a mass measurement in the cooler trap the magnetic field has to be calibrated by a cyclotron frequency measurement of a reference ion with well known mass. As discussed in chapter 7.3 for the case of ISOLTRAP the magnetic field changes with
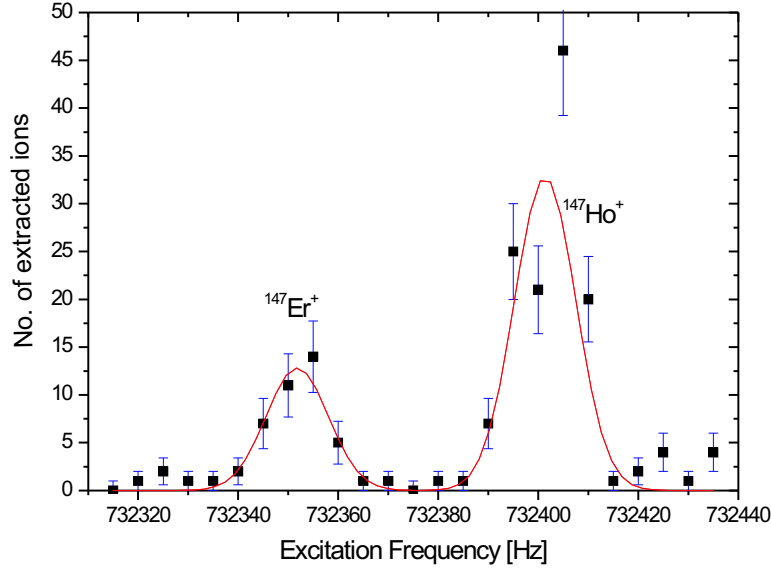
Figure 8.6: Number of ejected ions from the purification trap as a function of the cyclotron excitation frequency. A mass resolving power of about 60,000 was reached. The magnetron excitation amplitude $A_- = 900$ mV and the cyclotron excitation amplitude $A_c = 400$ mV were kept constant during the measurements. The cyclotron excitation time was 200 ms. The buffer gas pressure was $p_{He} = 4.3 \times 10^{-7}$ mbar

time. For that reason it is calibrated by a cyclotron frequency measurement of the reference ion before and after the actual measurement. Hence a cooling resonance for ^{133}Cs ions from the reference ion source was recorded keeping all relevant parameters constant such as buffer gas pressure, excitation times and amplitudes for the magnetron and cyclotron frequency excitation. Such a cooling resonance recorded during the beamtime in July 2004 is shown in Fig. 8.7. The resonance frequency for ^{133}Cs$^+$ was determined to be 809,742.75(20) Hz from a Gaussian fitted to the data points. The linewidth is $\Delta\nu$ (FWHM) ≈ 12.6 Hz corresponding to a mass resolving power of about 64,000. The data points are not very well described by the fitted lineshape. Since the width of the curve is higher than expected for that buffer gas pressure of $p_{He}=4.3\times10^{-7}$ *mbar* it may due a wrongly chosen parameter. It may also be due to the high number of ions during the measurement because of the low detection efficiency of the micro-channel plate detector MCP3. It can happen that the line splits into two lines where the center of gravity stays constant. Since the measurements were sequentially performed the magnetic field has to be interpolated to the time of the measurement for the ion of interest. This is done in the same way as for the measurement trap according to Eq. (7.2).

The results of the mass measurement of ^{147}Er and ^{147}Ho in the purification trap are summarized in Tab. 8.2. The uncertainties take into account the error of the center frequency determination from the fit and the error due to the magnetic field interpolation.
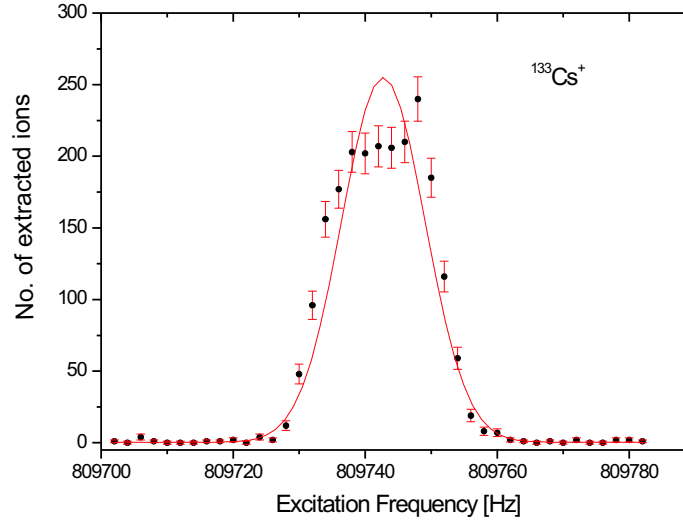
Figure 8.7: Cooling resonance of ^{133}Cs$^+$ from the reference ion source. The linewidth of the resonance is about 12.5 Hz, corresponding to a mass resolving power of about 64,000. The measurement was performed at the same conditions that were also used for holmium and erbium.

Table 8.2: Results of the analysis for ^{147}Er and ^{147}Ho measured by use of the SHIP-TRAP purification trap. $\overline{r}$ is the mean frequency ratio between the ion of interest and ^{133}Cs$^+$ calculated according to Eq. (7.10). N_{total} is the total number of detected ions. m_{atomic} is the atomic mass calculated according to Eq. (7.15). $\delta m_{atomic}/m_{atomic}$ represents the relative mass accuracy.

Nuclei	$T_{1/2}$	Frequency ratio($\overline{r}$)	N_{total}	m_{atomic} [u]	$\delta m_{atomic}/m_{atomic}$
^{147}Er	1.5 s	1.105 674 5(10)	66	146.950 11(18)	1.4×10^{-6}
^{147}Ho	5.8 s	1.105 599 7(10)	198	146.940 17(13)	0.88×10^{-6}

8.6 Mass measurements in the measurement trap by the TOF-ICR technique

For the two nuclides with the highest production rate at the selected primary beam energy, namely ^{147}Ho and ^{148}Er, mass measurements using the TOF-ICR technique in the measurement trap were performed. Due to the problems discussed above and the low count rate of about 0.5 ions/s detected at MCP 3 only a short excitation time was used limiting the precision.

The obtained time-of-flight cyclotron resonances for ^{147}Ho and ^{148}Er are shown in Fig. 8.8. For a cyclotron excitation time of 200 ms a linewidth of 5 Hz was observed in agreement with the theoretical limit for the chosen cyclotron excitation time. About 2,000 ions were accumulated for each resonance. The TOF effect for both resonances
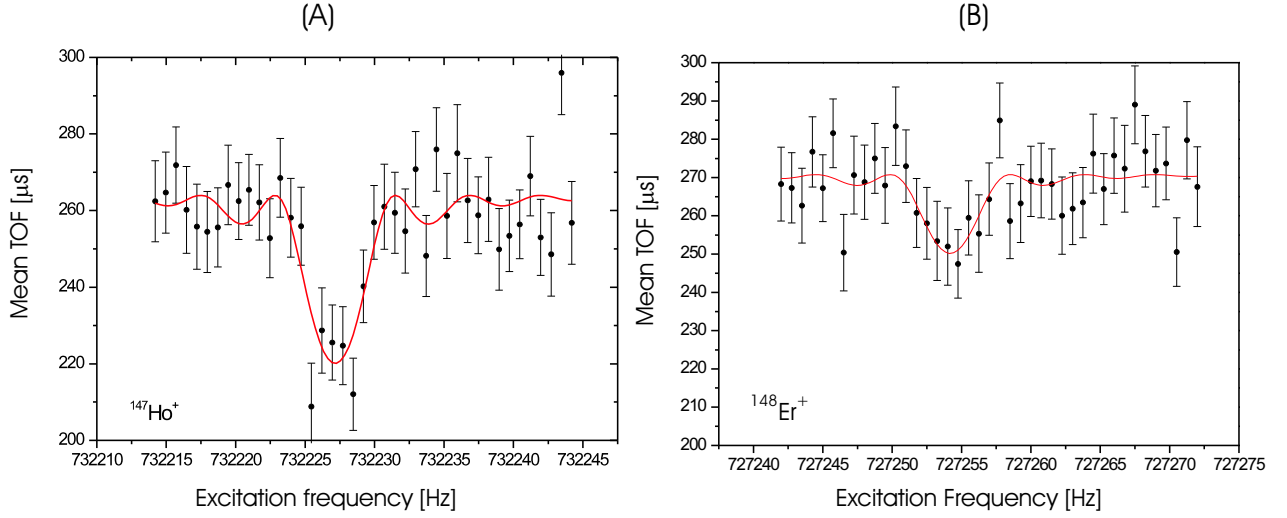
Figure 8.8: (A:) Time-of-flight resonance of ^{147}Ho$^+$ trapped in the measurement trap. The line shows a fit to the data points using the theoretically expected line shape. The linewidth corresponds to a resolving power m/$\Delta m = 1.6 \times 10^5$ for 200 ms excitation time. The TOF effect was about 16%. (B:) Time-of-flight resonance of ^{148}Er$^+$ from the measurement trap. The TOF effect was about 9%.

is low compared to typical values of 30% obtained for Cs resonances. The reduction of the TOF effect is due to impurity ions. They are not affected by the exciting RF field and hence their time of flight is not reduced on resonance but they contribute to the mean time of flight shifting it to a higher value. Because of the low count rate and the time required to deal with the impurity problem, which were only under some control at the end of the run, only two resonances for each nuclide could be recorded.

From the resonances shown in Fig. 8.8, a cyclotron frequency for ^{147}Ho and ^{148}Er of 732226.487 and 727254.394 is obtained from a fit of the theoretical line shape to the data points. Concerning the magnetic field calibration the same procedure as mentioned in Section 8.5 and Chapter 7 was applied. A TOF resonance for the reference ion ^{133}Cs was recorded before and after the actual frequency measurement of the ion of interest. Then the magnetic field was linearly interpolated to the time of the actual measurement. It should be mentioned that the reference measurements were not taken in regular intervals. Since the count rate for the reference ion can be controlled by the operating parameters of the reference ion source a sufficiently high rate was chosen to limit the time for a reference measurement to about 15 minutes. The final experimental result from the experiment is the frequency ratio between the ion of interest and the reference ion given in Tab. 8.3. The mass value can then be calculated at any time using the most recent and hence most precise value of the reference mass available. The error in the frequency ratio is calculated according to Eq. (7.13) and includes in the case of SHIPTRAP only the error in the center frequency determination from the

fit to the cyclotron resonance and the error from the interpolation of the magnetic field. In addition the z class analysis described in Section 7.2 was applied to correct for frequency shifts due to contaminant ions. The mass dependent error as observed for ISOLTRAP (see Chapter 7.5) is expected to be negligible here. If it was on a similar order as for ISOLTRAP it would contribute a level of 10^{-8} which is small as compared to the statistical error. The same holds for the other errors discussed in chapter 7, since these uncertainties have not yet been determined for SHIPTRAP. A carbon cluster ion source to allow for cross correlation mass measurements to determine the systematic uncertainties as discussed by [Kellerbauer03] is currently being commissioned. In addition long-term measurements of the magnetic field stability will be pursued from which the error introduced by a linear interpolation of the magnetic field can be determined. Table 8.3 summarizes the frequency ratio as well as the mass value obtained for ^{148}Er and ^{147}Ho using the TOF-ICR technique.

Table 8.3: Results from the analysis on ^{148}Er and ^{147}Ho measured with the precision trap of SHIPTRAP. $\overline{r}$ is the mean frequency ratio between the ion of interest and ^{133}Cs$^+$ calculated according to Eq. (7.6). N_{total} is the total number of detected ions. m_{atomic} is the atomic mass calculated according to Eq. (7.10). $\delta m_{atomic}/m_{atomic}$ represent the relative mass accuracy.

Nuclei	$T_{1/2}$	Frequency ratio($\overline{r}$)	N_{total}	m_{atomic} [u]	$\delta m_{atomic}/m_{atomic}$
^{148}Er	4.6 s	1.113 158 4(17)	2965	147.944 76(21)	1.4×10^{-6}
^{147}Ho	5.8 s	1.105 600 3(18)	2269	146.940 25(21)	1.3×10^{-6}

The relative accuracy achieved in this first measurements is about 10^{-6} which is the same order as obtained in the results from the purification trap measurements.

This is not very surprising since the resolution achieved in the measurement trap was only about a factor of two higher than in the purification trap. Additionally, the error bar of the final result from the TOF-ICR measurement increases due to the extrapolation of the cyclotron frequency to one ion in the trap.

8.7 Compilation of results

The Atomic Mass Excess of the Er and Ho isotopes is presented in Tab. 8.4. The Mass Excess was calculated according to

$$ME = [m_{atomic} - A] \tag{8.6}$$

where A is the atomic mass number of the nucleus, and m_{atomic} is the atomic mass of the nucleus in u.

The mass of ^{147}Er was previously only known from extrapolations using systematic trends [Audi03]. It has to be mentioned that this nuclide has a long-lived isomeric

Table 8.4: Comparison of the in the beam time of July 2004 measured mass excesses (ME) to the Atomic Mass Evaluation. Values obtained from the measurements in the purification trap are marked by $\star$, those form the measurements in the measurements Penning trap are by $\dagger$. ME_{lit} are the AME values from 2003 [Audi03]. The values for the erbium nuclides given by the AME are only an extrapolated ones. In the last row, the mean value of the two mass determinations of ^{147}Ho in given. Values labelled with # are estimated from systematic trends in AME2003.

Nuclei	ME_{expt} [keV]	ME_{lit} [keV]	ME_{expt} - ME_{lit} [keV]
^{147}Er	-46464(168)$\star$	-47050(300)#	585
^{147}Ho	-55729(122)$\star$	-55837(28)	107
^{148}Er	-51454(198)$\dagger$	-51650(200)#	195
^{147}Ho	-55647(204)$\dagger$	-55837(28)	189
^{147}Ho	-55707(104)	-55837(28)	130

state with a half-live comparable to the one of the ground state. The excitation energy of the isomer is about 100 keV so the isomeric state was not resolved. This may be a reason why the result deviates from the extrapolated AME value for the ground state by 585 keV. The mass of ^{147}Ho was previously measured at the ESR storage ring [Litvinov4] with a lower uncertainty but the results agree within their uncertainties. The result obtained for ^{147}Ho in the measurement trap is in agreement with the one obtained from the purification trap presented. For the first time a direct mass measurement ^{148}Er, ^{147}Er and ^{147}Ho are summarized in Tab. 8.4.

The mass measurements on ^{147,148}Er and ^{147}Ho performed at SHIPTRAP in July 2004 were a first test suffering from a number of problems so that finally only a moderate precision was achieved. Nevertheless, the two erbium masses were experimentally measured for the first time.

8.8 SHIPTRAP efficiency

Another important information from the first on-line mass measurements is the overall efficiency of the complete set-up. It can be derived comparing the number of ions detected on MCP3 to the number of ions detected on a silicon detector in front of the stopping cell. The number of ^{147}Ho ions detected at the silicon detector in front of the cell is determined from a spectrum as shown in Fig. 8.2. For a primary beam current of 400 pnA about 13,000 secondary ions per second are detected. Since the different evaporation residues contained in the second peak cannot be resolved the total number of ions in the peak is multiplied with the calculated fraction of ^{147}Ho produced according to the calculated production cross sections which is about 0.6. Hence, 7800 ^{147}Ho ions entered the gas cell per second. The current detected on the beam stop was

used for scaling.

The number of ^{147}Ho ions detected on MCP3 was calculated from the total number of ions contributing to cyclotron time of flight resonance of ^{147}Ho as shown in Fig. 8.8 minus a background of about 0.1 ions per second. A value of 0.1 ions per second was obtained resulting in an overall efficiency of 1.3×10^{-5}.

This value has to be compared to a calculated efficiency based on the efficiencies of individual components of the set-up, previously measured in off- and on-line tests. For the subsystem of stopping cell, extraction RFQ and RFQ buncher a transmission efficiency of 3% was measured in test runs at Garching and GSI [Neumayr04]. As discussed already in Section 8.2, due to a too thick entrance window only 15% transmission through the foil could be reached according to SRIM calculations. The efficiency of the transfer section between buncher and Penning trap system was determined in off-line tests to be 90 %. The efficiency for capturing, storing and ejecting bunches for the two traps has been measured to be 80%. For the last micro-channel plate detector (MCP3) a detection efficiency of 20% was expected. With all these numbers an overall efficiency of 6.5×10^{-4} was expected. This is a factor of 60 larger than observed. The reason for this deviation was later found to be due to the not properly working MCP3 detector. Its actual detection efficiency was measured after the run to be only 0.5% giving an overall efficiency of 3.2×10^{-5} in fair agreement with the experimental value.

8.9   Discussion of results

In this section the implications for nuclear structure will be discussed that can be obtained from the performed mass measurements. Systematic nuclear structure studies require a large amount of data so the discussion will mainly focus on the future potential. The region around ^{147}Ho is interesting because of its vicinity to a region of ground-state proton radioactivity, which was discovered at SHIP. For instance ^{146}Tm is an odd-odd proton emitter, lying in the transitional region between predicted deformed and near-spherical shapes. The key parameter here is the proton separation energy which can be derived from atomic masses. Still today, there are many masses in this region which are so far experimentally unknown. Another issue for these nuclei is to investigate the neutron shell closure at N = 82. Continuing the mass measurements in this region of the nuclear chart with an improved precision and extending them to more nuclides approaching the drip-line will also provide valuable information on nuclear structure.

Two-neutron separation energy around the N = 82 shell closure

The nucleon separation energy is the energy that is needed to remove a certain number of nucleons as for instance two neutrons from the atomic nucleus. Because of the pairing effect, the single-nucleon separation energy is a less clear-cut indicator. Two-nucleon separation energies provide basic information on the nuclear shell structure. Plotting the neutron separation energy as a function of the neutron number makes a
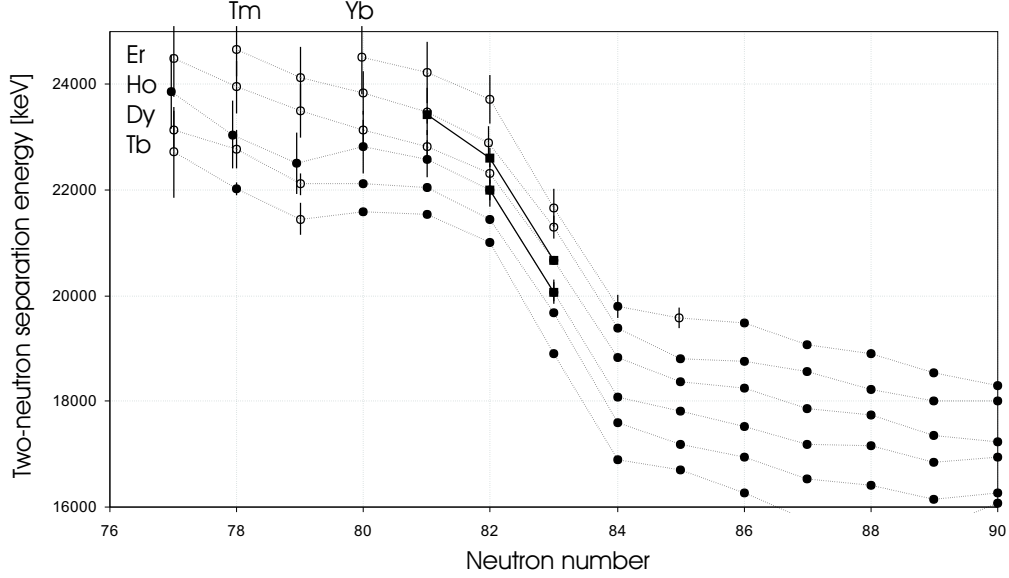
Figure 8.9: Two-neutron separation energy as a function of neutron number for 77 $\leq N \leq 90$. The filled circles present the experimental data from AME-2003 and the open circles present estimated values from systematic trends. Two-neutron separation energies calculated for ^{149}Er and the semi-magic ^{150}Er and ^{149}Ho isotopes using the newly measured mass values at SHIPTRAP are indicated by filled squares.

shell closure visible as a kink since the neutrons in a closed shell are stronger bound. The two-neutron separation energy is defined as

$$S_{2n}(N, Z) = B(N, Z) - B(N - 2, Z). \tag{8.7}$$

Using the mass values from the AME together with the measured mass values of ^{147,148}Er and ^{147}Ho from SHIPTRAP the two-neutron separation energy (S_{2n}) was calculated for five elements in the range of neutron number from N = 77 to N = 90. The result is shown in Fig. 8.9. In this plot the experimentally obtained values for the two-neutron separation energy for the magic isotopes ^{150}Er and ^{149}Ho are indicated by filled squares (with solid line). The empty circles (with dashed line) indicate the values from systematic trends and the filled circles (with dashed line) indicate experimentally values, both from AME 2003. In general a similar trend is observed for all considered nuclides. The two-neutron separation energy S_{2n} falls steadily as the neutron number N increases for constant proton number. This is a liquid-drop characteristic, and follows from the Weizsäcker mass formula given in Eq. (1.2). The expected kink at N = 82 indicating the neutron shell closure is observed. For very neutron-deficient holmium isotopes (around N = 78) a deviation from the trend of the neighboring elements is observed. For erbium the measured value from SHIPTRAP also deviates from the trend because the ^{147}Er nucleus is considerably weaker bound than expected. Since ^{147}Er has an isomeric state with a half-live comparable to the one of the ground

state and the state assignment is unclear this deviation might be reduced by about 100 keV, if the SHIPTRAP measurements contained 100% of the excited state. To clarify if this deviation is indeed due to nuclear structure changes there are two steps needed. First, a repeated mass measurement with sufficiently high resolving power in the measurement trap should be performed to identify the isomeric state as well as the ground state. Second, the mass of ^{145}Er needs to be determined experimentally in order to discriminate eventually present difficulties with the extrapolation.

Chapter 9

Mass measurements of neutron-rich Ra and Fr nuclei with ISOLTRAP

Mass measurements on heavy neutron-rich nuclei above ^{208}Pb are of great interest because of several reasons. Many mass values in this region are unknown although some nuclides have half-lives up to minutes. A profound understanding of this region is required to predict the properties of super-heavy elements. Here, the half-lives for α-decay and spontaneous fission are very sensitive to shell corrections [Patyk89]. For the production of super-heavy elements it is of primary interest to test those shell corrections around Z = 82, the next heavy shell closure. Furthermore, ^{232}U and ^{232}Th are key nuclei for cosmochronometry [Schatz02]. However, exact dating requires the knowledge of the formation of these two nuclides which is especially difficult for the long-lived ^{232}Th. An in-depth knowledge of the r-process path and subsequent β-decay towards ^{232}Th is needed. This requires new experimental mass data towards the neutron-rich side.

The present work extends previous investigations by ISOLTRAP [Bollen92b, Weber04] in this region towards the neutron-rich side of the valley of beta-stability. With ISOLTRAP, the masses of the short-lived nuclides ^{230}Fr and $^{229-232}$Ra have been measured with a relative accuracy of 10^{-7}. The mass values of ^{230}Fr and ^{231,232}Ra were determined experimentally for the first time. Furthermore, ^{232}Ra is the heaviest nuclide which has been investigated in a Penning trap ever.

9.1 The experiment

The francium and radium isotopes were produced the on-line isotope separator ISOLDE at CERN/Geneva [Kugler00] in spallation reactions by bombarding a uranium carbide target with an intense high-energy proton beam from the CERN PS-Booster accelerator. 2.2×10^{13} protons per pulse with an energy of 1.4 GeV impinging on the target every 2.4 s.

The produced atoms would then diffuse out from the hot (≈ 2000 K) target region and get surface ionized in a tungsten ionizer cavity. Table 9.1 indicates the production yields

Table 9.1: Production yields of francium and radium isotopes at ISOLDE/CERN. A uranium carbide target with a thickness of 54 g/cm^2 was used.

Isotope	Production yields [ions/proton pulse]	Production yields [ions/s]
^{230}Fr	8.2×10^4	3.4×10^4
^{230}Ra	3.1×10^7	1.3×10^7
^{232}Ra	8.2×10^5	3.4×10^5
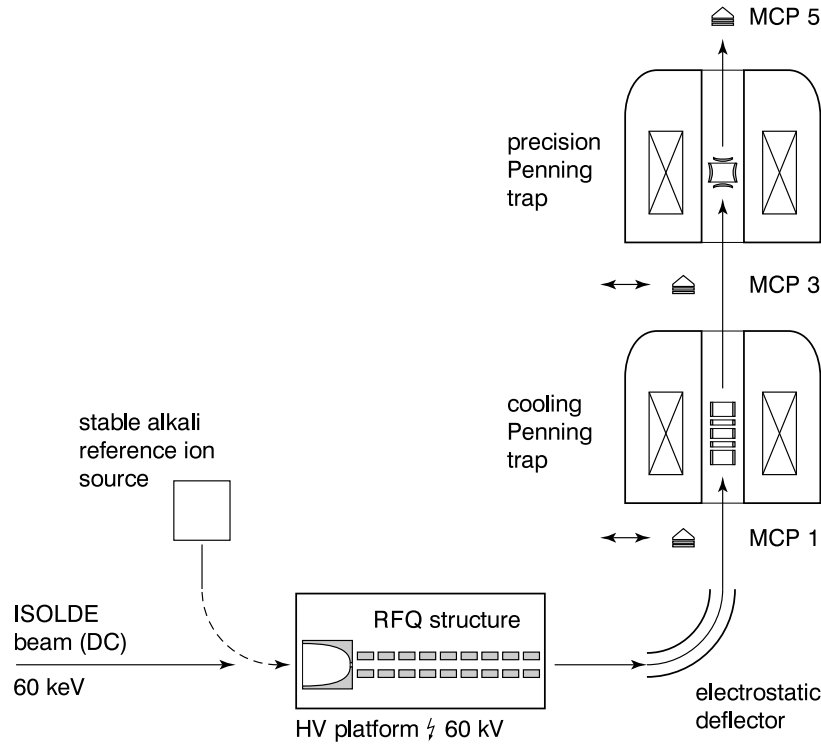
Figure 9.1: Sketch of the ISOLTRAP setup. It consists of a reference ion source delivering stable isotopes of alkali elements, the radiofrequency quadrupole RFQ ion beam cooler and buncher, the cooling Penning trap and the precision trap. Micro-channel plate (MCP) detectors are located along the beam line for beam diagnostics purpose.

of the investigated Ra and Fr isotopes. The ions were accelerated to 60 keV and mass separated using the General Purpose Separator (GPS), a magnetic mass separator with a resolving power of $\frac{m}{\Delta m} = 700$. The ions were then transported to the ISOLTRAP set-up [Bollen92a, Blaum03] for precision mass measurements (see Fig. 9.1). They were first decelerated, radially cooled and bunched in the RFQ ion beam cooler and buncher [Herfurth01b] subsequently, the cooled ions were transported to the cylindrical cooling Penning trap [Raimbault97, Beck97a] inside a superconducting magnet of field strength B = 4.7 T where isobaric contaminants were removed through mass-selective

cooling [Savard91]. The mass resolving power of the cooling Penning trap was about $\frac{\nu_c}{\Delta\nu_c} = 10^5$. The purified ion sample was then send to the last stage, a hyperbolic Penning trap inside a superconducting magnet of field strength B = 5.9 T. The mass resolving power of the precision Penning trap was about $\frac{\nu_c}{\Delta\nu_c} = 10^6$ to 10^7. There the actual mass measurement was carried out using the time-of-flight cyclotron resonance technique (see Section 3.4.1).

A surface ion source producing ions of stable alkali isotopes, was used to tune the beam transport and trap parameters. $^{133}Cs^+$ ions were used as reference ions to determine the magnetic field strength. A typical example of a time-of-flight cyclotron resonances for $^{229-232}Ra^+$ and $^{230}Fr^+$ are shown in Fig. 9.2.
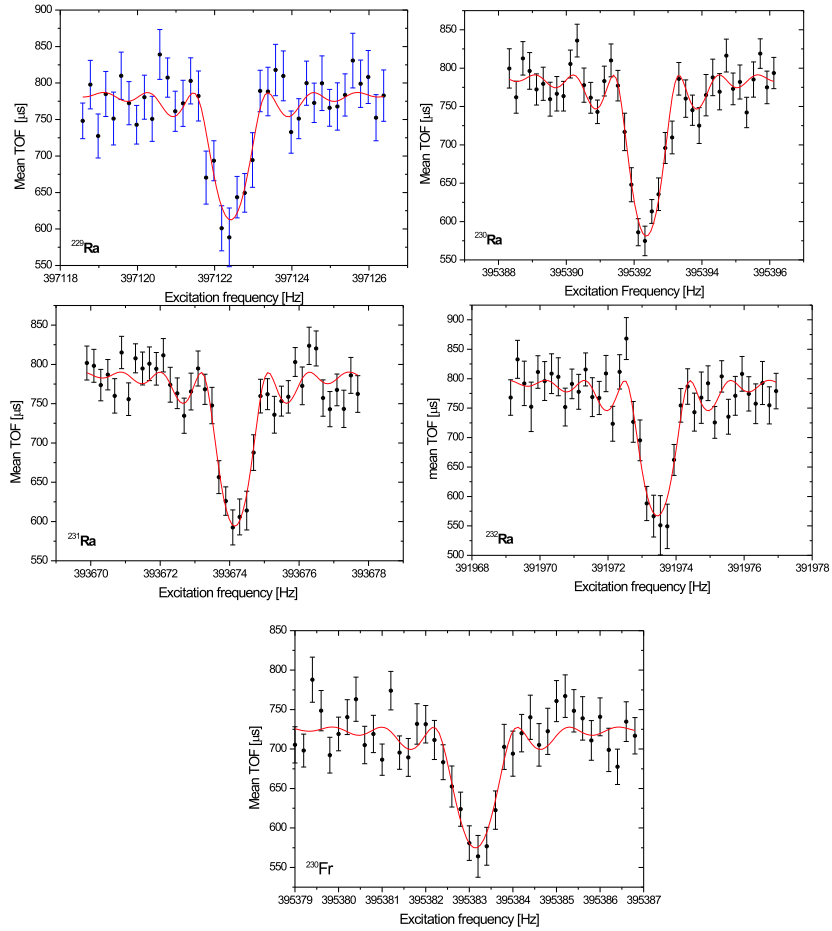
Figure 9.2: Time-of-flight resonances for $^{229-232}Ra^+$ and $^{230}Fr^+$ ions measured at ISOLTRAP mass spectrometer. The solid line corresponds to a fit of the theoretically expected function to the data [König95]. The center frequency is used for the mass determinations.

9.2   The mass measurement results

The experimental result of a ISOLTRAP measurement is the ratio of cyclotron frequency of the reference ion and the ion of interest. This ratio has been measured two times for ^{231,232}Ra and only once for ^{229,230}Ra and ^{230}Fr. Therefore the statistical uncertainty dominates in the final uncertainty. The frequency ratio can then be converted to an atomic mass m_{atomic} according to Eq. (7.10). In Tab. 9.2 the experimental results are summarized for the nuclides investigated here.

Table 9.2: Results of the measurements of ^{229,230,231,232}Ra and ^{230}Fr determined at ISOLTRAP. $T_{1/2}$ represents the half-life of the nuclei. N_{total} is the total number of detected ions. m_{atomic} represents the atomic mass calculated according to Eq. (7.10) taking into account the reference mass $m(^{133}Cs^+) = 132.905\ 451\ 93(27)$ u [Audi03], and the mass of the electron $m_e = 0.000548579910(12)$ u [Mohr99] with 1 u $= 931494.013(7)$ keV [Audi03]. The relative mass uncertainty is indicated by $\delta m_{atomic}/m_{atomic}$.

Nuclei	$T_{1/2}$	Frequency ratio$(\overline{r}) = \frac{\nu_{ref}}{\nu_c}$	N_{total}	m_{atomic} [u]	$\delta m_{atomic}/m_{atomic}$
^{229}Ra	4.0 min	1.723 295 23(20)	886	229.034 935(26)	1.1×10^{-7}
^{230}Ra	93.0 min	1.730 835 33(16)	2404	230.037 051(21)	0.9×10^{-7}
^{231}Ra	103.0 sec	1.738 389 50(16)	4697	231.041 037(21)	0.9×10^{-7}
^{232}Ra	4.2 min	1.745 932 03(10)	1958	232.043 476(13)	0.5×10^{-7}
^{230}Fr	19.1 sec	1.730 875 61(24)	1329	230.042 405(32)	1.3×10^{-7}

The mass excess ME of a nucleus is given by

$$ME = [m_{atomic} - A] \tag{9.1}$$

where A is the atomic mass number of the nucleus, m_{atomic} is the atomic mass of the nucleus in atomic mass units (u) defined as 1/12 of the mass of ^{12}C. The mass excesses of all known nuclides are tabulated in the Atomic Mass Evaluation (AME) [Audi03] which is constantly updated and published every few years [Audi93, Audi95, Audi03]. It is the result of a least-squares adjustment of all available experimental data on mass measurements, decay and reaction energies. The final results from the 2004 measurements are summarized in Tab. 9.3 along with a comparison to the values from the Atomic Mass Evaluation 2003 [Audi03].

^{229}Ra and ^{230}Ra

The mass values agree well with the previous measurements performed in 2002 at ISOPTRAP [Weber04] and the determining the mass values of these isotopes given in AME 2003 [Audi03]. The mass of ^{230}Ra was already determined in 1992 [Bollen92b], but less precise. The two frequency ratio (relative to ^{133}Cs) obtained for each, ^{229}Ra and ^{230}Ra, in 2002 [Weber04] and 2004 (present work) can be combined to yield mass

Table 9.3: Comparison of the measured mass excess with the values given in the Atomic Mass Evaluation 2003. ME_{expt} represents the experimental mass excess obtained from the cyclotron frequency ratio given in Tab. 9.2. $ME_{lit.}$ are the AME values from 2003 [Audi03]. With # labelled values are estimated from systematic trends.

Nuclei	ME_{expt} [keV]	$ME_{lit.}$ [keV]	ME_{expt} - $ME_{lit.}$ [keV]
^{229}Ra	32542(24)	32563(19)	20
^{230}Ra	34513(19)	34518(12)	4
^{231}Ra	38226(19)	38400(300 #)	173
^{232}Ra	40498(12)	40650(280 #)	151
^{230}Fr	39500(29)	39600(450 #)	99
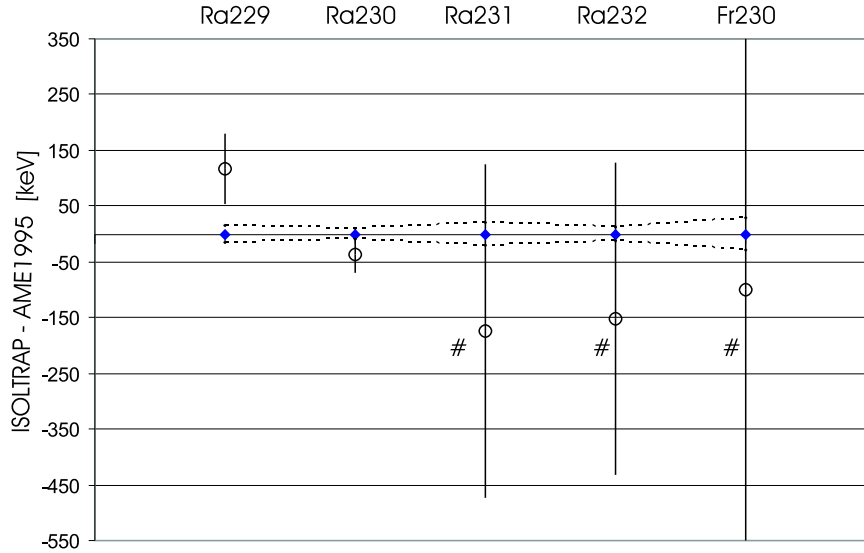
Figure 9.3: Mass excess differences between ISOLTRAP results of ^{229,230,231,232}Ra and ^{230}Fr and the results from the AME1995 [Audi95]. The ISOLTRAP values define the zero line (filled circles) and the open circles represent the AME1995 values. Values labelled with # are estimated from systematic trends in AME1995. The uncertainty of the ISOLTRAP data are depicted by dashed lines.

data with improved accuracy. This yields the values given in Tab. 9.4. The frequency ratios, measured in 2002 cited in Tab. 9.4, are without the mass dependent systematic shift.

These improved mass data for ^{229}Ra and ^{230}Ra and those of ^{231}Ra, ^{232}Ra and ^{230}Fr are compared with the mass values given in the Atomic Mass Evaluation presented 1995 AME1995 by G. Audi et. al [Audi95] since in the AME 2003 already part of the ISOLTRAP data was used.

Table 9.4: Frequency ratios for ^{229}Ra and ^{230}Ra relative to ^{133}Cs$^+$ as obtained in two different beam time taking place in 2002 [Weber04] and 2004 [this work] at ISOLTRAP and a results of a combination of both frequency ratios leading to improved values of the atomic mass and the mass excess.

nuclei	frequency ratio $\overline{r} = \frac{\nu_{ref}}{\nu_c}$ in 2002	frequency ratio $\overline{r} = \frac{\nu_{ref}}{\nu_c}$ in 2004	combined frequency ratio	m$_{atomic}$ [amu]	mass excess [keV]
^{229}Ra	1.72329547(16)	1.72329523(20)	1.72329537(12)	229.034953(15)	32558(15)
^{230}Ra	1.73083534(10)	1.73083533(16)	1.730835335(83)	230.037052(11)	34513(10)

The mass excess difference between the combined ISOLTRAP results and the results from the AME1995 are shown in Fig. 9.3. The previous mass value for ^{229}Ra nuclei measured via the end-point energy of the β-decay of ^{229}Fr [Westgaard75] deviates by 1.9σ from the combined ISOLTRAP mass value. In the case of ^{230}Ra the combined value agrees with the measurement from 1992 [Bollen92b]. This reflects the strong reliability of ISOLTRAP mass measurements.

^{231}Ra, ^{232}Ra and ^{230}Fr

The masses of the nuclides ^{231}Ra, ^{232}Ra and ^{230}Fr have been determined for the first time. The measured masses agree well with the values AME2003 [Audi03], extrapolated using systematic trends within the large uncertainties of the extrapolation.

9.3 Discussion

To investigate the nuclear structure by mass values, the two-neutron separation energy S_{2n} is very well suited (see Eq. (8.7)). The two-neutron separation energy S$_{2n}$ is known to carry the signature of the shell structure of the nucleus as well as of shape transitions and configuration mixing effects.

Figure 9.4 shows a plot of the two-neutron separation energy as a function of the neutron number for $130 \leq N \leq 155$. A steady fall of the S$_{2n}$ is observed as expected in this region in between the shell closures at N = 126 and N = 164. In this plot the experimentally obtained values for the two-neutron separation energy for $^{230-232}$Fr and $^{231-234}$Ra are included (filled diamonds with solid line). The empty circles (with dashed line) indicate the extrapolated values from systematic trends and the filled circles (with dashed line) indicate the measured value. The considerable reduction of the mass uncertainty as well as the first ever mass measurement of ^{230}Fr mark a clear change in the trend of the two neutron separation energy. While the extrapolation naturally delivered a smooth behavior, the experimental values do not follow this trend. A significant drop in the S$_{2n}$ values is observed between N = 144 and 145 for radium and for francium between N = 143 and 144.
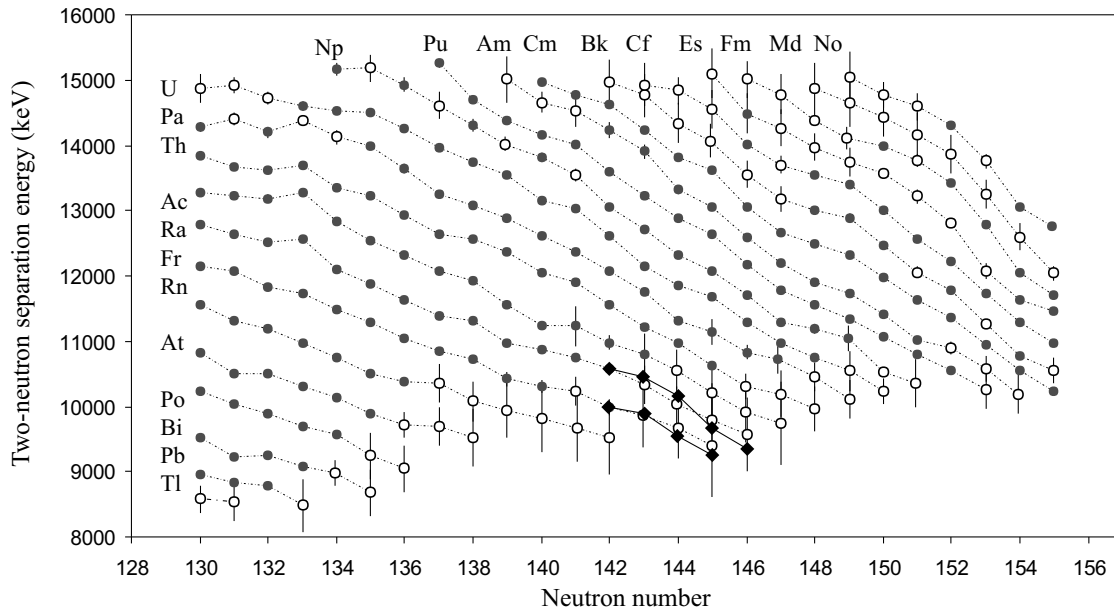
Figure 9.4: Two-neutron separation energy plotted versus the neutron number. Full circles mark experimental values as cited in the Atomic Mass Evaluation 2003 [Audi03]. Open circles result from an extrapolation [Audi03]. Data that include one of the radium or francium nuclides determined in this work are marked with diamonds and connected with a solid line and the error bars are indicated if they exceed the diameter of the symbols.

Another way to investigate the shell structure is the neutron shell gap defined as

$$\Delta_N(N_0, Z) = S_{2n}(N_0, Z) - S_{2n}(N_0 + 2, Z). \tag{9.2}$$

The investigated nucleus ^{232}Ra has N = 144 which is very close to mid-shell N = 145 (exactly in between two shell closures 126 and 164). The experimentally determined neutron shell gap as a function of neutron number is shown in Fig. 9.5. The open circles represent the francium and the filled triangles indicate the radium isotopes. With the expectation of the pronounced discontinuity at N = 126, which is a clear signature for a shell closure, the neutron shell gap is rather constant in this region of neutron numbers. Eventually a smooth and slow decrease is observed towards the neutron drip-line.

9.3.1 Comparing the experimental results with mass models

There is a large number of mass models. It is necessary to compare mass models to experimental results for their further development and to improve their in predictive power for regions very far from stability, where mass values are required to calculate the path of the r-process. A recent overview of those models can be found in [Lunney03]. The magic numbers that we know 2, 8, 20, 28, 50, 82 and 126 were established within the shell model at a time the data was limited to nuclei lying close to the line of
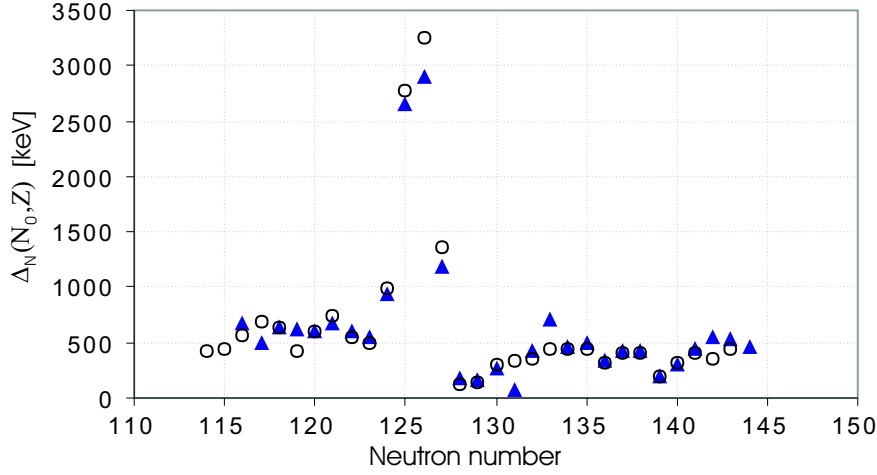
Figure 9.5: Experimentally determined neutron shell gap plotted as a function of neutron number. The open circles represent francium and the filled triangles indicate radium isotopes.

β-stability. There is an ongoing interest concerning new magic numbers that might appear in neutron-rich or proton-rich regions far away from the valley of β-stability in the nuclear chart [Lunney03]. Theoretical calculations using the Infinite Nuclear Matter model (INM) predict new islands of stability around N = 100, Z $\simeq$ 62; N = 150, Z $\simeq$ 78 and N = 164, Z $\simeq$ 90 in the neutron drip-line regions of the nuclear chart [Satpathy98, Satpathy04]. They also provide strong evidence for new neutron magic numbers at N = 100, 150 and 164; and a new proton magic number Z = 78. These have been recognized based on extrapolations of the two-neutron separation energies (S_{2n}) and their systematic deviations of the continuity properties.

The INM model is based on the quantum mechanical infinite nuclear matter rather than the classical liquid used in the liquid drop mass formulae of the Bethe-Weizsäcker model. In this model the ground state energy E^F(A, Z) of a nucleus is expressed as [Satpathy04]

$$E^F(A, Z) = E(A, Z) + f(A, Z) + \eta(A, Z), \tag{9.3}$$

where E(A, Z) being a property of nuclear matter, will satisfy the Hugenholtz and Van Hove (HVH) theorem of the many body theory and f(A, Z) characterizes the finite size effects which includes the usual surface, Coulomb and pairing terms. The key quantity in the INM model is η(A, Z), called the local energy, comprising all the characteristic features of a nucleus, which predominantly includes the shell effect and all the local effects such as deformation and diffuseness. The theoretical predictions of S_{2n} for francium and radium is shown in Fig. 9.6 by open circles. The experimentally determined values (filled symbols) have some deviation from the predicted values but still follow the predicated smooth behaviors of S_{2n}. A deviation is observed between the theoretical predictions and the experimental value near the shell closure 126, although
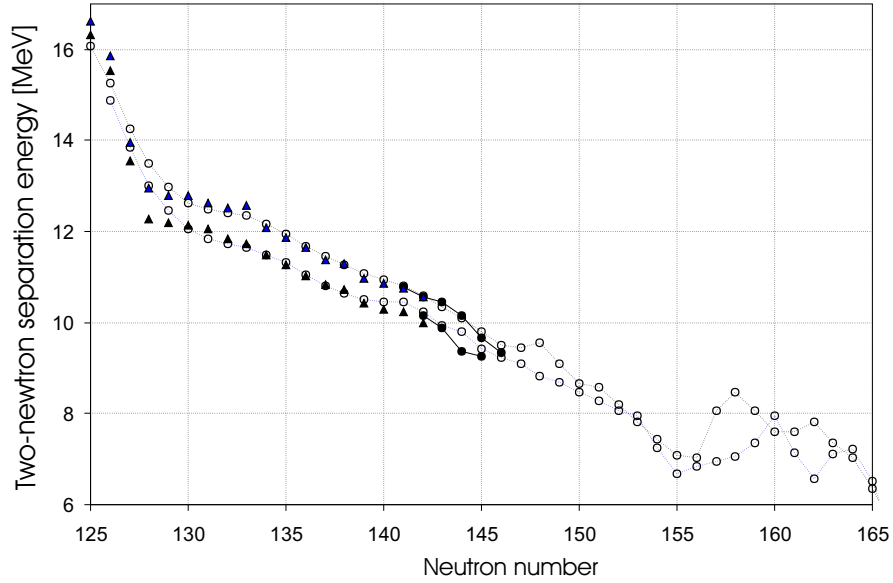
Figure 9.6: Two-neutron separation energy as a function of neutron number for N =125 to 165. The open circles present the theoretical calculation according to the INM model. Two-neutron separation energies calculated for $^{229-232}$Fr and $^{229-234}$Ra using the newly measured mass values are indicated by filled squares. The other experimental values, taken from AME2003, are indicated by filled triangles.

both results carry it's magicity information. However, especially interesting would be to see if the experimental data reproduce the increase of the S_{2n} energies in the model as the neutron number reaches N = 156. However, data on such neutron-rich heavy isotopes are presently out of reach of any mass spectrometric technique.

Chapter 10

Summary and outlook

In the course of this work, the Penning trap mass spectrometer at SHIPTRAP at GSI/Darmstadt was extensively tested, optimized, commissioned and employed for the very first time for precision mass measurements of radioactive isotopes. Although quite a number of problems showed up such as a large number of contaminating ions and a poor detector efficiency, the masses of two isotopes ^{147}Er and ^{147}Er could be determined for the first time. Furthermore, a precision mass measurement of the heaviest neutron-rich radium and francium isotopes was performed at ISOLTRAP CERN/Geneva. This work extends the investigations of nuclear structure in the region towards the neutron-rich side of the valley of β-stability. The results are compared with the predictions of Infinite Nuclear Matter model.

SHIPTRAP consists of three main functional parts: (i) a gas cell for stopping the energetic ions produced by a fusion reaction and separated by the velocity filter SHIP, (ii) radiofrequency quadrupole structures to cool and to bunch the ions extracted from the gas cell and, (iii) a superconducting magnet housing two Penning traps, the so-called purification and measurement trap. This thesis is focused on the characterization of the Penning traps as well as first on-line experiments.

The purification trap at SHIPTRAP is used for mass-selective buffer gas cooling. Systematic investigations were carried out to study the efficient injection of ions into the trap and to optimized the potentials applied to the trap electrodes. At present a maximum mass resolving power of $\frac{m}{\Delta m} = 85{,}000$ could be achieved with a 400 ms total cycle time. The cooling time depends on the helium pressure in the trap. Generally, higher helium pressures allow for shorter cooling times but the resolving power will be reduced. A shorter cooling time of 150 ms was applied resulting in a mass resolving power $\frac{m}{\Delta m} = 40{,}500$.

The measurement trap of SHIPTRAP is dedicated to precision mass measurements. For this trap, the timing for capturing the ions in the trap, excitation by radiofrequency and the mass resolving power as a function of excitation time were investigated during the commissioning phase. A storage time of about 1.2 second could be realized without

any loss of ions from the trap. A resolving power of about $\frac{m}{\Delta m} = 850,000$ was achieved using a 900 ms radiofrequency excitation in agreement with the Fourier limit for such an excitation time.

Regarding the efficiency of the Penning trap system, systematic measurements were performed. A transmission efficiency of about 40% was achieved for a DC ion beam steered through the strong magnetic field of the superconducting magnet. A trapping, cooling and centering efficiency of the purification trap of about 95% was measured. The transfer efficiency from the purification trap to the measurement trap was determined to be about 80%.

After commissioning all individual components of the SHIPTRAP set-up, the facility was used to measure the masses of the short-lived ^{147,148}Er and ^{147}Ho isotopes which are produced at SHIP by fusion reactions with an energy of 650 keV/u and a production rate of few 1,000 ions per second. These radionuclides are the first ones the mass of which could be determined by SHIPTRAP.

A total efficiency of the complete set-up of about 10^{-5} was measured during this first beam time taking place in July 2004. This gives access to radioactive ions with a production rate of a few 1,000 ions per second. Still there are many parameters that can be optimized to improve the efficiency of the system. For example, the MCP detector efficiency was later found to be only 2% during the beam time. Also the stopping and extraction efficiency of the gas cell can be further improved. Thus an improvement in efficiency by two orders of magnitude seems feasible. This will open the possibility to access radioactive ions which are produced at a rate of about 100 ions per seconds. Therefore one can access very heavy elements in the near future and measure their masses which are only known from extrapolations with an uncertainty of few 100 keV. Still, the ion extraction out of the measurement trap is not fully optimized and ion detectors reaching nearly 100% detection efficiency are being developed. So there is a fair chance for further improvement of the efficiency of the system.

For the first time the masses of ^{147,148}Er were determined. During the beam time contaminating ions other than the one under investigation represented a major problem. The achieved accuracy of about 170 to 190 keV, equivalent to a relative accuracy $\delta m/m$ of 1×10^{-6} was limited by these contaminations. Measures have to be developed and tested to suppress the creation of unwanted ions. This is mainly an issue of the purity of the used He gas and proper outgassing of the set-up.

The investigated nuclei are located in a region where proton emission occurs as in the case of ^{146}Tm and ^{151}Lu. Since proton radioactivity depends on the proton separation energies it is interesting to determine the nuclear mass. Nuclear structure effects are important in this case. For example, ^{146}Tm is an odd-odd proton emitter, lying in the transitional region between predicted deformed and near-spherical shapes.

In the course of this thesis work, the masses of the short-lived nuclides $^{229-232}$Ra and ^{230}Fr have been measured with the ISOLTRAP set-up with an accuracy of 1×10^{-7}. The

mass values of ^{229}Ra and ^{230}Ra were found to be in good agreement with the values obtained at ISOLTRAP during previous experiments. The mass values of ^{231,232}Ra and ^{230}Fr were previously unknown and have been determined experimentally for the first time. Furthermore, ^{232}Ra is the heaviest element ever investigated in a Penning trap and represents, therefore, a good starting point for the measurements planned at SHIPTRAP.

This work extends the previous investigations at ISOLTRAP in this region towards the neutron-rich side of the valley of β-stability. The experimentally determined two-neutron separation energies S_{2n} values for $^{229-232}$Fr and $^{230-234}$Ra have a clear deviation from the ones given in the Atomic Mass Evaluation 2003, edited by G. Audi and A. H. Wapstra. The values for ^{231,232}Ra and ^{230}Fr are extrapolated masses assuming a smooth tread of the mass surface. The results are also compared to theoretically calculated two-neutron separation energies. For francium and radium a steady fall of the two-neutron separation energy S_{2n} is expected according to the Infinite Nuclear Matter model in the region around N = 140 to 150. The experimentally determined values are in good agreement with these predictions.

Acknowledgments

I am much indebted to many people who have given me help and encouragement for my work. First, I would like to thank my supervisor Professor H.-Jürgen Kluge, who gave me the opportunity to study this interesting field of the trapping technique for mass measurements of heavy elements.

I am deeply grateful to Dr. Michael Block, Priv. Doz. Wolfgang Quint, Dr. Frank Herfurth and Dr. Gerrit Marx, who sincerely took care of me and gave me advices and comments in the course of the experiment and thesis writing. I should mentioned that the GSI net connection was shut-down in the last two days of my thesis writing, even in this situation Michael Block was working together with me to finish my thesis according to the University date.

Special gratitude to my present colleagues at SHIPTRAP, Dr. Sergey Eliseev, Christian Rauth, Manas Mukherjee and Ankur Chaudhuri. I should not forget to thank my previous colleagues Dr. Günther Sikler, Dr. Christine Weber, Dr. Daniel Rodríguez and Dr. Medhi Tarisien. I remember my hard time to translate the summary of the thesis from English to German language, which was finally possible together with the help of Christine Weber.

I would like to thank the SHIP people, Dr. Sigurd Hofmann, Dr. Fritz P. Hessberger and Dr. Dieter Ackermann for their continuous support during the experiments.

Special thanks to Dr. Dietrick Beck for his continuous support to the SHIPTRAP control system.

I thank Dr. Christophor Kozhuharov for his support to the SHIPTRAP group.

I must thank our close collaborators Dr. Jürgen Neumayr from Maier-Leibnitz Laboratory (MLL) at Garching and Dr. Wolfgang Plus from Giessen University.

I would like to thank the all stuff of the mechanical workshop of GSI for providing the necessary help for building the parts for the experiments.

I would also like to thank for the continuous support of our trapper friends, from ISOLTRAP at CERN and JYFLTRAP at Jyväskylä. Special thanks to Dr. Klaus Blaum for his guidance during the visit of ISOLTRAP experiment.

Finally, I thank all my brothers and sister for their patience and forbearance. I thank my parents for their support, understanding and encouragement. Special thanks to my brother Najme Alam and Dr. Azizur Rahaman for their contribution on my way to reach here. I must thank Joly for her sacrifices during my PhD and her continuous support and encouragement.

Bibliography

[Anderson62] P. W. Anderson, "Theory of Flux Creep in Hard Superconductors", Phys. Rev. Lett. **9** (1962) 309.

[Anderson64] P. W. Anderson and Y. B. Kim, "Hard Superconductivity: Theory of the Motion of Abrikosov Flux lines", Rev. Mod. Phys. **39** (1964) 39.

[Audi93] G. Audi, A. H. Wapstra, "The 1993 Atomic Mass Evaluation: (II) Atomic mass table", Nucl. Phys. A **565** (1993) 1.

[Audi95] G. Audi, A. H. Wapstra, "The 1995 update to the Atomic Mass Evaluation", Nucl. Phys. A **595** (1995) 409.

[Audi03] G. Audi, A. H. Wapstra and C. Thibault, "The AME2003 Atomic Mass Evaluation", Nucl. Phys. A **729** (2003) 337.

[Bachelet04] C. Bachelet, G. Audi, C. Gaulard, C. Guénaut, F. Herfurth, D. Lunney, M. De Saint Simon, C. Thibault and the ISOLDE collaboration, "A new high precision binding energy for the halo nuclide ^{11}Li", ENAM04 to be published.

[Beck97a] D. Beck, PhD Thesis, "Massenbestimmung instabiler Isotope der Seltenen Erden um ^{146}Gd mit dem ISOLTRAP-Spektrometer", Mainz, 1997.

[Beck97b] D. Beck, F. Ames, G. Audi, G. Bollen, H.-J. Kluge, A. Kohl, M. König, D. Lunney, H. Raimbault-Hartmann, S. Schwarz, J. Szerypo, and the ISOLDE Collaboration, "Towards higher accuracy with the ISOLTRAP mass spectrometer", Nucl. Inst. Methods B, **126** (1997) 374.

[Beck04] D. Beck, K. Blaum, H. Brand, F. Herfurth, S. Schwarz, "A new control system for ISOLTRAP", Nucl. Inst. Methods A **527** (2004) 567.

[Beier02] T. Beier, H. Häffner, N. Hermanspahn, S. G. Karshenboim, H.-J. Kluge, W. Quint, S. Stahl, J. Verdú, and G. Werth, "New Determination of the Electron's Mass", Phys. Rev. Lett. **88**, (2002) 011603.

[Bergström02] I. Bergström, C. Carlberg, T. Fritioff, G. Douysset, J. Schönfelder, R. Schuch, "SMILETRAP: A Penning trap facility for precision mass measurements using highly charged ions", Nucl. Inst. Methods A **487** (2002) 618.

[Beverini88] N. Beverini, V. Lagomarsino, G. Manuzio, F. Scuri, G. Testera, and G. Torelli, "Experimental verification of stochastic cooling in a Penning trap", Physica Scripta, **T22** (1988) 238.

[Bianchi89] L. Bianchi, B. Fernandez, J. Gastebois and A. Gillirert, "SPEG: An energy loss spectrometer for GANIL ", Nucl. Inst. Methods A, **276** (1989) 509.

[Blaum02] K. Blaum, G. Bollen, F. Herfurth, A. Kellerbauer, H.-J. Kluge, M. Kuckein, E. Sauvan, C. Scheidenberger, and L. Schweikhard, "Carbon clusters for absolute mass measurements at ISOLTRAP" Eur. Phys. J. **A15**, (2002) 245.

[Blaum03] K. Blaum, G. Bollen, F. Herfurth, A. Kellerbauer, H.-J. Kluge, M. Kuckein, S. Heinz, P. Schmidt, and L. Schweikhard, "Recent developments at ISOLTRAP: towards a relative mass accuracy of exotic nuclei below 10^{-8}", J. Phys. **36** (2003) 921.

[Blaum04] K. Blaum, "Private communication"

[Bollen90] G. Bollen, R. B. Moore, "The accuracy of heavy-ion mass measurements using time of flight-ion cyclotron resonance in a Penning trap", J. Appl. Phys. **68** (1990) 9.

[Bollen92a] G. Bollen, H.-J. Kluge, M. König, T. Otto, G. Savard, H. Stolzenberg, R. B. Moore, G. Rauleau, G. Audi, and the ISOLDE collaboration, "Resolution of nuclear ground and isomeric states by a Penning trap mass spectrometer", Phys. Rev. Lett. C **46** (1992) 2140.

[Bollen92b] G. Bollen, H.-J. Kluge, Th. Otto, G. Savard, L. Schweikhard and H. Stolzenberg., "Mass determination of francium and radium isotopes by Penning trap mass spectrometer", J. Mod. Opt. **39** (1992) 257.

[Bollen96] G. Bollen, S. Becker, H.-J. Kluge, M. König, R. B. Moore, T. Otto, H. Raimbault-Hartmann, G. Savard, L. Schweikhard, H. Stolzenberg, and the ISOLDE collaboration, "A Tandem Penning Trap System for Accurate On-Line Mass Determination of Short-Lived Isotopes", Nucl. Inst. Methods A **368** (1996) 675.

[Bollen01] G. Bollen, "Mass Measurements of Short-Lived Nuclides with Ion Traps", Nucl. Phys. A **693** (2001) 3.

[Bohr98]   A. Bohr, B. R. Mottelson, "Nuclear Structure", World Sceintific Publ. Singapore, 1998.

[Brown86]   L. S. Brown and G. Gabrielse, "Geonium theory: Physics of a single electron or ion in a Penning trap", Rev. Mod. Phys. **58** (1986) 233.

[Westgaard75] L. Westgaard, K. Aleklett, G. Nyman, E. Roeckl, "Beta-Decay Energies and Masses of Short-Lived Isotopes of Rubidium, Caesium, Francium, and Radium ", Z. Phys. **A275** (1975) 127.

[Comisarow86] M. B. Comisarow and N. M. M. Nibbering, "Fourier Transform Ion Cyclotron Resonance Mass Spectrometry", Int. J. Mass Spectr. Ion Proc. **72** (1986) 1.

[Comisarow74] M. B. Comisarow, A. G. Marshall "Fourier Transform Ion Cyclotron Resonance Spectroscopy", Chem. Phys. Lett. **25**, (1974) 282.

[Dawson95]   Peter H. Dawson, "Quadrupole mass spectrometry and its applications", American Institute of Physics Press, 1995.

[Dehmelt89]   H. G. Dehmelt, "Experiments with an isolated subatomic particle at rest", Rev. Mod. Phys. **62** (1989) 531.

[Dilling99]   J. Dilling, D. Ackermann, J. Bernard, F. P. Hessberger, S. Hoffmann, H.-J. Kluge, E. Lamour, M. Maier, R. Mann, G. Marx, G. Münzenberg, W. Quint, D. Rodríguez, M. Schädel, J. Schönfelder, G. Sikler, C. Toader, L.Vermeeren, C. Weber, G. Bollen, O. Engels, D. Habs, P. Thirolf, H. Backe, A. Dretzke, W. Lauth, W. Ludolphs, M. Sewtz and the SHIP-TRAP collaboration, "The SHIPTRAP project: A capture and storage facility at GSI for heavy radioniclides from SHIP", Hyp. Int. **127** (1999) 491.

[Dilling00]   J. Dilling, D. Ackermann, F. P. Hessberger, S. Hoffmann, H.-J. Kluge, G. Marx, G. Münzenberg, Z. Patyk, W. Quint, D. Rodríguez, C. Scheidenberger, J. Schönfelder, G. Sikler, A. Sobiczewski, C. Toader, C. Weber, "A Physics case for SHIPTRAP: Measuring the Masses of Transuranium Elements", Hyp. Int. **132** (2000) 495.

[Eliseev04]   S. Eliseev, PhD thesis, "Design Construction and Commissioning of an Ortho-TOF Mass Spectrometer for Investigations of Exotic Nuclei", Justus-Liebig university, Giessen, 2004.

[Fraser02]   G. W. Fraser, "The ion detection efficiency of microchannel plates (MCPs)", Int. J. Mass Spectr. Ion Proc. **215** (2002) 13.

[Gabrielse99]   G. Gabrielse, A. Khabbaz, D. S. Hall, C. Heimann, H. Kalinowsky, and W. Jhe, "Precision Mass Spectroscopy of the Antiproton and Proton Using Simultaneously Trapped Particles", Phys. Rev. Lett. **82** (1999) 3198.

[Gabrielse84]   G. Gabrielse and F. Colin, "Cylindrical Penning traps with orthogonalised anharmonicity compensation", Int. J. Mass Spectr. Ion Proc. **57** (1984) 1.

[Gabrielse89]   G. Gabrielse, L. Haarsma and S. L. Rolston, "Open endcap Penning traps for high precision experiments", Int. J. Mass Spectr. Ion Proc. **66** (19589 327.

[Gabrielse83]   G. Gabrielse, "Relaxation calculation of the electrostatic properties of compensated Penning traps with hyperbolic electrodes", Phys. Rev. A **27** (1983) 2277.

[Geissel95]   H. Geissel, G. Münzenberg, K. Riisagar, "Secondary exotic nuclear beams", Annu. Rev. Nucl. Sci., **45** (1995) 163.

[Geissel01]   H. Geissel, F. Attallah, K. Beckert, F. Bosch, M. Falch, B. Franzke, M. Hausmann, Th. Kerscher, O. Klepper, H.-J. Kluge, C. Kozhuharov, Yu. Litvinov, K. E. G. Löbner, G. Münzenberg, N. Nankov, F. Nolden, Yu. Novikov, T. Ohtsubo, Z. Patyk, T. Radon, C. Scheidenberger, J. Stadlmann, M. Steck, K. Sümmerer, H. Weick, H. Wollnik, "Progress in mass measurements of the stored exotic nuclei at relativistic energy", Nucl. Phys. A, **685** (2001) 115.

[Ghosh95]   P. K. Ghosh, "Ion Traps", Oxford University Press, 1995.

[Gräff80]   G. Gräff, E. Klempt, G. Werth, "A Direct Determination of the Proton-Electron Mass Ratio", Z. Phys. A **297** (1980) 35.

[Hartmann97]   H. Raimbault-Hartmann, D. Beck, G. Bollen, M. König, H.-J. Kluge, E. Schark, J. Stein, S. Schwarz, J. Szerypo, "A cylindrical Penning trap for capture, mass selective cooling, and bunching of radioactive ion beams", Nucl. Inst. Methods B **126** (1997) 1.

[Hausmann01]   M. Hausmann, J. Stadlmann, F. Attallah, K. Beckhert, P. Beller, F. Bosch, H. Eickhoff, M. Falch, B. Franczak, B. Franzake, H. Geissel, Th. Kerscher, O. Klepper, H.-J. Kluge, C. Kozhuharov, Yu. Litvinov, K. E. G. Löbner, G. Münzenberg, N. Nankov, F. Nolden, Yu. Novikov, T. Ohtsubo, T. Radon, H. Schatz, C. Scheidenberger, M. Steck, H. Weick, H. Wollnik, "Isochronous Mass Measurements of Hot Exotic Nuclei", Hyp. Int., **132** (2001) 291.

[Häffner00]   H. Häffner, T. Beier, N. Hermanspahn, H.-J. Kluge, W. Quint, S. Stahl, J. Verdú, and G. Werth, "High-Accuracy Measurement of the Magnetic Moment Anomaly of the Electon Bound in Hydrogenlike Carbon", Phys. Rev. Lett. **85** (2000) 5308.

[Herfurth01a] F. Herfurth, PhD Thesis, "A new ion beam cooler and buncher for ISOLTRAP and mass measurements of radioactive argon isotopes", University of Heidelberg, Germany, May 2001.

[Herfurth01b] F. Herfurth, J. Dilling, A. Kellerbauer, G. Bollen, S. Henry, H.-J. Kluge, E. Lamour, D. Lunney, R. B. Moore, C. Scheidenberger, S. Schwarz, "A linear radiofrequency ion trap for accumulation, bunching, and emittance improvement of radioactive ion beams", Nucl. Inst. Methods A **469** (2001) 254.

[Hill89]   Horowitz and Hill, "Art of Electronics", Cambridge University Press, 1989.

[Hofmann00]   S. Hofmann and G. Münzenberg, "The discovery of the heaviest elements", Rev. Mod. Phys. **72** (2000) 733.

[Kellerbauer02] A. Kellerbauer, PhD Thesis, "A Study of the Accuracy of the Penning Trap Mass Spectrometer ISOLTRAP and Standard-Model Tests with Superallowed Beta Decays", University of Heidelberg, Germany, July, 2002.

[Kellerbauer03] A. Kellerbauer, K. Blaum, G. Bollen, F. Herfurth, H.-J. Kluge, M. Kuckein, E. Sauvan, C. Scheidenberger and L. Schweikhard, "A Study of Accuracy of ISOLTRAP", Euro. Phys. J. D **22** (2003) 53.

[Klepper92]   O. Klepper, F. Bosch, H. W. Daues, H. Eickhoff, B. Franczak, B. Franzke, H. Geissel, O. Gustafsson, M. Jung, W. Koenig, C. Kozhuharov, A. Magel, G. Münzenberg, H. Stelzer, J. Szerypo and M. Wagner, "First steps towards radioactive beams in the experimental storage ring at GSI", Nucl. Inst. Methods B, **70** (1992) 427.

[Kolhinen03]   V. Kolhinen, PhD Thesis, "Penning Trap for Isobaric Purification of Radioactive Beams at IGISOL", University of Jyväskylä, Finland, June 2003.

[König95]   M. König, G. Bollen, H.-J. Kluge, T. Otto, J. Szerypo, "Quadrupole excitation of stored ion motion at the true cyclotron frequency", Int. J. Mass Spectr. Ion Proc. **142** (1995) 95.

[Kugler00]   E. Kugler, "The ISOLDE facility", Hyp. Int., **123** (2000) 23.

[Litvinov4]   Y. A. Litvinov, PhD Thesis, "Basic Nuclear Properties of Neutron-
                Deficient Nuclei Investigated via High Precision mass measurements in
                the Element Range 36≤ Z ≤ 92", University of Gieβen, Germany, May
                2004.

[Lunney96]   D. Lunney, G. Audi, C. Borcea, M. Dedieu, H. Doudre, M. Duma, M.
                Jacotin, J.-F. Képinski, G. Le Scornet, M. de Saint Simon, "MISTRAL:
                A new program for precise atomic mass determinations of nuclides far
                from stability", Hyp. Int. **99** (1996) 105.

[Lunney01]   D. Lunney, G. Audi, H. Doubre, S. Henry, C. Monsaglant, M. de
                Saint Simon, C. Thibault, C. Toader, C. Borcea, G. Bollen, and the
                ISOLDE Collaboration, "Precision mass measurements of very short-
                lived neutron-rich Na isotopes using a radio-frequency spectrometer",
                Phys. Rev. C, **64** 2001, 054311.

[Lunney03]   D. Lunney, J. M, Pearson, and C. Thibault, "Recent trends in the de-
                termination of nuclear masses", Rev. Mod. Phys. **75** (2003) 1022.

[Mancini99]   S. Mancini, A. M. Martins, and P. Tombesi "Quantum logic with a
                single trapped electron", Phys. Rev. A **61** (1999) 012303.

[Marx03]   G. Marx, J. Dilling, H.-J. Kluge, M. Mukherjee, W. Quint, S. Rahaman,
                D. Rodriguez, G. Sikler, M. Tarisien, C. Weber, and the SHIPTRAP
                Collaboration, "SHIPTRAP is trapping: A capture and storage device
                on its way towards a RIB-facility", Hyp. Int. **146**, (2003) 245.

[Meer85]   S. van der Meer, "Stochastic cooling and the accumulation of antipro-
                ton", Rev. Mod. Phys. **57** (1985) 689.

[Mohr99]   P. J. Mohr and B. N. Taylor, "CODATA Recommended Values of Funda-
                mental Physical Constants: 1998", J. Phys. Chem. Ref. Data **28** (1999)
                1713.

[Münzenberg79] G. Münzenberg, W. Faust, S. Hofmann, P. Armbruster, K. Güttner,
                and H. Ewald, "The Velocity Filter SHIP, A Separator of Unslowed
                Heavy Ion Fusion Products", Nucl. Inst. Methods. **161** (1979) 65.

[Neumayr04]   J. B. Neumayr, PhD Thesis, "The buffer-gas cell and the extraction RFQ
                for SHIPTRAP", Ludwig-Maximilians-Universität, München, Germany,
                April, 2004.

[Patyk89]   Z. Patyk, A. Sobiczewski, "Shell Effects in the Properties of the Heavist
                Nuclei ", Nucl. Phys. A **491** (1989) 267.

[Phillips98]   W. D. Phillips, "Laser cooling and trapping of neutral atoms", Rev.
                Mod. Phys. **196** (1998) 721.

[Radon2000]   T. Radon, H. Geissel, G. Münzenberg, B. Franzke, Th. Kerscher, F. Nolden, Yu. N. Novikov, Z. Patyk, C. Scheidenberger, F. Attallah, K. Beckert, T. Beha, F. Bosch, H. Eickhoff, M. Falch, Y. Fujita, M. Hausmann, F. Herfurth, H. Irnich, H. C. Jung, O. Klepper, C. Kozhuharov, Yu. A. Litvinov, K. E. G. Löbner, F. Nickel, H. Reich, W. Schwab, B. Schlitt, M. Steck, K. Sümmerer, T. Winkler, and H. Wollnik, "Schottky Mass Measurements of Stored and Cooled Neutron-Deficient Projectile Fragments in the Element Range of $57 \leq Z \leq 84$", Nucl. Phys. A **677** (2000) 75.

[Raimbault97] H. Raimbault-Hartmann, D. Beck, G. Bollen, M. König, H.-J. Kluge, E. Schark, J. Stein, S. Schwarz, J. Szerypo, "A cylindrical Penning trap for capture, mass selective cooling, and bunching of radioactive ion beams", Nucl. Inst. Methods B, **126** (1997) 378.

[Ravn92]   H. L. Ravn, S. Sundell, and L. Westgaard, "Target techniques for the ISOLDE on-line isotope separator", Nucl. Inst. Methods B, **70** (1992) 107.

[Rahaman02]   S. Rahaman, Diploma Thesis, "First Tests of the Penning traps of the SHIPTRAP Facility", University of Heidelberg, Germany, August 2002.

[Reisdorf81]   W. Reisdorf, "Analysis of Fissionability Data at High Excitation Energies", Z. Phys., **A 300** (1981) 227.

[Rodríguez02] D. Rodríguez, PhD thesis, "A Radiofrequency quadrupole buncher for accumulation and cooling of heavy radionuclides at SHIPTRAP and high precision mass measurements on unstable krypton isotopes at ISOLTRAP", University of Valencia, Spain, June, 2002.

[Savajols01]   H. Savajols, "The SPEG Mass Measurement Program at GANIL", Hyp. Int., **132** (2001) 245.

[Savard91]   G. Savard, St. Becker, G. Bollen, H.-J. Kluge, R. B. Moore, Th. Otto, L. Schweikhard, H. Stolzenberg, and U. Wiess, "A new cooling technique for heavy ions in a Penning trap", Phys. Lett. A **158** (1991) 247.

[Satpathy98]   L. Satpathy, R. C. Nayak, "Study of nuclei in the drip-line regions", J. Phys. **24** (1998) 1527.

[Satpathy04]   L. Satpathy, S. K. Patra, "Shell overcomes repulsive nuclear force instability", J. Phys. **30** (2004) 771.

[Schatz02]   H. Schatz, R. Toenjes, B. Pfeiffer, T. C. Beers, J. J. Cowan, V. Hill, K. L. Kratz, "Thorium and Uranium Chronometers applied to CS 31082-001", Astrophysical J., **579** (2002) 626.

[Sikler03a]   G. Sikler, PhD Thesis, "Massenspektrometrie kurzlebiger Sr- und Sn-Isotope und Aufbau der SHIPTRAP-Penningfallen", University of Heidelberg, Germany, February, 2003.

[Sikler03b]   G. Sikler, D. Ackermann, F. Attallah, D. Beck, J. Dilling, S.A. Elisseev, H. Geissel, D. Habs, S. Heinz, F. Herfurth, F.P. Hessberger, S. Hoffmann, H.-J. Kluge, G. Marx, M. Mukherjee, J. Neumayr, W.R. Plass, W. Quint, S. Rahaman, D. Rodríguez, C. Scheidenberger, M. Tarisien, P. Thirolf, V. Varentsov, C. Weber and Z. Zhou, "First on-line test of SHIPTRAP", Nucl. Inst. Methods B **204** (2003) 482.

[Smith71]   L. G. Smith, "Measurements of six light masses", Phys. Rev. C **4** (1971) 22.

[Stahl98]   S. Stahl, PhD Thesis, "Aufbau eines Experimentes zur Bestimmung elektronischer g-Faktoren einzelner wasserstoffähnlicher Ionen", University of Mainz, Germany, 1998.

[Steck98]   M. Steck, "Diagnostic methods to detect the properties of cooled heavy ion beams in storage rings", Nucl. Phys. A**626**, (1998) 473.

[Stolzenberg90] H. Stolzenberg et al., "Accurate Mass Determination of Short-lived Isotope by Tandem Penning Trap Mass Spectrometer", Phy. Rev. Lett. **65** (1990) 3104.

[Toader99]   C. Toader, "PhD Thesis", Orsay, 1999.

[Tremsin96]   A. S. Tremsin, J. F. Pearson, J. E. lees, G. W. Fraser, "The Microsphere Plate: A new type of electron multiplier", Nucl. Inst. Methods A **368** (1996) 719.

[Weber04]   C. Weber, PhD Thesis, "Konzeption eines kryogenen Penningfallenaufbaus für SHIPTRAP und Massenbestimmungen von Radionukliden um den Z = 82 - Schalenabschluss an ISOLTRAP", University of Heidelberg, Germany, February, 2004.

[Weizsäcker35]   C. F. Weizsäcker, "Zur Theorie der Kernmasssen" Z. Phys. **96** (1935) 431.

[Wouters85]   J. M. Wouters, D. J. Vieira, H. Wollnik, H. A. Enge, S. Kowalski, K. L. Brown, "Optical design of the TOFI (Time Of Flight Isochronous) spectrometer for mass measurements of exotic nuclei", Nucl. Inst. Methods A, **240** (1985) 77.

[Yu89]   J. Yu, M. Desaintfuscien et al., "Ion density limitation in a Penning trap due the combined effect of asymmetry and space charge", Appl. Phys. B **48** (1989) 51.